UCLouvain

École polytechnique de Louvain

High fidelity simulation of a high Reynolds flow around a 5:1 rectangular cylinder

Author: **Thomas VAN HOOBROUCK D'ASPRE**
Supervisors: **Jean-François REMACLE, Thomas TOULORGE, Michel RASQUIN**
Reader: **Vincent LEGAT**
Academic year 2022–2023
Master [120] in Mechanical Engineering

Acknowledgment

This thesis report signifies the culmination of a year's worth of arduous labor and dedication. It also marks the conclusion of many years of study at EPL, encompassing both its beautiful and challenging moments. I extend my heartfelt gratitude to all the individuals who have supported me throughout these past years, who placed their trust in me, and provided me with the opportunity to achieve this significant milestone.

In the first place, I express my deep appreciation to Cenaero for proposing the topic of my thesis and entrusting me with the completion of this research. I am truly thankful for their warm welcome and their support over the course of this year. I would particularly like to express my gratitude to Thomas Toulorge and Michel Rasquin, who graciously took me under their wing and generously shared their time to address my questions and guide me through this thesis.

I am grateful to my promoter at UCL, Professor Jean-François Remacle, for agreeing to sponsor this project and for his invaluable support and guidance. For their time and dedication to transmitting their knowledge, my gratitude goes to all the professors and assistants of EPL.

I would also like to thank Professor Vincent Legat, who graciously accepted to read and be a part of the jury of this thesis.

Finally, I would like to thank my parents, family and relatives for their unwavering trust, support and well-placed advice. This journey would not have been possible without their presence. A special note of appreciation goes to my girlfriend Sarah, who has been my constant companion and a pillar of support even during the most challenging periods.

Abstract

This thesis report is a contribution to the Jules Verne Benchmark launched by CSTB in 2022. The simulations of high Reynolds flow are preformed on three different meshes specifications using the solver developed at Cenaero, ARGO DGFluid. A thorough analysis of the flow results is detailed to help in the investigation of these not-well known high Reynolds flows around rectangular cylinders.

The results extracted showed good concordances with previous simulation found in the literature. The main bulk parameters of the flow reached expected values for the lift and drag coefficient, or the Strouhal number. The same observation was made on the mean flow features around the cylinder. Some inconsistencies within the three simulations showed the importance of the detached shear layer refinement and of the period of accumulation of statistics.

A crucial point however is the highly correlated pressure component obtained while conducting a spanwise correlation analysis. These results are outperformed by literature results while having a finer grid spacing in the spanwise direction. The correlations of the velocity vector in the x and z dimensions for the wake and the boundary layer showed however reassuring results.

Finally, this thesis observes the convergence towards a symmetry of the mean flow features and statistics.

Contents

Acknowledgment **i**

Abstract **ii**

List of Figures **vii**

List of Tables **viii**

List of Abbreviations **ix**

List of Symbols **xi**

Introduction **1**
Jules Vernes Benchmark at CSTB 2
Thesis outline 3

1 The science of elongated rectangular cylinders **4**
1.1 Elongated Rectangular cylinders 4
1.2 Aspect Ratio of 5 8

2 State of the art **10**
2.1 Numerical contributions 10
2.1.1 Turbulence modeling 11
2.1.2 Computational domain 13
2.2 BARC results and leads 16
2.3 Further investigations 19

3 Methodology **21**
3.1 Numerical domain 22
3.1.1 Boundary conditions 23
3.1.2 Mesh 26
3.2 Numerical solver 30

3.3 Mesh iterations . . . 31
3.3.1 Wall resolution . . . 31
3.3.2 Flow vorticity resolution . . . 35
3.4 Zenobe and Lucia . . . 39

4 Rectangular cylinders analysis 40
4.1 Monitoring of integral parameters . . . 41
4.1.1 Forces analysis . . . 41
4.1.2 Frequency analysis . . . 43
4.1.3 Time convergence . . . 45
4.1.4 Mesh convergence . . . 48
4.1.5 Comparison with literature . . . 51
4.2 Mean flow analysis . . . 53
4.2.1 Surfaces mapping . . . 53
4.2.2 Pressure distribution . . . 61
4.2.3 Mean flow convergence . . . 64
4.3 Spanwise correlation . . . 65
4.4 Symmetry analysis . . . 66

5 Conclusion 69

6 Improvement 71

A Mean flow convergence 72

B Spanwise correlations 76

List of Figures

1 The Jules Verne Platform 2

1.1 Streamlines at 300 tU/D of a 2D RANS simulation at Reynolds = 2×10^5, from Dahl's Master thesis [10] 5
1.2 Strouhal number (St_L) evolution in function of the aspect ratio at $Re_H = 10^3$, from Nakamura et al. [29] 7
1.3 Streamlines averaged in time and along the spanwise dimension (above) and scheme of the recognized mean flow structures (below). From Bruno et al. [7] 8

2.1 Pressure distribution from the BARC contributions. Picture obtained from Bruno et al. [8]. 17
2.2 Flow features of the simulations revised in the BARC. Picture obtained from Bruno et al. [8]. 18

3.1 Computational domain, indicating major dimensions and boundary conditions (not to scale) 23
3.2 Schematic of the no-slip and slip boundary conditions. Scientific figure from ReserachGate, available at: 25
3.3 First cells on the side of the surface of the cylinder 27
3.4 Structured mesh around the faces of the cylinder (left) and zoom on the fan configuration at the front edge (right). 27
3.5 Meshing cells in the x-y plane around a 5-1 rectangular cylinder, following the specifications 3. 29
3.6 Wall resolution - normal $\boldsymbol{y_0^+}$/p (left) and tangent $\boldsymbol{z_0^+}$/p (right) - for the top and bottom surfaces : first (above) and third specifications (below). 32
3.7 Distribution of the dimensionless $\boldsymbol{y_0^+}$ average in time, span and over the upper and lower surfaces of the cylinder. 33
3.8 Distribution of the dimensionless $\boldsymbol{x_0^+}$ (left) and $\boldsymbol{z_0^+}$ (right) average in time, span and over the upper and lower surfaces of the cylinder. 34

3.9 Instantaneous vorticity at t = 1.35 [s] of the detached shear layer for the first specification (top) and the third specification (bottom). 35
3.10 Instantaneous vorticity at t = 1.35 [s] near the front edge of the cylinder. The first specification (top) and third specification (bottom) are depicted. 36
3.11 Instantaneous vorticity at t = 1.35 [s] at the trailing edges of the cylinder. The first specifications (top) and third specification (bottom) are mapped. 37
3.12 Instantaneous vorticity at t = 1.35 [s] around the cylinder and with the wake region. The first specifications (top) and third specifications (bottom) are presented. 38

4.1 Time history of the lift (C_L) and drag (C_D) coefficients : the first specifications (left) ; the second specifications and the third one after the dotted line (right). 41
4.2 Frequency analysis for the three meshes simulations from top to bottom with the entire domains (left) and a zoom on the Strouhal frequencies (right). 44
4.3 Time convergence of the lift (right) and drag (left) coefficients for the first (upper) and second plus third (lower) specifications 46
4.4 Frequency analysis comparison between the three specifications, from the lift coefficient (left) and from the drag coefficient (right). 49
4.5 Mesh convergence of the simulations statistics : the drag coefficient (left), the lift coefficient (center) and the Strouhal number (right). . 50
4.6 Mean streamlines for the three meshes specifications. 55
4.7 Velocity contours from velocity magnitudes bellow 0.5 [m/s] for the three specifications. 56
4.8 Plot of the velocity magnitude along the y-direction at the center of the recirculation region abscissa x_c (left) and at the point of reattachment x_R (right). 57
4.9 Shear stress distributions over the surfaces for the three simulations. 59
4.10 Mean flow around the cylinder, with shear layer streamlines and velocity contours of velocity magnitudes below 0.5. 60
4.11 Distribution along the x direction of the pressure coefficient for the upper (left) and lower (right) surface, for the first (top), second (middle) and third (bottom) specifications. 63
4.12 Mean coefficient of pressure distribution for the three meshes. The coefficients are averaged in time, span and over the upper and lower surfaces. 64
4.13 Probes configuration 65
4.14 Pressure correlation at the cylinder surface for the third specifications 67

4.15 Correlation of pressure form the BARC at different points. From Bruno et al. [8]. 68

A.1 Mean flow of the first specification at distinct times increasing from top to bottom. 73
A.2 Mean flow of the second specification at distinct times increasing from top to bottom. 74
A.3 Mean flow of the third specification at distinct times increasing from top to bottom. 75

B.1 Velocity correlations in the wake, the x component (left) and the z component (right). 77
B.2 Velocity correlations in the boundary layer, the x component (left) and the z component (right). 78
B.3 Pressure correlations at the cylinder upper surface (left) and in the wake (right) 79

List of Tables

2.1 Numerical studies performed on rectangular cylinders with aspect ratio of 5 and their key parameters. 15

3.1 Meshes specifications 28
3.2 Dimensionless distance surface statistics 34
3.3 Some data on the computational time required to perform the simulations. 39

4.1 Statistical results from the monitoring of the lift and drag coefficient for the three meshes. 42
4.2 Strouhal numbers computed from the frequency analysis of C_L and C_D. 44
4.3 Statistical results from the monitoring of the lift and drag coefficient for the three meshes. Comparison between the statistic obtain on the whole period and the statistic obtained from the converged period. 48
4.4 Mesh statistics from the three simulations and ensemble average. . . 51
4.5 Time statistics and ensemble averages from the literature simulations. 52
4.6 Recirculation bubble data for the three meshes, and for the upper and lower cylinder's faces. 59
4.7 Statistics of reattachment and center of recirculation bubble from literature results. 61

List of Abbreviations

2D	Two dimensional
3D	Three dimensional
BARC	Benchmark on the Aerodynamics of a Rectangular 5:1 Cylinder
CFD	Computational Fluid Dynamics
CSTB	Centre Scientifique et Technique du Bâtiment
DES	Detached Eddy Simulation
DNS	Direct Numerical Simulation
DSM	Dynamic Smagorinsky turbulence Model
FEM	Finite Element Method
FVM	Finite Volume Method
HPC	High Performance Computing
KET	Kinetic Energy one-equation mode
LEA k - ω	Two-equation Linearized Explicit Algebraic Wilcox k - ω turbulence model
LES	Large Eddy Simulation
RANS	Reynolds-Averaged Navier-Stokes
RMS	Root Mean Square

RSM	Reynolds Stress Model
SA	One-equation Spalart-Allmaras turbulence model
SGS	SubGrid-Scale modelling for LES modelisations
SM	Standard Smagorinsky turbulence Model
URANS	Unsteady Reynolds-Averaged Navier-Stokes
WALE	Wall-Adapting Local Eddy-viscosity

List of Symbols

A_R	Aspect ratio
L	Cylinder length
H	Cylinder height
t	Time of simulated flow
U	Freestream velocity convention in some study, U_∞ in this thesis
D	Cylinder depth or height, convention used in some previous studies
B	Cylinder breadth or length, convention used in some previous studies
Re_H	Reynolds number evaluated with the height of the cylinder
U_∞	Freestream Velocity
ν	Kinematic viscosity of the fluid
μ	Dynamic viscosity of the fluid
ρ	Density of the fluid
St_l	Strouhal number in relation to the length of the cylinder
St_H	Strouhal number in relation to the height of the cylinder

f_1	Vortex shedding frequency
N_{rz}	Number of recirculation regions on a face of the cylinder
W	Spanwise length of the cylinder
D_x	Computational domain length in the x direction
D_y	Computational domain length in the y direction
Λ_x	Distance between the inlet boundary of the domain and the front face of the cylinder in the x direction
β	Blockage ratio of the cylinder in the domain
$\boldsymbol{n_0^+}$	Dimensionless wall-normal grid spacing of the first cell
u_x	Velocity in the x direction
u_y	Velocity in the y direction
u_z	Velocity in the z direction
p	Pressure
$\boldsymbol{u}$	Velocity vector
U_∞	Freestream velocity in the x direction
V_∞	Freestream velocity in the y direction
W_∞	Freestream velocity in the z direction
$R_{s,air}$	Specific gas constant of the air
T	Temperature
γ	Heat capacity ratio
ρ_{air}	Density of air

Pr	Prandlt number
κ_T	Thermal conductivity of the fluid
c_p	Constant pressure heat capacity
T_∞	Freestream temperature
p_∞	Freestream pressure
M_0	Freestream Mach number
β_s	Slip factor
u_t	Tangent velocity to the wall
$\boldsymbol{n_{wall}}$	Normal vector to the wall
P_{out}	Outlet pressure
σ	Damping factor of the sponge layer
x_{in}	Abscissa of the start of the sponge layer
x_{out}	Abscissa of the end of the sponge layer
dy_0	Dimension in the y direction of the first cell normal to the wall
dx_0	Dimension in the x direction of the first cell tangent to the wall
dx	Dimension in the x direction of a cell
dy	Dimension in the y direction of a cell
dz	Grid spacing in the z direction
u^+	Dimensionless velocity
κ	Constant of von Karman

$\boldsymbol{y^+}$	Dimensionless distance to the wall
τ_w	Wall shear stress
$\boldsymbol{y_0^+}$	Dimensionless distance normal to the wall of the first cell
$\boldsymbol{x_0^+}$	Dimensionless distance in the x direction tangent to the wall of the first cell
$\boldsymbol{z_0^+}$	Dimensionless distance in the z direction tangent to the wall of the first cell
p	Spatial discretization order of the solver
t_{real}	Real time of computation of the simulation
$t_{CPU,total}$	Total CPU time for the computation of the simulation
t_{CPU}/ct	CPU time of calculation for one convective time of simulation
ct	Convective time
C_L	Lift coefficient
C_D	Drag coefficient
n	Number of time steps

Introduction

In the realm of fluid mechanics, a particular emphasis lies in understanding the interaction between fluids and solid structures. Such flows develop complex behaviors that give rise to a multitude of distinctive features. From these, a classification has emerged to categorize the objects studied based on the source of the drag force they experience: streamlined bodies and bluff bodies. The drag force on a streamlined body primarily arises from the friction between its walls and the fluid, which are the viscous effects. Conversely, for a bluff body, the drag is significantly more influenced by the pressure component.

These structures have garnered significant academic and industrial interest. In industries such as automotive, aerospace development, and many other sectors, the impact of bodies moving through fluid flow has been extensively analyzed. Their objectives vary, including enhancing performance or efficiency and observing the structural impact of the flow. The academic world focuses less on the industrial prospects and more on the fundamental physics of the flow developing around these objects. A focal point of this fundamental academic research is set on simple bluff bodies, such as cylinders with circular, square, or rectangular bases.

Although primarily academic, the study of these basic shapes could arouse the interest of certain industrial sectors. In offshore or submarine engineering, a significant challenge arises from the structural stress induced by high currents and waves on platform columns or pontoons. In the construction industry, bridges and high-rise buildings are subjected to high velocity winds that could compromise their integrity if not well designed. However, reproducing such complex flows in water or wind tunnels is a costly and arduous process.

The development of numerical technologies has given engineering teams new ideas, and a new tool was soon developed: Computational Fluid Dynamics (CFD). The emergence of CFD opened the opportunity to perform analyses on complex geometries or flows that were previously less accessible. The cost of such simulations also significantly decreased compared to similar wind or water tunnel experiments.

Jules Verne Benchmark at CSTB

In the scope of this scientific advancement, this master's thesis aims to numerically investigate the characteristics of high Reynolds flow around a rectangular cylinder with an aspect ratio of 5. The comprehensive analysis of the results obtained from CFD simulations intends to contribute to the understanding of flow patterns, vortex shedding, pressure distribution, and other related parameters. These insights aim to facilitate the identification of underlying mechanisms and the prediction of performance for high Reynolds flows.

This master's thesis simulations and analysis constitute a contribution from Cenaero to the Jules Verne Benchmark. The software Argo DGFluid, developed at Cenaero, was used to conduct the numerical investigations. The simulations and analysis were performed using Cenaero's infrastructures, including the supercomputers Zenobe and Lucia.

The Jules Verne Benchmark was launched in early 2022 by CSTB in Nantes, France, in association with CNRS and the Institute of Engineering and Systems Sciences (INSIS). The Centre Scientifique et Technique du Bâtiment (CSTB) contributes to the Benchmark with experimental simulations performed in the Jules Verne platform presented in figure 1. With this climatic wind tunnel facility, CSTB proposed the aerodynamic test section to the academic community to study high Reynolds number aerodynamic flows.

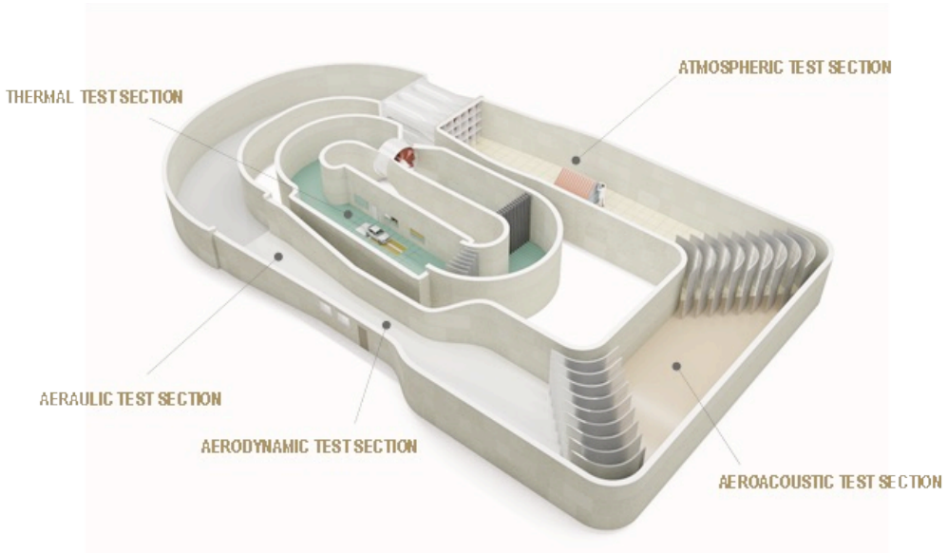

Figure 1: The Jules Verne Platform

Thesis outline

Chapter 1 introduces insights gathered from previous studies on rectangular cylinders. Theoretical concepts are initially outlined, along with a comprehensive description of the flow around rectangular cylinders. The influence of various parameters and the behavior of others are examined through the first studies on the subject.

Chapter 2 provides an overview of the state of the art. It details the characteristics of numerical simulations, turbulence models and computational domains. An overview of previous numerical researches is provided with relevant characteristic parameters. This chapter concludes with a presentation of the results obtained from those studies, along with their conclusions, remarks and potential directions for further research.

Chapter 3 presents the methodology employed for the simulations performed in this thesis. The computational domain and its boundary conditions are introduced, followed by an explanation of the discretization process used and its key parameters. The numerical solver and the main equations it solves are briefly discussed. Finally, the analysis of key parameters for the iterative meshing process is described and some primary results on the improvement in resolution are observed.

Chapter 4 offers a complete analysis of the three simulations conducted for this thesis. The results are compared both within the simulations and with results from existing literature. The chapter first focuses on monitoring key parameters. Furthermore, the mean flow features are described and critical values are extracted to enable the mapping of flow features. The spanwise dimension is also analyzed through correlations of pressure and velocity.

Chapter 5 summarizes the final conclusions drawn from the simulations and analysis performed in this thesis It provides key results and analysis along with discussions about the limitations of this work and comparisons with previous studies.

Chapter 6 suggests recommendations for future work.

Chapter 1

The science of elongated rectangular cylinders

In this thesis work, the flow around the simple geometry of a rectangle is studied. Although the set-up initially appears straightforward and the flow features are predominantly two-dimensional, at high Reynolds numbers, the complexity increases due to the development of three-dimensional structures.

Numerous researchers in the past decades have investigated the dynamics of these phenomena and examined the influence of various parameters, such as the geometry of the cylinder or the flow characteristics. In the following section, a brief summary of their research findings and conclusions is provided.

1.1 Elongated Rectangular cylinders

The primary parameter that significantly affects the flow around a rectangular cylinder is its aspect ratio, defined as the ratio between the streamwise length (L) and the crosswind height (H) of the structure:

$$A_R = \frac{L}{H} \tag{1.1}$$

Early on, parametric studies were conducted using wind tunnel experiments (see Nakaguchi et al.[25], Stokes and Welsh [40], Parker and Welsh [32], Nakamura et al. [27] [28] [29] or Okajima et al. [31] ...), and more recently, numerical simulations have also been employed. Despite variations in set-ups, these initial studies revealed consistent behavior.

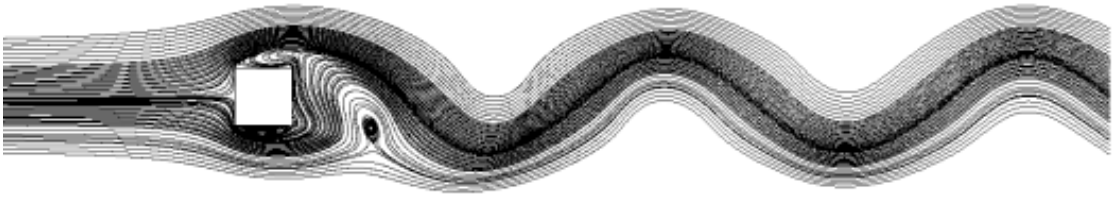

(a) B/D = 1

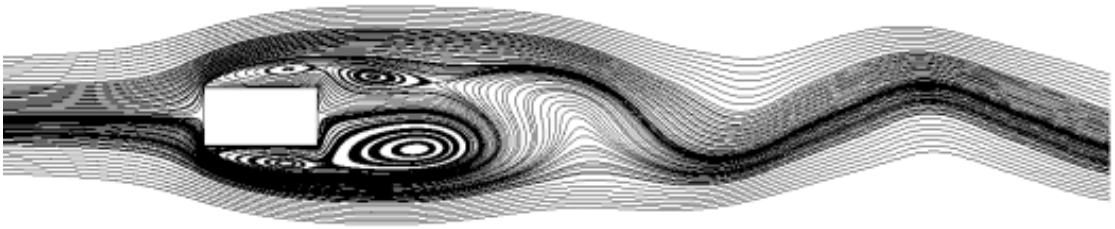

(b) B/D = 2

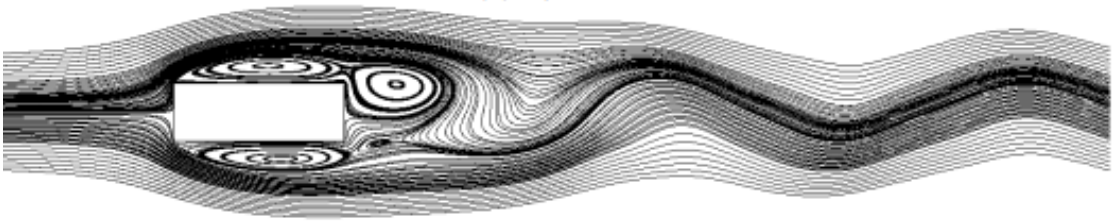

(c) B/D = 3

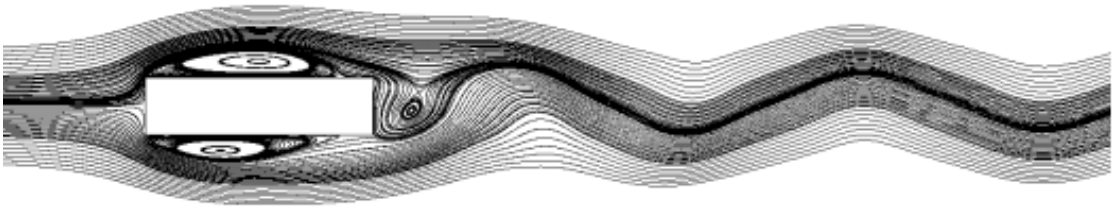

(d) B/D = 4

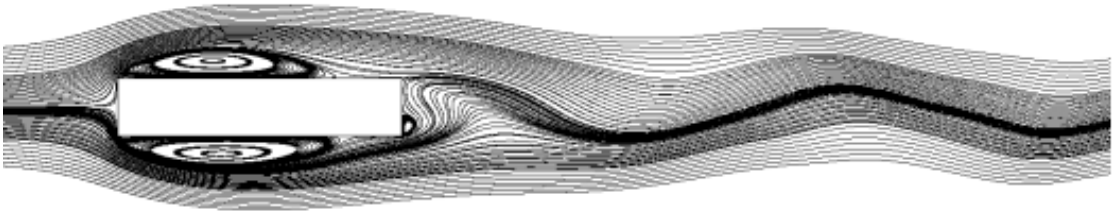

(e) B/D = 5

Figure 1.1: Streamlines at 300 tU/D of a 2D RANS simulation at Reynolds = 2×10^5, from Dahl's Master thesis [10]

For small aspect ratios, up to approximately 2.8, the flow separates from the cylinder at the leading edge, and the boundary layer does not reattach. Additionally, vortex shedding is only observed from the leading edge.

As the aspect ratio exceeds 2.8, the shear layer impinges on the side faces of the cylinder. Up to an aspect ratio of 3.5, a dynamic of intermittent reattachment of the shear layer to the side surfaces is observed.

Once the aspect ratio surpasses 3.5, the mean flow permanently reattaches to the cylinder's faces. This results in the formation of a recirculation bubble on the sides of the body. From this point, vortex shedding also occurs at the trailing edge.

It is important to note that the presented results are dependent on numerous parameters, not solely the aspect ratio of the cylinder. The values presented above were deduced for high Reynolds numbers in Okajima et al. [31]. This dimensionless number is another crucial parameter of great influence in fluid mechanics :

$$Re_H = \frac{U_\infty H}{\nu} \tag{1.2}$$

with U_∞ as the freestream velocity, H as the height of the cylinder and $\nu = \frac{\mu}{\rho}$ as the kinematic viscosity of the fluid.

This dimensionless number represents the ratio between inertial and viscous forces, playing a significant role in fluid dynamics. It distinguishes laminar flows at low Reynolds numbers from turbulent ones at higher Reynolds numbers.

At $Re_H = 1$, the flow remains perfectly laminar, adhering to the cylinder's faces. However, as the Reynolds number increases ($Re_H > 5$), the flow starts to detach while remaining laminar, resulting in the development of a pair of symmetric vortices in the wake. With further increases in Reynolds number, these vortices evolve into a vortex street. This vortex street is initially laminar, but as the Reynolds number surpasses the range of $200 < Re_H < 300$, it transitions into a turbulent wake. Beyond this critical Reynolds number, the wake becomes completely turbulent, characterized by a laminar shear layer separation.

In the various studies, the Reynolds numbers used vary greatly. With low values for certain studies, the lower end is around 10^3 (Nakamura et al. [26], Hourigan et al. [15] or Tan et al. [43]). Some studies employ higher Reynolds numbers, around 10^4 (Tamura et al. [41] [42] or Shimada and Ishihara [38]), or 10^5 (Yu et al. [46] [45]). However, few studies reach a Reynolds number of 2×10^5, which is our value of interest, found only in Dahl's master thesis [10], a two-dimensional simulation.

When studying bluff bodies with higher aspect ratios, an additional parameter needs to be considered: the Strouhal number. The Strouhal number, denoted as St_L or St_H, represents the vortex shedding frequency (f_1) of the cylinder in relation to its length or height, respectively, and the flow velocity.

For aspect ratios between 3.5 and 6, the Strouhal number is approximately 0.55. This value might also change based on other parameters such as the Reynolds number:

$$St_L = \frac{f_1 L}{U_\infty} \approx 0,55 \tag{1.3}$$

In 1991, Nakamura et al. [29] pointed out the non-continuous relation between the Strouhal number and the aspect ratio of the cylinder. This discontinuity is primarily influenced by the number of recirculation zones attached to the side faces of the cylinder. For aspect ratios between 3.5 and 6, a single separation and reattachment occurs, resulting in only one recirculation zone.

However, as the aspect ratio increases above 6, multiple detachments and reattachments of the boundary layers occur, leading to more than one recirculation zone. For instance, between 6 and 9, there are two of them. In such cases, the Strouhal number can be approximated by:

$$St_L \approx 0.55 N_{rz} \tag{1.4}$$

Here N_{rz} denotes the number of mean recirculation zones on each face of the cylinder.

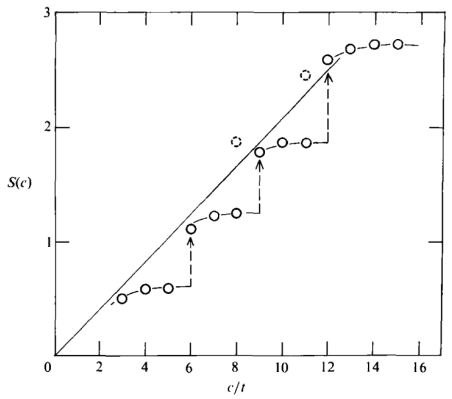

Figure 1.2: Strouhal number (St_L) evolution in function of the aspect ratio at $Re_H = 10^3$, from Nakamura et al. [29]

The same relationship holds when the aspect ratio is further increased, resulting in a third, fourth, and so on, recirculation zone.

1.2 Aspect Ratio of 5

In 2008, based on those observations, scientists initiated the BARC benchmark, focusing on a rectangular cylinder with an aspect ratio of 5. This specific aspect ratio was chosen because it significantly differs from the critical values of the Strouhal number (observed at $A_R = 2.8$ and 6). These discontinuities can have a substantial impact on flow features and thus statistical results. This could lead to greater discrepancies when comparing different studies. By avoiding these critical values, the benchmark aimed to improve the reliability of the findings.

Starting the benchmark with no predefined reference, one of the objectives was to gather a comprehensive database and create a reliable reference for future studies. Given the numerous parameters already influencing the flow, operating in the proximity of discontinuities could have introduced unwanted confounding factors, affecting the accuracy of the analysis.

An added advantage of the chosen aspect ratio (5) is that the flow reattaches permanently to the cylinder, resulting in a single recirculation zone. This aspect ratio encompasses all the interesting flow phenomena and their development. Additionally, having only one recirculation zone makes it easier to observe compared to scenarios with two or more recirculation zones.

Below, the primary flow characteristics around the rectangular cylinder with an aspect ratio of 5 are presented, as shown in figure 1.1.

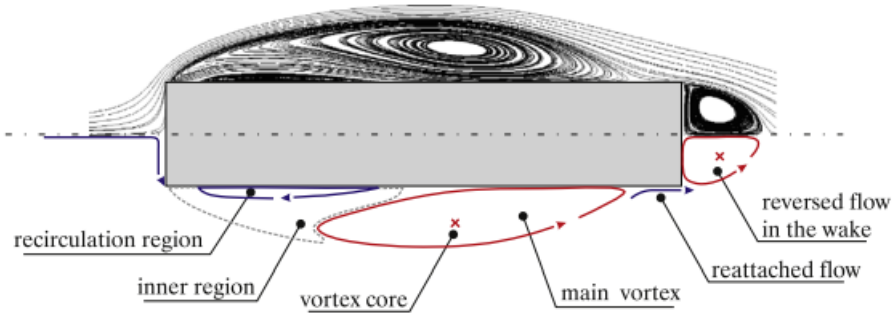

Figure 1.3: Streamlines averaged in time and along the spanwise dimension (above) and scheme of the recognized mean flow structures (below). From Bruno et al. [7]

The flow around the cylinder can be divided into three distinct regions following the development of vortex shedding. In the front region, the shear layer separates at the leading edge, initiating vortex shedding. Further down, the shear layer starts to

roll up, leading to the formation of vortical structures. These structures of different shapes and sizes develop in a main vortex along the cylinder face. The final region corresponds to the end of the recirculation region, drawn from the mean flow. In this region, the mean flow reattaches to the cylinder's face near the rear edges.

At these trailing edges, a second vortex shedding occurs from the reattached boundary layer. The mean flow is described by two reversed flow vortices on the rear surface of the cylinder. Behind the cylinder, a von Karman vortex street is observed, with the wake rotation fluctuating between clockwise and counterclockwise. However, the vortex shedding mechanism is not of the Karman type, created by the interactions of the upper and lower detached shear layers. Nakamura et al. [28] proposed that it is due to the instabilities of the shear layers impinging on the cylinder's faces.

A last point described in some studies, such as the one depicted in figure 1.3 from the simulations of Bruno et al. [7], is the formation of a second recirculation region. This one is situated close to the leading edge, near the shear layer separation. In this recirculation region, the flow rotates in the opposite direction compared to the main vortex. n some simulations, this feature is barely visible and in others, it does not appear at all.

The mapping described above is based on average quantities. Indeed all the phenomena are unsteady and evolve following certain frequencies, with the primary being the shedding frequency of the Strouhal number. This unsteadiness, added to the complexity of the flow, requires computing the solution over a large period of time to obtain good statistical convergence.

Chapter 2

State of the art

In the early days of the study of rectangular cylinders and other cylinder shapes, most experiments were conducted using wind tunnels. With the advent of more powerful computers and processors, there has been a proliferation of numerical studies. Similar to wind or water tunnel experiments, each numerical study has its own set-up. As mentioned and presented, numerous parameters can influence the flow. Analyzing the causes of differences in simulation results is therefore challenging. Additionally, the lack of standardized reference set-up for numerical (and experimental) studies adds complexity to the task.

2.1 Numerical contributions

The following section presents an overview of the numerical simulations conducted over the past decades that have contributed to the study of rectangular cylinders with an aspect ratio of 5 Additionally, some details on the principal parameters used in these numerical simulations are provided. A summary of these contributions along with key parameters is presented in the table 2.1 bellow.

The table is divided into three sections. The first one covers preliminary studies that mainly focused on the effect of the aspect ratio. The second section presents the contributions to the BARC Benchmark initiated in 2008. This benchmark led to initial conclusions, analyses and questions regarding this specific aspect ratio of 5. Finally, the third part encompasses studies conducted afterward. These studies concentrated on specific parameters, both geometric ones such as edge rounding and spanwise dimension, as well as resolution and fluid properties like inlet turbulence. Most of these studies were undertaken to help address the questions raised during the BARC Benchmark.

2.1.1 Turbulence modeling

The primary challenge when modeling high Reynolds number flows like this one is turbulence. All simulations presented here were performed at relatively high Reynolds numbers, typically high enough for the wake to be fully turbulent.

Turbulence poses a significant difficulty for numerical solvers. Turbulent flows are characterised by chaos arising from the formation of eddies, swirls and vortices. The velocity of turbulent fluid varies irregularly in both space and time, resulting in unpredictable fluid movement.

The complexity of turbulent flows for numerical solvers lies in their ability to solve them with precision. The fluid flow is modeled using the Navier-Stokes equations, which can be solved to capture all the scales of turbulence. However, this is a demanding task that requires substantial computational power, which is why several methods to handle turbulence have been developed.

In the previous simulations, various numerical methods were employed, including LES, DES, RANS and some DNS. For each approach, different closures and software codes were used, with OpenFOAM and Fluent being the most common, along with proprietary codes. Most of these codes share a common feature: they employ the finite-volume method (FVM). Furthermore, all of the simulations are designed to be second-order accurate in both space and time.

Direct Numerical Simulation (DNS)

In Direct Numerical Simulation (DNS), the Navier-Stokes equations are solved directly without any reliance on a turbulence model. This approach achieves the highest level of accuracy, aiming to resolve all scales of turbulence down to the smallest ones (Kolmogorov scales). However, the computational cost associated with DNS is substantial, owing to the requirement to resolve even the smallest turbulent structures. Especially at high Reynolds numbers, the demands of DNS can be prohibitive. In most practical cases, this method is rarely used in industry due to the computational expense outweighing the added accuracy it provides.

DNS is primarily employed for numerical experiments in academic research, particularly in the study of the fundamental physics of turbulence. The computational cost is further compounded because the scenarios where DNS is of interest often involve turbulent flows and therefore tend to be transient phenomena. Since these flows lack a steady state, observing the complete evolution and development of the mean flow necessitates accumulating data over an extended period of time.

Large Eddy Simulation (LES)

Solving all the smallest scales of turbulence with DNS is a highly resource-intensive method. In Large Eddy Simulation (LES), the larger scales of turbulence, referred to as large eddies, are directly solved, while the smaller scales are filtered out and resolved using a computational filter. All scales below this filter are time-averaged and effectively "ignored". However, these smaller scales still play a crucial role in the flow, which is why the effects of the unresolved small eddies on the flow must be modeled.

The unresolved smallest scales are lost due to this filtering process, but their influence on the flow remains present within the simulation model. This method is less precise than DNS, but the reduction in computational cost to achieve reasonably accurate results is appealing.

Here are some of the turbulence models used in various LES numerical studies:

- **Standard and Dynamic Smagorinsky Model (SM and DSM)** : The unresolved turbulent eddies at the subgrid-scale behave in a diffusive manner. The eddy viscosity is determined by a constant known as the Smagorinsky coefficient. DSM offers improved accuracy over the standard version, especially for complex and unsteady flows.
- **Kinetic Energy one-equation model (KET)** : This model is based on the transport equation for kinetic energy, which describes the transfer of energy between resolved and unresolved scales. The KET model solves a single transport equation for the resolved turbulent kinetic energy and uses it to estimate the eddy viscosity.
- **Wall-Adapting Local Eddy-viscosity (WALE)** : The WALE model utilizes a wall-distance function to adjust the eddy viscosity based on the proximity to the nearest wall. This enables the model to account for variations in turbulence structures near the wall, leading to improved predictions for flows with complex boundary layers.

Reynolds-Averaged Navier-Stokes (RANS)

The Reynolds-Averaged Navier-Stokes (RANS) method is a widely used turbulence modeling approach in CFD simulations. RANS equations are derived from the Navier-Stokes equations and are employed to solve turbulent flow problems. In RANS, turbulent flow properties are statistically averaged over time, which enhance computational efficiency compared to approaches that require resolving all the turbulent scales, such as DNS, or some in LES.

Nonetheless, the choice of appropriate turbulence models is crucial to accurately represent the behavior of turbulent flows. Many RANS simulations employ Eddy-viscosity turbulence models, with some utilizing the Reynolds Stress Model (RSM):

- **Eddy-viscosity turbulence model** : These models assume that the turbulent stresses can be represented by a viscosity concept, similar to the molecular viscosity in the laminar flow. The eddy-viscosity is generally related to local flow properties and is determined using empirical relationships. Many variation of this model exist, such as the one-equation Spalart-Allmaras model (SA), the two-equation Linearized Explicit Algebraic Wilcox k - ω model (LEA k - ω), or k - ϵ model.
- **Reynolds Stress Model (RSM)** : RSM is a six-equation model that predicts all components of the Reynolds stress tensor, offering a more accurate representation of the anisotropic nature of turbulence. It is a more sophisticated turbulence model compared to eddy-viscosity models like k - ω or k - ϵ.

Detached Eddy Simulation (DES)

Detached Eddy Simulation is a hybrid turbulence modeling approach that integrates elements from both Reynolds-Averaged Navier-Stokes (RANS) and Large Eddy Simulation (LES) methods. DES attempts to bridge the gap between these two approaches by dynamically transitioning between RANS and LES in different regions of the flow domain. In areas where turbulence is expected to be well-resolved and large eddies dominate the flow behavior, LES techniques are used. Conversely, in regions closer to walls or in regions where turbulence is anticipated to be more complex, RANS models are employed to reduce the computational expenses.

2.1.2 Computational domain

The simulations performed throughout the years have employed diverse set-ups encompassing variations in domain size, shape and grid definitions. Several dimensions are crucial when configuring the computational domain.

Firstly, the spanwise dimension, which underwent a sensitivity study in Bruno et al. [6] and Mariotti et al. [23]. A few of the realisation were conducted in 2D, primarily during the early stages of CFD or for RANS simulations. In most cases were 3D domain are employed, the span over height ratio stood at 5 or 10.

As for other pertinent dimensions, the domain length in the x (D_x) and the y (D_y)

directions, as well as the distance between the inlet boundary and the cylinder (Λ_x) are observed. These lengths exhibit significant variations from one study to another, but some minimal value where deduced by the authors of the BARC review [8]:

$$\frac{D_y}{H} > 40 \quad \textbf{and} \quad \frac{\Lambda_x}{H} > 20 \tag{2.1}$$

Where H is the height of the cylinder.

In terms of the domain's size in the x and y directions, most studies adopted dimensions between 20 to 50 times the length (L) of the cylinder. The sole requirement for the BARC was a minimum blockage of 0.05:

$$\beta = \frac{H}{D_y} \tag{2.2}$$

Although the majority of studies adhered to similar values and remained within the same range, Wei et al. [44] stood out by employing a significantly smaller domain. Conversely, another notable exception was the studies of Mannini et al. [19] [20] [21], with a domain at least four times larger in the x and y dimensions.

Grid Types

As mentioned, both the shape of the domain and the grid configurations exhibit significant variations. While most domains are prismatic, a frequent cylindrical shape is also observed. Regarding the grids in the x-y plane, nearly all of them are hybrid, featuring a combination of body-fitted and structured grids in the vicinity of the cylinder, while employing unstructured grids elsewhere. Some exceptions employ fully unstructured or structured grids Across all 3D cases, the grid is structured in the spanwise direction z with a consistent discretization size. The grid cells themselves are of various types, including triangular or quadrilateral cells.

In the structured near-wall region, an critical parameter is the size of the first cell. Most grids attempt to achieve a cell size that results in a dimensionless wall-normal grid spacing of $\boldsymbol{n_0^+} = 1$. This value plays a pivotal role in ensuring proper wall resolution for the flow.

The boundary conditions used are predominantly consistent, featuring no-slip conditions on the surfaces of the cylinder and periodic boundaries on the spanwise boundaries. For the top and bottom faces, there is a small variety between periodic conditions and slip conditions, depending on the cases. The inflow conditions display the most variation, encompassing differences in inlet turbulence intensity and Reynolds number as determined by the freestream velocity.

Simulation		Turbulence model		Freestream	Domain dimensions		
Authors	Year	Method	Model	Re_H	W/H	D_x/L	D_y/L
Ohya et al.	1992 [30]	DNS	/	10^3	0 (2D)	313	81
Tamura et al.	1993 [41]	DNS	/	10^4	2	60	60
	1996 [42]	DNS	/	10^4	2	60	60
Nakamura et al.	1996 [26]	DNS	/	200 - 10^3	0 (2D)	/	/
Yu et al.	1998 [46]	LES	SM	10^5	2	30.22	15.23
Hourigan et al.	2001 [15]	DNS	/	300 - 400 - 500	0 (2D)	/	/
Shimada et al.	2002 [38]	RANS	k - ϵ	2.2×10^4	0 (2D)	12	12
Tan et al.	2004 [43]	DNS	/	400	0 (2D)	/	/
Arslan et al.	2011 [3]	LES	SM,DSM,KET	2.64×10^4	5	23	20.2
Bruno et al.	2010 [7]	LES	KET	4×10^4	5	41	30.2
	2011 [6]	LES	KET	4×10^4	5, 10, 20	41	30.2
Grozescu et al.	2011 [13]	VMS-LES	SM	2×10^4	0 (2D)	41	30.2
	2011 [12]	VMS-LES	WALE	4×10^4	0 (2D)	41	30.2
Mannini et al.	2010 [20]	URANS	SA	2.64×10^4	5	200	200
	2011 [21]	URANS	LEA k - ω	10^5	10	200	200
Mannini & Schewe	2011 [19]	DES	SA	2.64×10^4	5	200	200
Riberio	2011 [33]	URANS	RSM	2.64×10^4	0 (2D)	51	50.2
Wei and Kareem	2011 [44]	LES	DSM	10^5	0 (2D)	8	3
Yu et al.	2013 [45]	LES	SM	10^5	/	/	/
Dahl	2014 [10]	RANS	k - ϵ	2×10^5	0 (2D)	8	5
Mariotti et al	2016 [22]	RANS	SST - k - ω / RSM	4×10^4	0 (2D)	40	30
	2017 [23]	LES	Fisher	4×10^4	5	41	30.2
Ricci et al	2017 [34]	LES	MDSRFG	5.5×10^4	5 - 15	40	30
Cimarelli et al	2018 [9]	DNS	/	3000	5	22.4	10
Mannini et al.	2019 [17]	LES	SEM	4×10^4	5	41	30.2
Rocchio et al.	2020 [37]	LES	Fisher	4×10^4	5	41	30.2
Abbasi	2022 [1]	URANS	k - ω - SST	5×10^4	0 (2D)	18	20

Table 2.1: Numerical studies performed on rectangular cylinders with aspect ratio of 5 and their key parameters.

2.2 BARC results and leads

During the initial years of the Benchmark on the Aerodynamics of a Rectangular 5:1 Cylinder (BARC), ten teams of researchers produced eighteen wind tunnel tests and forty-one computational simulations. The preliminary findings of the BARC were analyzed and summarized in the paper by Bruno et al. [8]. Several interesting observations were made, leading to further questions and the need for more in-depth studies of the rectangular cylinder's aerodynamics.

They first compared the time-averaged statistics of bulk parameters for the simulations and experiments. They found that the drag coefficient was approximately 1 in numerical studies, which closely aligned with experimental results. Most studies converged towards this value, with one notable exception in the case of Wei and Kareem [44], where the results were exaggerated. This deviation was attributed to the small computational domain size chosen in that study.

Another parameter with consistent results was the Strouhal number, with an average around 0.109. However, the mean lift coefficient expected to be zero, was not reached in some of simulations. This discrepancy could indicate an asymmetry in the mean flow. Furthermore, a significant dispersion in numerical predictions for the standard deviation of the lift coefficient was observed.

The researchers concluded that LES simulations yielded better and more accurate results than their RANS counterparts. However this was only true, when certain LES results were discarded, particularly those from 2D simulations (as in Arslan et al. [3]) or simulations with small domains (as in Wei and Kareem [44]), highlighting the importance of the choice of computational domain.

The second point of comparison among the analyzed studies was the mean flow features. The data analyzed included the mean pressure distribution on the cylinder's surface and the characteristics of the main recirculation zone. As seen in fig 2.1, both numerical and experimental pressure distribution data exhibited considerable spread. Only in a low-pressure plateau before the recirculation zone did simulations show relatively close results, whereas the dispersion in experimental data remained significant.

The mean flow features across the different simulations also exhibited substantial variation. Some featured extremely long recirculation bubbles, as observed in experimental results, while others had shorter or even extremely short recirculation regions, as shown in figure 2.2.

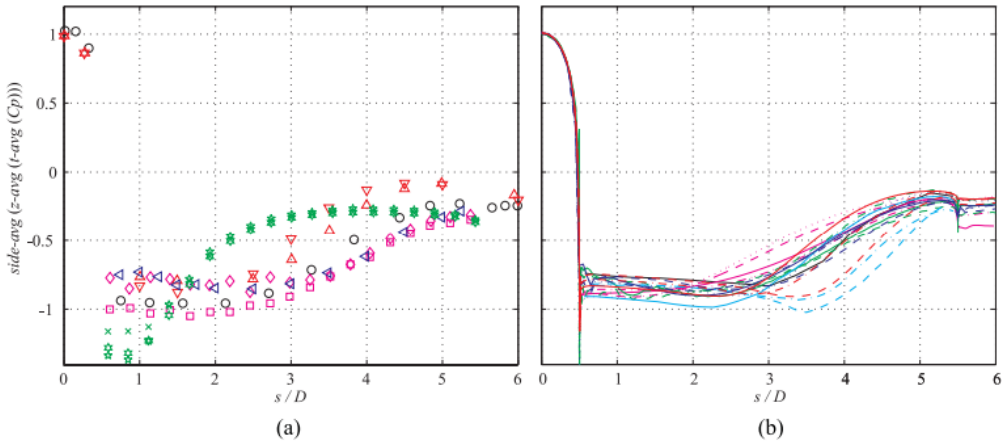

Figure 2.1: Pressure distribution from the BARC contributions. Picture obtained from Bruno et al. [8].

The choice of simulation methods (LES, RANS,...) and turbulence models appeared to play a crucial role, particularly for RANS simulations. For LES models, subgrid-scale modeling (SGS) and numerical dissipation had a notable impact on the mean flow topology. What disturbed the scientist is that the shorter recirculation regions are obtained from seemingly more precise results, with more refined meshes. An investigation on spanwise discretization performed by Bruno et al. [6] revealed that increasing resolution led to shorter recirculation lengths, contrary to experimental results.

In conclusion, numerous questions remained unanswered regarding the observed dispersion during the BARC. While the origins of dispersion in numerical and experimental studies may differ, the effects are similar. No reference experimental or simulation set-up could be extracted from the results, given the absence of conclusive findings on the impact of each parameter.

The turbulence models employed in the various simulation all have exult dispersion in the results. Although LES simulations did better than RANS, intriguing outcomes were still obtained The influence of the subgrid-scale models, the size of the computational domain or the spanwise grid resolution appeared to be key issues. Lastly, an asymmetry in time-average flow was observed both in wind tunnel experiments and the numerical simulations.

Sensitivity studies on the mentioned parameters were deemed necessary to establish a reference numerical setup. To help characterize the flow properties with better

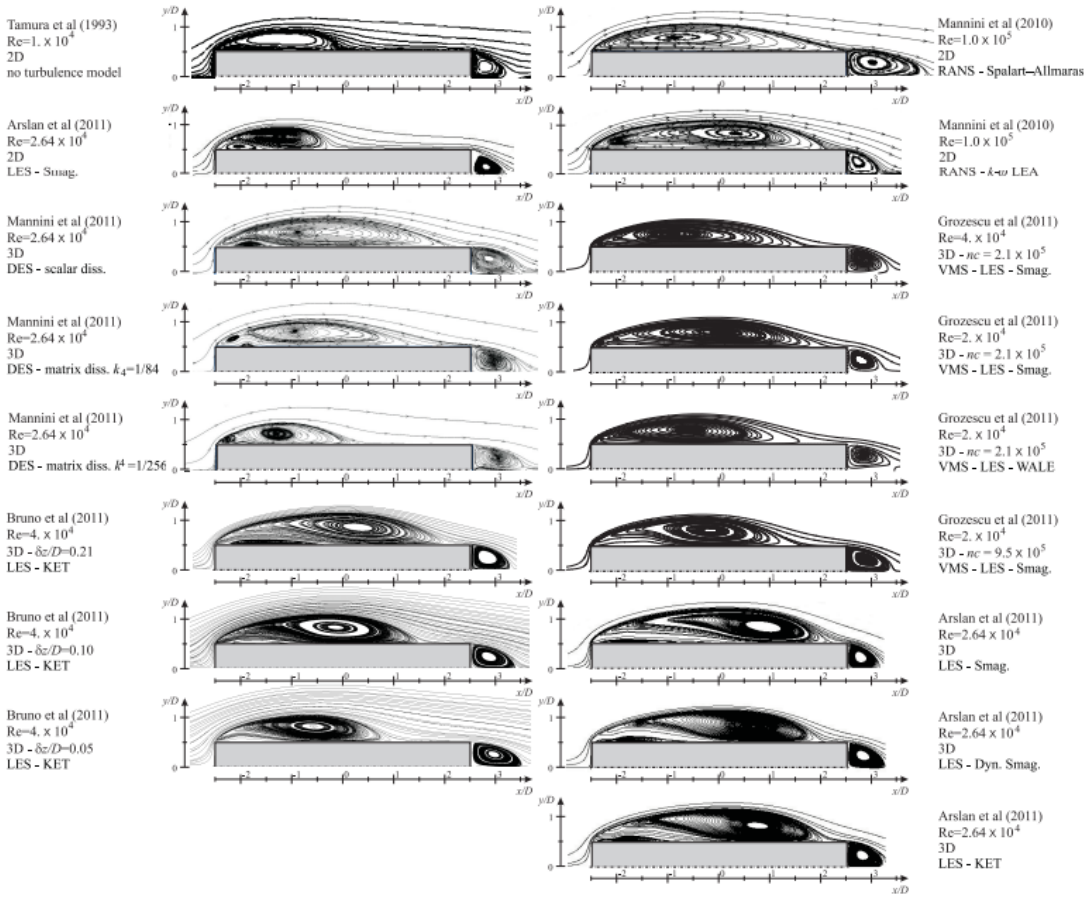

Figure 2.2: Flow features of the simulations revised in the BARC. Picture obtained from Bruno et al. [8].

precision, Bruno et al. [8] conducted ensemble statistics on all benchmark results to provide a more precise characterization of flow properties. Further investigations and simulations could enhance these results by contributing more data sets to the statistical analysis.

2.3 Further investigations

Following the conclusion drawn by the BARC and the substantial dispersion observe among the results, several studies investigated the effects of various parameters or uncertainties. These studies aimed to provide explanations for the observed dispersion and identify key influencing factors Below is a summary of these works, along with a brief description of their focus and conclusions.

In Mariotti et al. [2016] [22], the impact of freestream flow parameters was investigated, including angle of incidence, freestream turbulence intensity, and length scale. While some dispersion in the results was observed, it was not as pronounced as in the BARC results. The study suggested that freestream uncertainties are not the sole contributors to the dispersion. Other parameters, such as geometric edges uncertainty in experiments, blockage ratio (which was ruled out), and spanwise discretization, were identified as potential sources. The authors used two turbulence models (SST - k - ω and RSM) for 2D URANS simulations and employed a stochastic collocation method to assess uncertainties. They found that the turbulence model significantly impacts the sensitivity of uncertainties, with the RSM model exhibiting higher variability and minimal influence from grid discretization.

In Mariotti et al. [2017] [23], they focused on investigating the impact of spanwise discretization and subgrid-scale models on the dispersion of LES results Building upon the 2012 investigation by Bruno et al. [6], which results significantly deviated from the ensemble average of the BARC results, they performed stochastic analysis on two grids models - coarser and refined. The coarser grid results of the probable flow were in alignment with the BARC results. However, the finer grid confirmed the results observed by Bruno et al. [6], with a smaller recirculation region and the related pressure distribution. The study confirmed the higher sensitivity of results to spanwise grid refinement over SGS dissipation. This phenomenon was attributed to the influence of shear layer instability capture and small vortical structures originating from it. The researchers speculated whether an extremely sharp leading edge could introduce noise and explain discrepancies between LES results influenced by spanwise discretization and experimental results unaffected by this factor.

The findings from Bruno et al. [2012] [6] and Mariotti et al. [2017] [23] help explain the extensive dispersion present in the BARC results. Indeed, the sensitivity of the result to the capture of shear layer small vortical structures has been pointed out. Many the BARC contributions used URANS or DES method that may not capture these structures. Similarly, LES simulations with coarser grids or higher

dissipation may fail to accurately reproduce flow dynamics.

In Mannini et al. [2017] [18], they performed a wind tunnel experiment with increasing inlet freestream turbulence. The results demonstrated that a shorter recirculation region develops on the sides of the cylinder as the inlet turbulence intensity increases. In Ricci et al. [2017] [34], they conducted similar study with numerical Large-Eddy simulations, leading to the confirmation of the results observed.

In Rocchio et al. [2020] [37], they investigated the effect of edge rounding on flow behavior. The authors aimed to model the uncertainty of fabrication tolerance for experimental cylinder edges. Indeed, the study wish to address the discrepancy observed in the previous studies of Bruno et al. [2012] [6] and Mariotti et al. [2017] [23], where fine grids yielded smaller recirculation bubbles than experiments. It was noted that experiments with inlet turbulence intensity should have shorter recirculation regions than numerical simulations without it. The study concluded that even minimal edge rounding significantly affected the recirculation bubble and flow over the cylinder's surfaces. A longer recirculation bubble was observed compared to perfectly sharp edges. This finding potentially explains the differences between simulations with sharp edges and experimental results with less precise edges.

Chapter 3

Methodology

Computational Fluid Dynamics (CFD) is a lengthy process involving a sequence of meticulous steps. Prior to commencing the modeling and analysis of the flow around a rectangular cylinder, a series of challenges must be addressed.

The initial step involves establishing the set-up, which encompasses defining the computational domain along with its corresponding boundary conditions. Additionally, the properties of the simulated fluid and its characteristics need to be determined.

Once the domain is defined, the discretization into small cells begins : the meshing phase. Generating the mesh is a crucial step that dictates the resolution of the solution and the computational cost of the simulations. The parameters influencing this phase must be carefully and precisely defined.

With the domain meshed, the Navier-Stokes equations can be solved in each cell. The numerical solver, is presented below, along with its main features. The solver parameters also require careful consideration, especially the timestep, which significantly influences the numerical simulation's stability.

Having both the numerical domain meshed and the solver parameterized, the simulation can start. Before initiating the analysis, a qualitative and quantitative assessment of the results quality is performed. The domain, boundary conditions, and solver parameters are examined in an initial test run, to ensure that the physics under study is accurately modeled. Subsequently, the quality of the solution is observed and an iterative process on the mesh is conducted. The objective is to achieve the optimal balance between a well-refined mesh, high resolution and minimal computational cost.

3.1 Numerical domain

In the realm of numerical simulations, as well as experimental study, the selection of the set-up is critical. In the previous chapter, a concise overview of the diverse computational domains used by other researchers was presented. The sole variable studied was the spanwise dimension; no specific sensitivity analyses were conducted on the other dimensions of the domain. For these dimensions, only certain guidelines were deduced in the BARC benchmark based on the obtained results.

For the present study, conclusive data regarding the optimal domain size are lacking. Consequently, the decision was made to adopt the same domain sizes as in Bruno et al. [7]. This choice fell within a reasonable range, neither too small nor excessively large, and these specifications have already been adopted in several more recent studies.

The computational domain takes the form of a rectangle, as depicted in figure 3.1, with the following dimensions :

$$\begin{aligned} \frac{D_x}{H} &= 205 \\ \frac{D_y}{H} &= 155 \\ \frac{W}{H} &= 1 \end{aligned} \tag{3.1}$$

The span has been selected to be equal to the height of the cylinder. This geometric parameter is smaller than the spanwise dimension used in most studies. This reduction was primarily undertaken to mitigate the computational cost of this simulation. The effects of this spanwise length on flow phenomena will be studied within this thesis.

The dimensions of the cylinder - its length (L) and height (H) - are predetermined, aiming for an aspect ratio of 5:

$$\begin{aligned} H &= 0.2\ [m] \\ L &= 5H = 1\ [m] \end{aligned} \tag{3.2}$$

The positioning of the cylinder also constitutes a crucial parameter. The distance between the inlet boundary and the cylinder is set as follows:

$$\frac{\Lambda_x}{L} = 15 \tag{3.3}$$

Consequently, the coordinates of the bottom-left corner of the cylinder are:

$$(x\ ;y\ ;z) = (15.0\ ;15.4\ ;0.0) \tag{3.4}$$

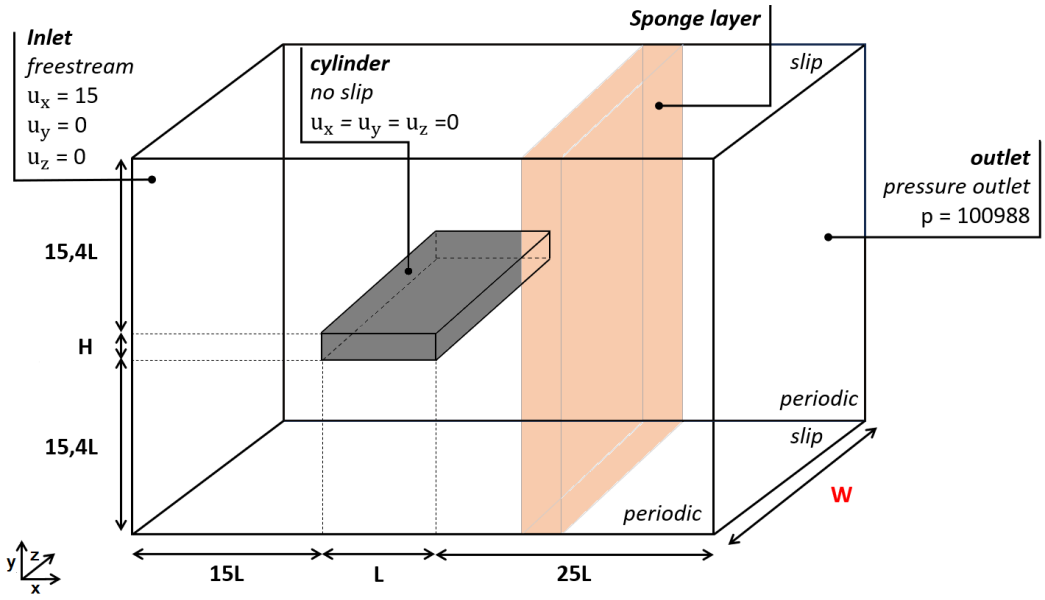

Figure 3.1: Computational domain, indicating major dimensions and boundary conditions (not to scale)

3.1.1 Boundary conditions

The boundary conditions are presented in figure 3.1. These choices are based on common practices used in previous studies, as well as the numerical solver employed in this study, Argo DGFluid. The boundary conditions model the interaction of the flow with domain walls.

Freestream

For the freestream conditions, various properties of the flow need to be determined. Two variables were imposed during the set-up of the Jules-Vernes Benchmark: the freestream velocity and Reynolds number in relation to the cylinder height (H):

$$\boldsymbol{u} = (U_\infty \,; V_\infty \,; W_\infty) = (15.0 \,; 0.0 \,; 0.0) \; [m/s] \tag{3.5}$$

$$Re_H = 2 \times 10^5 \; [-] \tag{3.6}$$

To compute the other properties required for our solver, several assumptions were made. First, the freestream fluid was assumed to be air, treated as an ideal gas:

$$p = \rho R_{s,air} T \tag{3.7}$$

Some constants (at ambient temperature) are also defined:

$$\begin{aligned} \gamma &= 1.4\ [-] \\ R_{s,air} &= 287.1\ \left[\frac{J}{kgK}\right] \\ \rho_{air} &= 1.2\ \left[\frac{kg}{m^3}\right] \\ Pr &= 0.707\ [-] \end{aligned} \tag{3.8}$$

With these assumptions, the dynamic viscosity of the fluid can be computed:

$$\mu = \frac{\rho_{air} U_\infty H}{Re_H} = 1.8 \times 10^{-5}\ \left[\frac{kg}{ms}\right] \tag{3.9}$$

Using the dynamic viscosity, the thermal conductivity of the fluid is computed:

$$\kappa = \frac{c_p \mu}{Pr} = 0.025583\ \left[\frac{W}{mK}\right] \tag{3.10}$$

Finally, assuming an incoming flow Mach number of 0.0437, the temperature is obtained using the Mach law:

$$T_\infty = \gamma R_{s,air} \left(\frac{U_\infty}{M_0}\right)^2 = 293\ [K] \tag{3.11}$$

And with the temperature, using the ideal gas law 3.7, the pressure is computed:

$$p_\infty = \rho_{air} R_{s,air} T_\infty = 100989\ [Pa] \tag{3.12}$$

No-slip condition

On the faces of the cylinder, a no-slip condition is imposed. This condition models a solid wall boundary, where the fluid velocity is equal to the solid boundary's velocity:

$$\boldsymbol{u} = (u_x; u_y; u_z) = (0; 0; 0) \tag{3.13}$$

Slip condition

On the top and bottom boundaries of the domain, slip boundaries are imposed. This condition models solid walls, similar to the no-slip condition, but with a difference in flow velocity from the wall velocity. This difference in velocity is the slip (β_s) of the fluid on the solid boundary.

The flow velocity vector can be divided into two parts. The velocity normal to the wall is null, as the boundary is a solid wall without through flow. As depicted in figure 3.2, the fluid velocity tangent to the wall is non-null. The equation that models this boundary condition is as follows, with the slip factor (β_s):

$$\begin{aligned} u_y &= 0 \\ u_t &= \beta_s \left(\boldsymbol{u} - u_y \right) \cdot \boldsymbol{n_{wall}} \end{aligned} \tag{3.14}$$

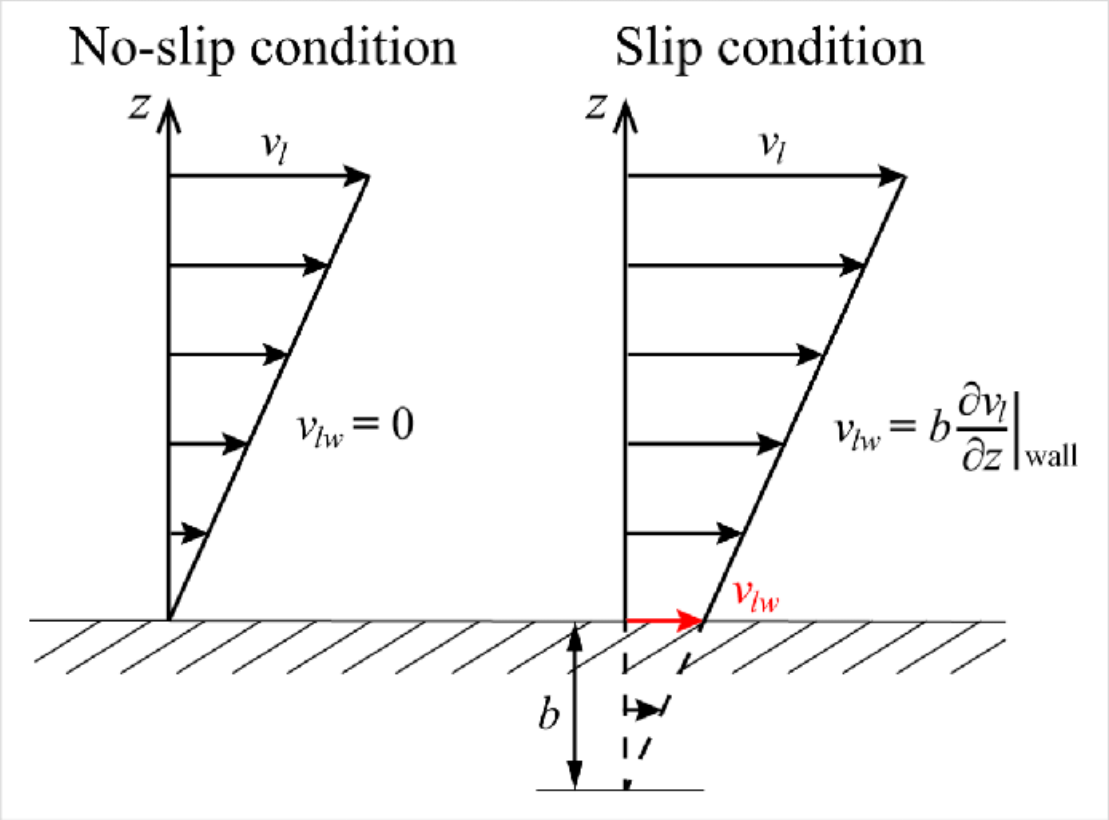

Figure 3.2: Schematic of the no-slip and slip boundary conditions. Scientific figure from ReserachGate, available at:

Periodic condition

The faces in the spanwise dimension are set to be periodic. The periodicity of these boundaries ensures identical flow conditions on both sides. This condition is directly modeled in GMSH, adhering to the equation:

$$\boldsymbol{u}(x, y, z) = \boldsymbol{u}(x, y, z + W) \tag{3.15}$$

Pressure outlet

For the outlet, only the desired pressure at the end of the domain is specified. This pressure is set to be the same as the inlet pressure, considering ambient conditions far behind the cylinder:

$$P_{out} = P_{ref} = 100988.7\ [Pa] \tag{3.16}$$

Sponge Layer

The discretization of the mesh plays a significant role in determining the precision of the solved flow but is the main factor affecting the computational cost. A more refined mesh offers greater precision but requires more time for simulation. Efficiency necessitates making concessions in some parts of the domain. However, if excessive vortices persist with larger mesh sizes, it could be problematic.

To dissipate these vortices beforehand, a sponge layer is employed. This layer absorbs and rapidly dissipates all vortices. This dissipation is achieved using damping by introducing a source term penalizing the difference between the local and time-average solutions. The damping factor is a function of spatial variables and is given by :

$$\sigma = 40 * 0.5 * (1 + tanh(1000 * (x - x_{in})/(x_{out} - x_{in}))) \tag{3.17}$$

Assuming that the sponge layer starts at $x_{in} = 17.8$ and ends at $x_{out} = 22.8$.

3.1.2 Mesh

With the domain boundaries and dimensions defined, the next step involves generating the mesh. This task is accomplished using the GMSH software [11]. The meshing of the domain requires striking a balance between precision and computational cost. The Navier-Stokes equations are solved within each cell; hence, the solution's accuracy depends on the cell size. Conversely, the computational cost is largely influenced by the number of cells within the domain.

Balancing computational cost and precision is a challenging process. During this thesis, three meshes were refined, and the solutions obtained from their simulations were compared. Each of these three meshes has its specifications, ranging from less refined to more refined, as presented in table 3.1. The mesh presented hereunder, along with the images, is from the third mesh with specifications 3.

The x-y plane of the domain is meshed as depicted in the figure 3.5. The critical region is the vicinity of the cylinder. More specifically, the phenomena to be captured occur in two distinct zones: the upper and lower faces of the cylinder on one hand and the wake behind the cylinder on the other. Each of these regions was treated differently.

Concerning the cylinder's faces, a body-fitted structured mesh is first generated, known as the boundary layer. The dimensions of the first cell - normal to the wall (dy_0) and tangent to the wall (dx_0), as shown in figure 3.3 - for the three specifications are presented in table 3.1. The growth rate of the cells in the normal dimension to the wall, as well as the thickness of this boundary layer, is also provided. The structured mesh in this zone grows until dy = dx, yielding isotropic cells in the plane.

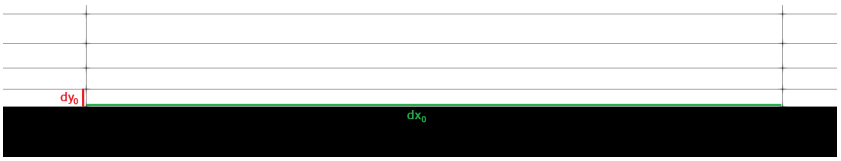

Figure 3.3: First cells on the side of the surface of the cylinder

The boundary layer around the cylinder takes on a C shape, extending continuously between the top, front and bottom faces, as pictured in figures 3.4 and 3.5. Around the corners of the front edges, refining the structured mesh becomes arduous. Within the GMSH software [11], a feature is present to mesh the boundary layer around the corners with a fan configuration. This fan is shown in figure 3.4. The straight angle of the cylinder is meshed using six cells, dividing the 90° arc circle. While more cells could be beneficial, using six cells already produces a well-refined mesh near the edges. Moreover, it is unnecessary to employ more refined cells further away in front of the cylinder's front edges, where the flow is less turbulent.

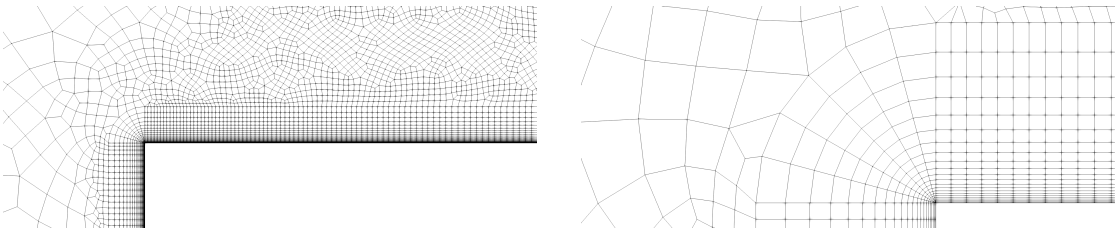

Figure 3.4: Structured mesh around the faces of the cylinder (left) and zoom on the fan configuration at the front edge (right).

When moving away from the upper and lower surfaces of the cylinder, the detached shear layer needs to be captured. The size of the cells just outside of the boundary layer structured mesh for all specifications is detailed in the table 3.1.

Only a small region around the shear layer is refined. Further, the mesh size increases rapidly to reduce the computational cost of these calmer zones. Since refining the mesh with small cells in regions far from the cylinder is unnecessary, these areas are meshed with cells as large as 4 times the cylinder's length (L). While the mesh is less accurate, it suffices to capture the flow in the distant regions.

Ensuring the continuity of the boundary layer with fans at the rear edges of the cylinder is inconceivable due to the high turbulence intensity in this region. The precision of the fan configuration is insufficient to accurately capture this turbulence. Additionally, the cells resulting from the fan have unfavorable shapes that could lead to numerical instability. Therefore, behind the cylinder, an unstructured mesh with progressively refining cell sizes is employed. The first cells at the edges have a size of dy_0, capturing the small flow variations in this highly turbulent zone. The cell size growth reaches up the 0.06/H when further into the wake.

In this master thesis, the simulation is three-dimensional, to capture all the effects of the turbulence. The mesh presented here above is in the x-y plane and thus two-dimensional. A extrusion is performed from this mesh in the spanwise direction. The size of the extrusion is the length of the span (W), equal to one height of the cylinder (H) for all meshes. In the spanwise dimension, the mesh is therefore structured, with a constant spacing (dz). The dimensionless spanwise discretization (dz/H) for each of the three meshes are presented in the table below 3.1.

	First cell dimensions			Boundary layer		Cells sizes	
	dy_0/H	dx_0/H	dz/H	Ratio [%]	Thickness/H	ShearLayer/H	Wake/H
Specs 1	0.00075	0.03	0.03125	12	0.3	0.06	0.06
Specs 2	0.0005	0.02	0.02	19	0.14	0.06	0.06
Specs 3	0.0005	0.02	0.02	19	0.14	0.02	0.06

Table 3.1: Meshes specifications

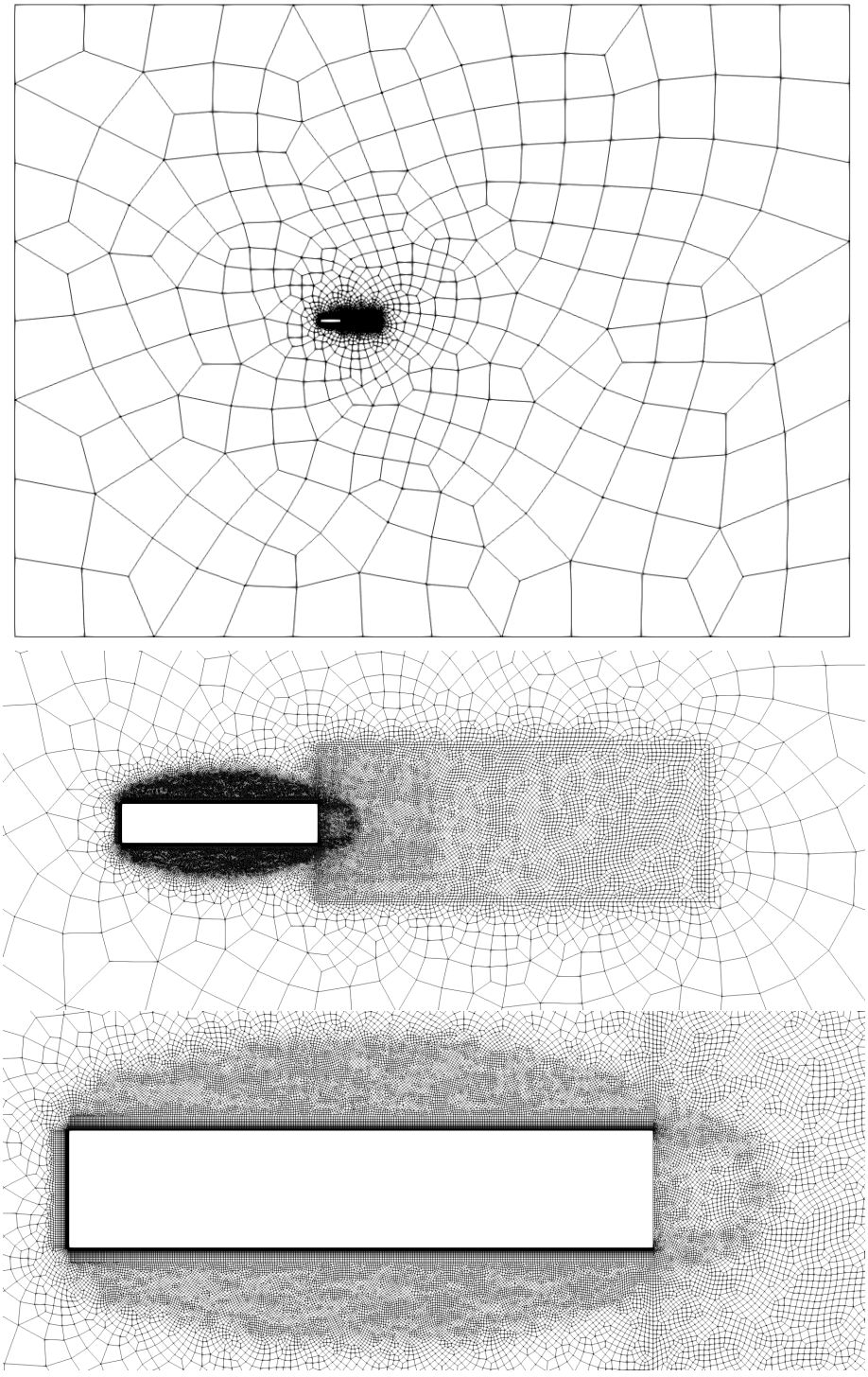

Figure 3.5: Meshing cells in the x-y plane around a 5-1 rectangular cylinder, following the specifications 3.

3.2 Numerical solver

The numerical solver used for this simulation is Argo DGFluid, developed by Cenaero. This code develops and solves the Navier-Stokes equations with the use of the Discontinuous Galerkin discretization. This implementation is conducted with a finite volume method (FVM) at the surfaces of the elements. The flow inside the elements is solve with a finite element method (FEM).

A spatial discretization order of p = 3 is chosen for the solver division of each elements. This implies that every cells of the mesh is divided in three equivalent section, leading to p+1 degree of freedom for every elements.

The diffusive term is discretized using IIPDG, Incomplete Interior Penalty for Discontinuous Galerkin scheme. While the temporal scheme used is the Backward Differentiation Formula 2 (BDF2), with an implicit strategy. The non linear solver uses the Newton method, with the generalized minimal residual method (GMRES) to solve the linear equations.

CFL and timestep

With the solver defined, one last parameter needs to be determine for the simulation to properly run, the time step (Δt). It is not easy to determine the best value to use as it depends on many factors. However, a minimum can be determined by using the Courant-Friedrichs-Lewy condition, the CFL:

$$CFL : \Delta t \left(\frac{u_x}{\Delta x} + \frac{u_y}{\Delta y} + \frac{u_z}{\Delta z} \right) \leq C_{max} \tag{3.18}$$

Since the solver uses a implicit scheme (BDF2), and is unconditionally stable, the CFL is not a requirement, but it gives a good first guess. This condition has to be respected in every cells of the mesh, the time step is thus vastly influenced by the higher speed and the smallest cell size. The speed is not expected to raise above the freestream velocity with exaggeration. The smallest cell size is $dy_0/H = 0.00075$ and assuming a one-dimensional flow near the wall with velocity $u_y = 15$ [m/s], the CFL reduces to:

$$\Delta t \leq C_{max} \left(\frac{dy_0}{u_y} \right) = 5 \times 10^{-6} \tag{3.19}$$

With a value of $C_{max} = 0.5$ to ensure the reliability, the time step of the simulations is determined.

3.3 Mesh iterations

This final step involves analysis the initial results from the simulations. The simulation is conducted multiple times, initially through test runs aimed at evaluating the proper implementation of the boundary conditions and the solver parameters. These test runs also provides a first feedback on the domain size, indicating whether it needs to be expanded or reduced, before proceeding to subsequent iterations.

Once the solver's readiness is confirmed, the actual simulation commences. An iterative process is also applied on the mesh to fine-tune and achieve the desired quality. This iterative process resulted in the first and second mesh specifications. The first mesh prioritizes a lower computational cost, while the second leans more towards a precise solution. Both of these meshes are initiated from the same starting point that accumulates all the previous iterated meshes not presented in this report.

The third mesh represents an upgrade version of the second, retaining some specifications while refining others. The refinement is guided by qualitative and quantitative analysis that will be detailed below. These analysis aimed to achieved optimal refinement, building upon the foundation provided by the first and second specifications, while minimizing the computational expenses.

The mesh resolution was determined from two sets of data. The first set focuses on the resolution at the wall of the cylinder. Specifically, attention is directed towards the dimensionless x, y, and z distances. Particular emphasis is placed on the normal wall dimension. The second aspect involves a qualitative observation of the flow vorticity resolution in critical regions surrounding the cylinder.

3.3.1 Wall resolution

The velocity at the wall of the cylinder is set to null, a condition applied to model the underlying physics. This condition induces friction between the fluid and the surface. In 1930, the first version of the law of the wall was published, it provides a relationship between the average velocity at a point near the wall and the distance from that wall :

$$u^+ = \frac{1}{\kappa}\, ln(y^+) + C^+ \tag{3.20}$$

Where κ is the von Karman constant and C^+ is a constant.

The distance to the wall (dy) is made dimensionless ($\boldsymbol{y}^+$) and is calculated using the friction velocity ($\boldsymbol{u_\tau}$) and the kinematic viscosity of the fluid (ν) :

$$y^+ = \frac{dy\ u_\tau}{\nu} \tag{3.21}$$

The friction velocity is derived from the wall shear stress (τ_w), which is computed from the friction between the wall and the fluid :

$$u_\tau = \sqrt{\frac{\tau_w}{\rho}} \tag{3.22}$$

The law of the wall provides insight into the dimensionless distance normal to the wall ($\boldsymbol{y}^+$) describing the flow region at that distance. The near-wall region is divided into three zones : the viscous sublayer, the buffer layer and the log-law inner layer. The limit of the viscous sublayer extends up to $\boldsymbol{y}^+ < 5$.

The dimensionless distance in the y direction of the first cell ($\boldsymbol{y_0^+}$) is a crucial variable to monitor in CFD. The objective is for the first cell to remain completely is this viscous sublayer to ensure a good resolution of the flow near the wall. A mean value of $\boldsymbol{y_0^+} = 1$ is a reasonable target.

As explain, the dimensionless distance of the first cell normal to the wall ($\boldsymbol{y_0^+}$) is computed using the shear stress exerted on the surface by the fluid. Figure 3.6 illustrates the time-average values of this parameters on the lower and upper surfaces of the cylinder for both the first and third simulation specifications. The dimensionless distance is divided by the spatial discretization order of the solver (p=3).

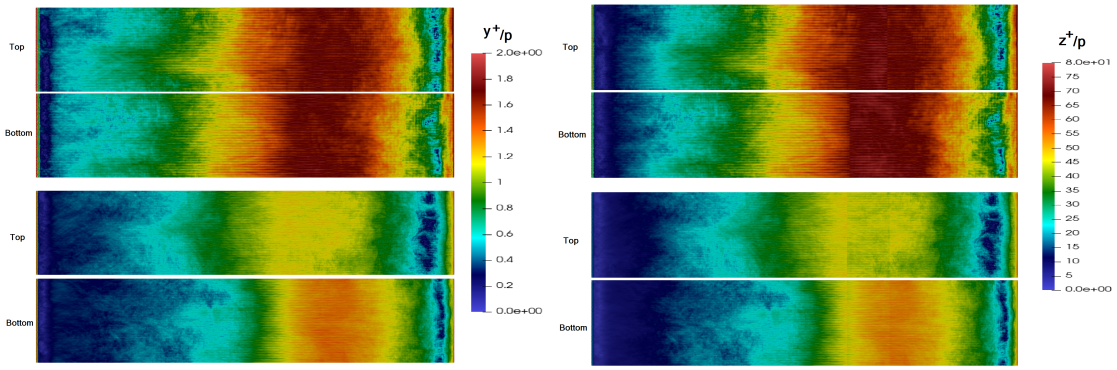

Figure 3.6: Wall resolution - normal $\boldsymbol{y_0^+}$/p (left) and tangent $\boldsymbol{z_0^+}$/p (right) - for the top and bottom surfaces : first (above) and third specifications (below).

In both cases, the values for the first halves of the cylinder's face are either below or well below the threshold value of 1. For the second halves, while the values differ between bottom and top surfaces, the improvement from the first specifications is evident. However, even with this enhancement, the mean value of the dimensionless distance in this section remains above unity.

A similar observation is made when comparing the three simulation specifications in figure 3.7. The graph illustrates the distribution on the surface of the dimensionless distance of the first cell ($\boldsymbol{y_0^+}$), averaged in time, span and over the upper and lower surfaces of the cylinder. From these plots, two key values can be extracted: the peak value and the mean of the normal dimensionless distances. The values for the three specifications are presented in the table 3.2. With the improved near-wall

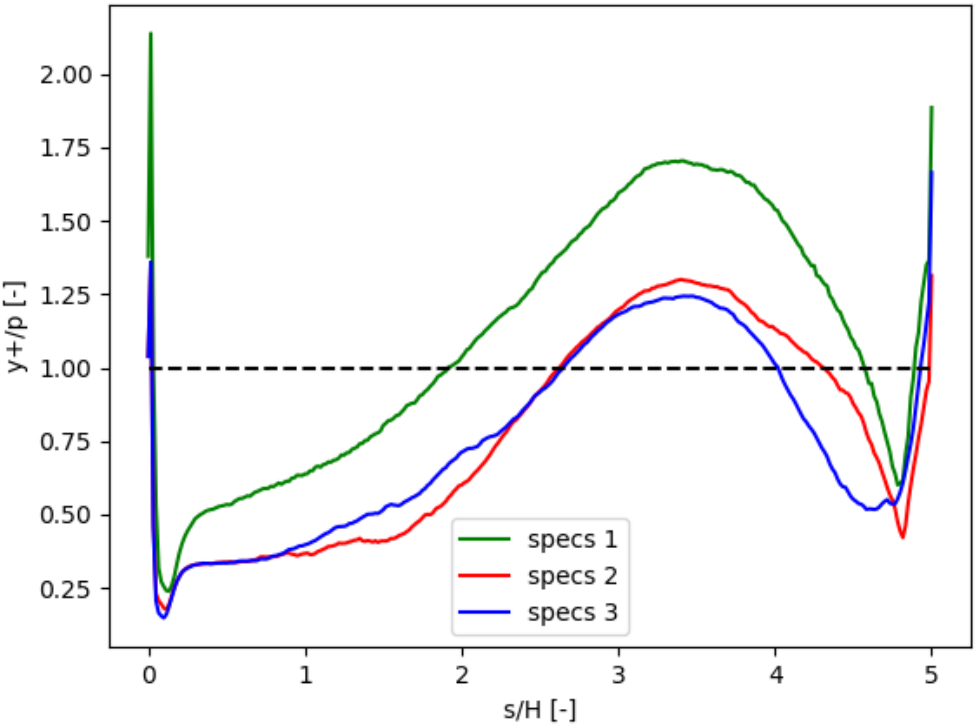

Figure 3.7: Distribution of the dimensionless $\boldsymbol{y_0^+}$ average in time, span and over the upper and lower surfaces of the cylinder.

resolution, the objective is not fully achieved everywhere, but it is approaching that goal. Moreover, the mean value over the cylinder's wall face is satisfactory, even for the first specification.

While the distance normal to the wall is of primary interest and requires careful consideration, the tangent dimensions are also significant. The time-average mapping of the spanwise dimensionless distance of the first cell (z_0^+) is depicted on the right part of the figure 3.6. The span dimension is more critical to monitor due to its greater impact on computational cost.

Again, a comparison between the first and third specification reveals a significant drop as expected when the spanwise resolution is further increased. For LES case, a desirable range for the dimensionless distance of the first cell (z_0^+) is between 25 and 40. The graph below illustrates the surface distribution of the time-average, span-average and upper/lower surfaces-average values for the three specifications. The threshold value is achieved in all case for a substantial portion of the surfaces, and for the third and second specification, nearly everywhere.

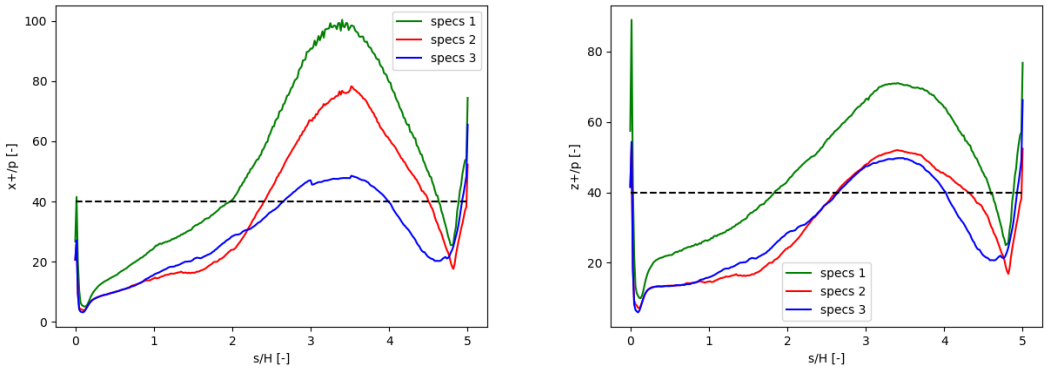

Figure 3.8: Distribution of the dimensionless x_0^+ (left) and z_0^+ (right) average in time, span and over the upper and lower surfaces of the cylinder.

The mean and maximum values of the dimensionless distance in the x and z dimensions are also provided in the table 3.2. While the second and third specifications share a similar near-wall resolution, the x dimensions exhibit significant dispersion, as observed in the table.

Simulation	avg(y_0^+)	max(y_0^+)	avg(x_0^+)	max(x_0^+)	avg(z_0^+)	max(z_0^+)
Specs 1	1.095	1.662	51.59	96.57	45.62	69.25
Specs 2	0.763	1.255	36.93	71.41	30.51	50.19
Specs 3	0.745	1.212	28.71	47.04	29.81	48.48

Table 3.2: Dimensionless distance surface statistics

3.3.2 Flow vorticity resolution

In this section, a qualitative observation of specific regions around the cylinder is describe. These observations from the first and second specifications led to the development of the third mesh specifications.

Detached shear layer

At the front edge of the cylinder, the shear layer detaches, resulting in the formation of most of the vortical structures observed along the cylinder's faces. These structures must be adequately resolve along the entire shear layer. Insufficient cell resolution in this region would lead to vorticity dissipation and information loss.

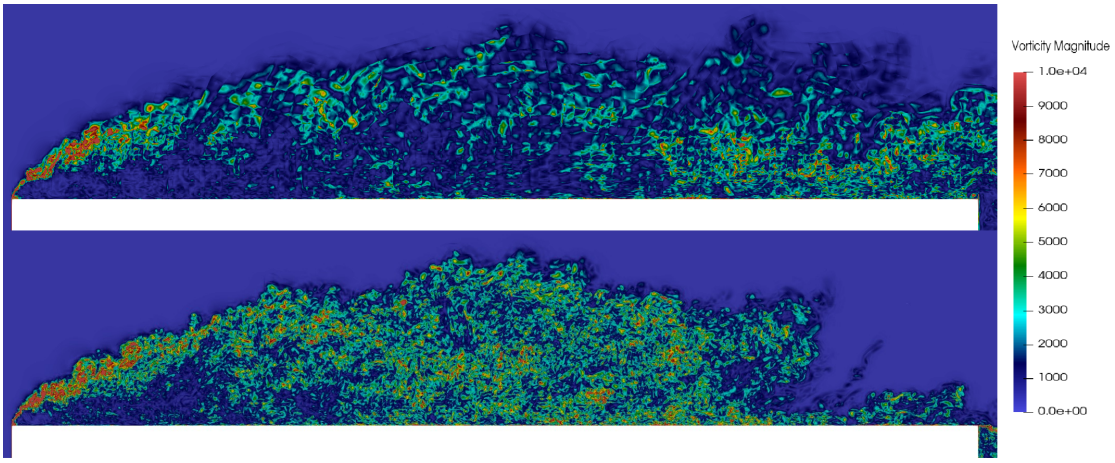

Figure 3.9: Instantaneous vorticity at t = 1.35 [s] of the detached shear layer for the first specification (top) and the third specification (bottom).

A comparison between the first and third specification is shown in figure 3.9. The refinement of the second specifications in the detached shear layer region is similar to that of the first specifications. As observed, the development of vorticity in the first simulation is considerably diminished compared to the third specifications. The mesh cells sizes in this region was reduced by a factor of three in the x and y dimensions for the third specifications.

Zooming near the front edges, as shown in figure 3.10, the detachment of the shear layer is observed. Initially, no substantial difference is observed between the two meshes. In both case, the structured mesh cell sizes remain small, even in the first specifications. However, when the shear layer exits this region, an almost immediate dissipation of vortical structures in the mesh becomes noticeable.

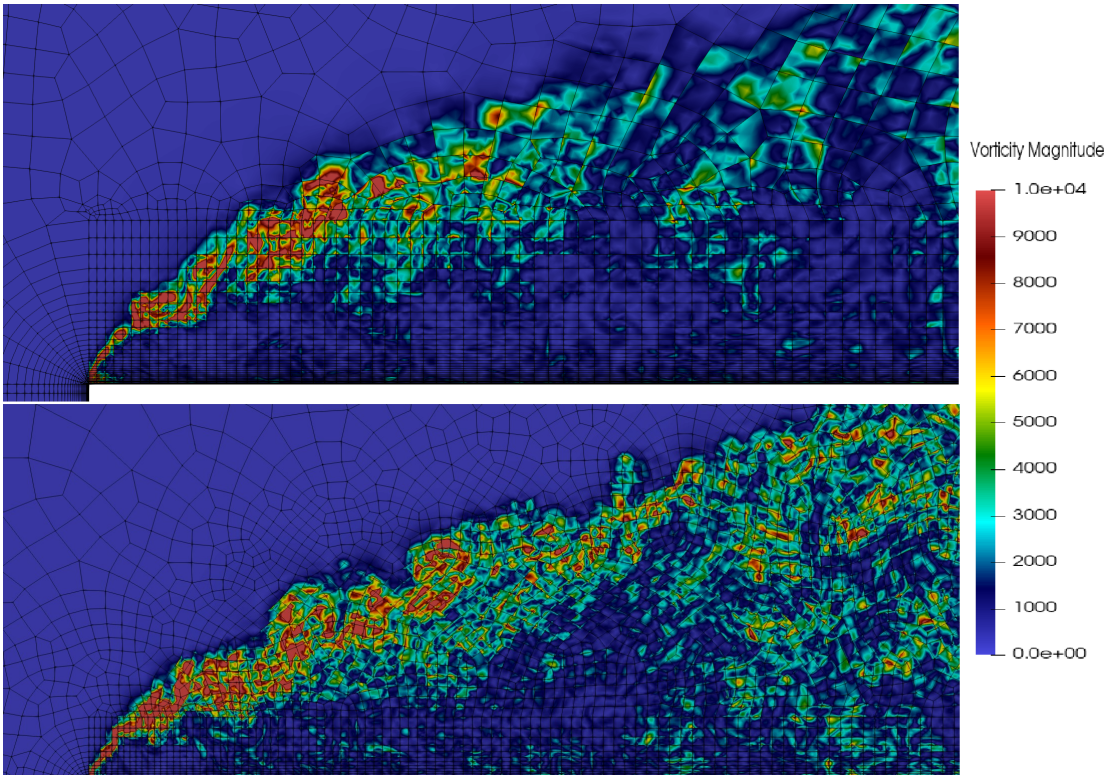

Figure 3.10: Instantaneous vorticity at t = 1.35 [s] near the front edge of the cylinder. The first specification (top) and third specification (bottom) are depicted.

Similar observations can be made near the end of the cylinder's face. The vortical structures develop again upon entering the structured mesh. While the precision is lower than that of the third specifications, it represents a significant improvement over the region outside the structured mesh.

The structured boundary layer was left unchanged from the second to the third specifications, and from the observation made, it appears sufficient in this regions The improvement in the shear layer region is substantial in the third simulation. A considerable amount of information was dissipated in the two previous mesh, and this correction is expected to contributes significantly to the solution precision.

Trailing edge vortex shedding

Vortex shedding around the rectangular cylinder with an aspect ratio of 5 occurs at both the leading and trailing edges. The mesh in this region is unstructured, and the first cells near the edges are very small, of size dy_0, in all cases. However, further down the wake, cell growth is less pronounced in the third mesh.

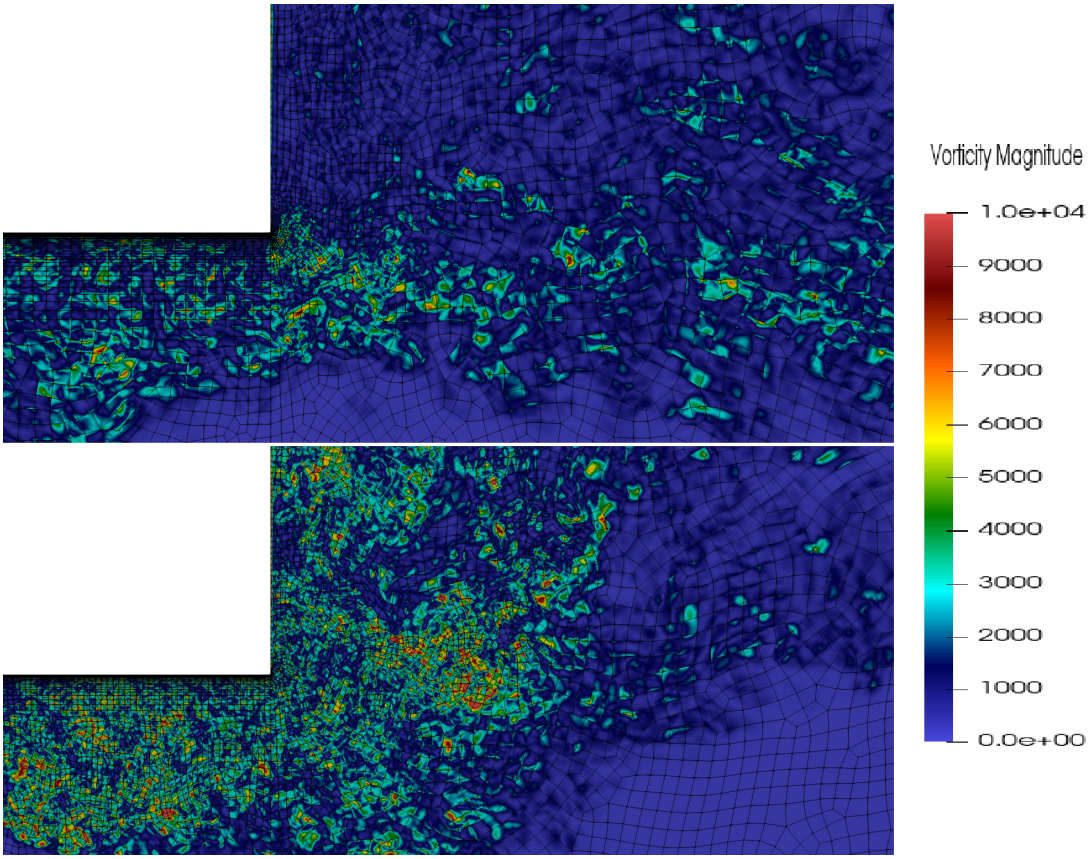

Figure 3.11: Instantaneous vorticity at t = 1.35 [s] at the trailing edges of the cylinder. The first specifications (top) and third specification (bottom) are mapped.

Figure 3.11 present the instantaneous vorticity at the trailing edges for the first and the third specification. Once again, the first specifications exhibits a clear sign of rapid vortical structure dissipation in the wake. The precision near the end of the cylinder's bottom and top faces is also notably low. Consequently, the mesh size growth was reduced in the third mesh specifications to mitigate this dissipation.

In the third mesh, while the result is not perfect, further refinement could potentially capture more information. However, most of the vorticity is captured, and the computational cost of refining even more would be prohibitively large compared to the gains.

Sponge Layer

In the wake, a sponge layer is present to dissipate the remaining turbulence before the refinement becomes too coarse. In the first and second specifications, this zone is placed not too far from the cylinder's rear face. The effect, as shown in figure 3.12, is a dissipation of vortical structures before a complete vortex cycle can be observe. For the third specifications, the sponge layer zone was moved farther back,

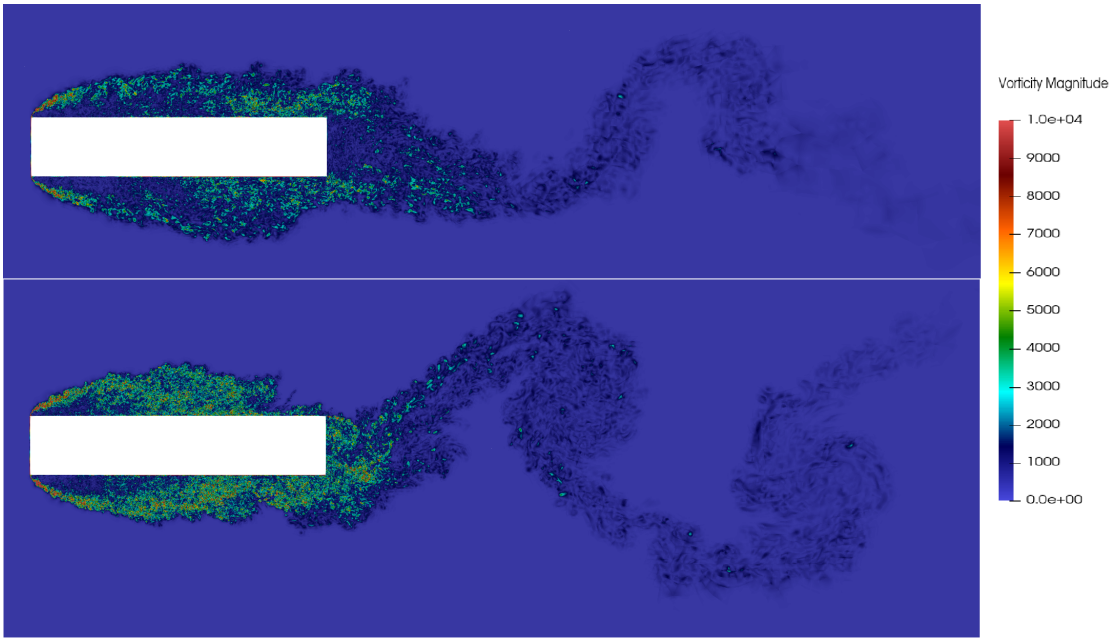

Figure 3.12: Instantaneous vorticity at t = 1.35 [s] around the cylinder and with the wake region. The first specifications (top) and third specifications (bottom) are presented.

and the refinement was extended slightly. This adjustment ensures the capture of an entire turbulence oscillation of the von Karman vortex street. Although the impact of such change may be minor, the computational cost was relatively low compared to the others applied modifications to the third specifications.

Of course, the mesh in the wake could be significantly more refined, adding substantial precision to the results. However, the cost of such refinement is beyond the available resources.

3.4 Zenobe and Lucia

The simulation were conducted on "Zenobe" first and then "Lucia" supercomputers, with high performance computing (HPC). Both of these supercomputer are under the supervision of Cenaero. The supercomputer "Zenobe", was baptised after Zenobe Gramme, a Belgian electrician. It is composed of 14000 processors, with a high performance storage capacity of 350 To in addition to the 120 standard storage. The infrastructure was connected to the Belgian network with high speed (1 Gbps) and was disconnected this year.

The new supercomputer launched earlier this year is called "Lucia" in memory of Lucia De Brouckère. This infrastructure connected at higher speed to the belgian network (10 Gbps) is constituate of a CPU partition containing 300 nodes. In each of these nodes, 128 processors are connected with an available memory per node of 240 GB.

If the initial simulations were conducted using Zenobe, the three simulations specifications presented before were performed on Lucia. For the results presented in the following chapter, some characteristic of the resource required to perform the simulations are presented in the table below 3.3.

Simulation	Partitions	Processors	t_{real} [d]	$t_{CPU,total}$ [y]	t_{CPU}/ct [h]	ct
Specs 1	2048	4096	32.7	336.7	157k	20.4
Specs 2	2048	8192	29.8	669	372k	15.75
Specs 3	2048	8192	27	606	543k	9.78

Table 3.3: Some data on the computational time required to perform the simulations.

Chapter 4

Rectangular cylinders analysis

In this chapter, the results of the three simulations carried out with Argo DGFluid are comprehensively examined. The simulation outputs are processed to create a coherent dataset. This set serves as the foundation for the comparison of the results across the three simulations. Additionally, a comparison is made with results extracted from the existing literature.

In an initial phase, the monitors generated by the simulations are processed and compared. This analysis serves multiple purposes. Firstly, it offers insights into the reliability of the simulations results. Any substantial deviation from established results would prompt suspicion on the simulation set-up and solver employed and on the results. Secondly, the state of convergence of the simulations is assessed, determining whether the simulations have reached a stable and consistent outcome.

In the subsequent analysis, the mean flow characteristics surrounding the cylinder faces are extracted and examined. These features have historically exhibited significant variability across simulations and experimental findings in prior studies. The pressure distributions associated with these characteristics, derived from the three different meshes, are also scrutinized. Furthermore, this analysis delves into uncovering the root cause of the asymmetry observed between the flow features on the upper and lower surfaces of the cylinder.

The third set of results analyzed involves the pressure and velocity correlations in the spanwise dimension. A meticulous study of grid resolution is conducted, with the outcomes compared to the findings of previous analyses. This investigation seeks to shed light on the influence of grid resolution on pressure and velocity correlations and ascertain the level of agreement with earlier research.

4.1 Monitoring of integral parameters

In the field of computational fluid dynamics (CFD), the precision of simulations is evaluated by monitoring specific values at each timesteps. In this case, these values refer to the boundary fluxes observed at the inlet and outlet of the domain, as well as on the surfaces of the cylinder. These monitors provide pertinent data concerning the flow state at the boundaries. The quantities of interest include convective, diffusive, and pressure forces, in addition to the momentum of density, momentum, and energy stagnation density.

4.1.1 Forces analysis

From the monitoring files of the three simulations, the forces exerted by the cylinder on the flow can be computed. The lift force is obtained in the y-direction, while the drag force is in the x-direction. Using these forces, the dimensionless lift and drag coefficients are computed, taking into account the flow and domain characteristics:

$$C_L = \frac{L}{1/2\rho U L} \quad \textbf{and} \quad C_D = \frac{D}{1/2\rho U L} \tag{4.1}$$

The time histories of the lift and drag coefficients are plotted in figure 4.1. The left graph of the figure shows the time history of the first specifications simulation. The right graph illustrates the second simulation, followed by the third simulation after the dotted line. The simulation employing the third specifications was initialized using the results of the second simulation, which explain this choice of representation.

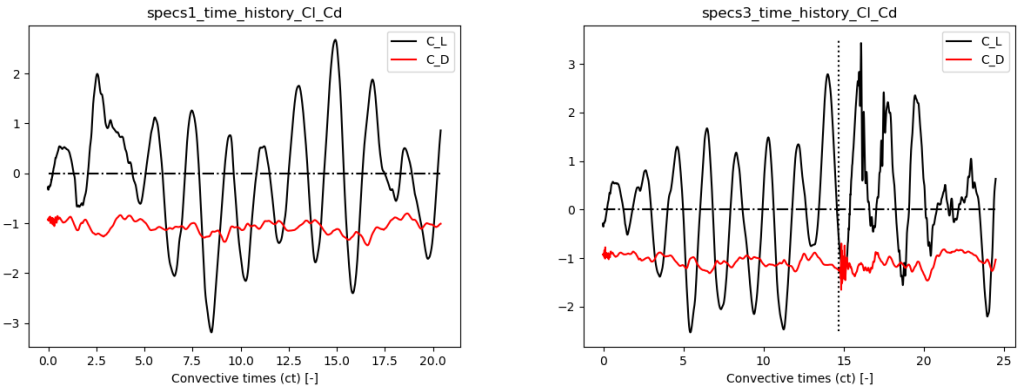

Figure 4.1: Time history of the lift (C_L) and drag (C_D) coefficients : the first specifications (left) ; the second specifications and the third one after the dotted line (right).

Both graphs are plotted as functions of convective times, which refer to the convective process. This metric is used to gain a better understanding of the actual simulation time computed. It represent the time required for a fluid particle at freestream velocity (U_∞) to traverse from the leading to trailing edges of the cylinder, spanning one length (L):

$$ct = \frac{L}{U_\infty}[s] \tag{4.2}$$

For the first specifications, a total of 20 convective times are accumulated. For the other two, shorter periods are accumulated with 15 and 7 convective times for the second and third simulations, respectively. This accumulation is reduced for the second specifications, because it transitioned to the third one which was deemed more significant. Due to computational limitations, both simulations could not be executed simultaneously.

Based on this accumulation, and on the monitoring of those values at each time step, an extensive dataset of lift and drag coefficients is obtained. Relying solely on time histories for comparing these datasets among themselves and with other research is somewhat intricate. Therefore, various statistical measures are extracted from the datasets, including the mean, the root mean square (RMS), and the standard deviation :

$$\overline{C_\alpha} = \frac{1}{N}\sum_{i=0}^{N} C_{\alpha,i} \tag{4.3}$$

$$std(C_\alpha) = \sqrt{\frac{1}{N}\sum_{i=0}^{N}\left(C_{\alpha,i} - \overline{C_\alpha}\right)^2} \tag{4.4}$$

$$C_{\alpha,RMS} = \sqrt{\frac{1}{N}\sum_{i=0}^{N} C_{\alpha,i}} \tag{4.5}$$

These statistics, computed for each simulations on the specified accumulation periods, are presented in the table bellow 4.1.

Case	Period [ct]	$\overline{C}_D$	std(C_D)	$C_{D,RMS}$	$\overline{C}_L$	std(C_L)	$C_{L,RMS}$
Specs 1	20	-1.072	0.127	1.080	-0.1219	1.185	1.192
Specs 2	15	-1.068	0.113	1.074	-0.1304	1.190	1.197
Specs 3	7	-1.088	0.163	1.100	0.258	1.129	1.158

Table 4.1: Statistical results from the monitoring of the lift and drag coefficient for the three meshes.

4.1.2 Frequency analysis

In addition to the statistics computed here above, the analysis of frequency behaviors can yield significant insights into the simulations. The discrete Fourier transform is employed to scrutinize the time histories. For a data set containing N discrete values of the coefficient (C_α), the Fourier coefficients (c_α) are computed with :

$$c_\alpha[k] = \sum_{n=0}^{N-1} C_\alpha[n] \cdot e^{i\omega_k} \qquad \textbf{for } k = 0, 1, 2, ... \ N \tag{4.6}$$

Where the respective frequency for each Fourier coefficient is determined by :

$$\omega_k = 2\pi k \frac{n}{N} \tag{4.7}$$

The Fourier transform returns N sets of Fourier coefficients and frequencies, however it is important to note that there is only N/2 distinct frequencies, due to the complex conjugate symmetry:

$$c_{\alpha,k} = c^*_{\alpha,N-k} \tag{4.8}$$

Thus, N/2 sets of Fourier transform amplitudes and corresponding frequencies are obtained. To facilitate comparison, a basis that considers the dataset size and simulation parameters is needed. The power spectral density (PSD) is used to compute the amplitude of the frequencies. It multiplies the amplitude of the Fourier coefficient by its complex conjugate and normalizes it by the number of samples:

$$psd = \frac{1}{N} c_\alpha \cdot c^*_\alpha \tag{4.9}$$

For the frequencies, dimensionless Strouhal frequencies are calculated using the freestream velocity (U_∞) and the height of the cylinder (H) :

$$St_H = \frac{fH}{U_\infty} \qquad \textbf{with} \quad f = \frac{2\pi}{\omega} \tag{4.10}$$

The frequency domains for the three simulations are illustrated in figure 4.2. The left side of the figure shows the entire frequency domains, while the right graphs provide a zoom to emphasize the principal frequency. This frequency represent the impinging of the shear layer on the upper and lower surfaces, the vortex shedding at the trailing edge, and the swirling vortices resulting in the wake. This principal dimensionless frequency from the lift analysis is the Strouhal number of the simulation. From the drag analysis, the principal frequency should give the half of the Strouhal number.

Both the Strouhal numbers for the lift and drag coefficient frequency analysis, as well as their respective power spectral density (PSD) are presented in the table 4.2. Upon a quick examination, it becomes evident that the Strouhal values computed from lift and drag are consistent only in the second simulation.

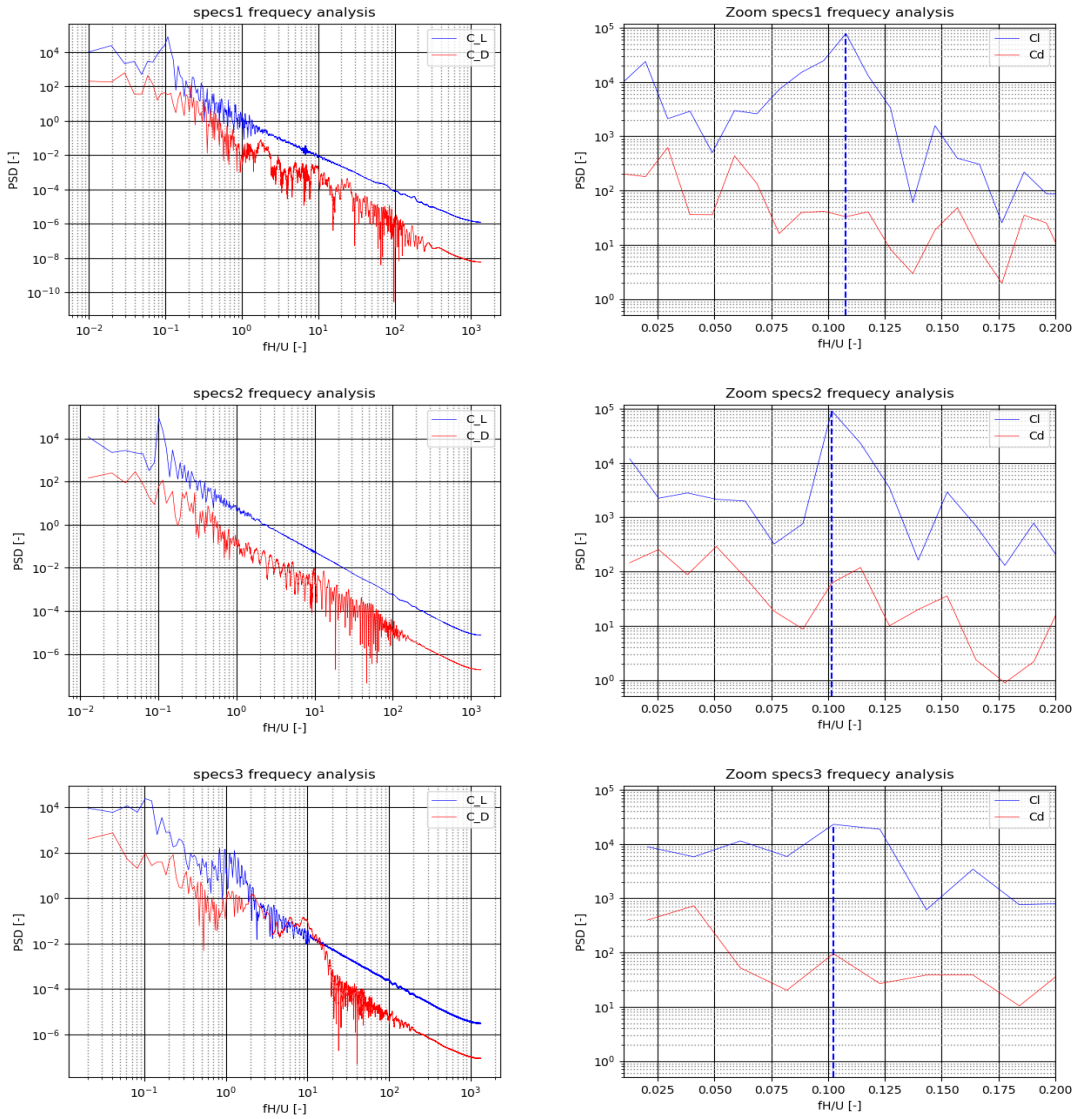

Figure 4.2: Frequency analysis for the three meshes simulations from top to bottom with the entire domains (left) and a zoom on the Strouhal frequencies (right).

Mesh	$St_H - C_L$	Amplitude-C_L	$St_H - C_D$	Amplitude-C_D
Specs 1	0.108	78141	0.059	619
Specs 2	0.102	91862	0.102	289
Specs 3	0.102	23040	0.082	727

Table 4.2: Strouhal numbers computed from the frequency analysis of C_L and C_D.

4.1.3 Time convergence

At high Reynolds numbers, the flow becomes highly turbulent. For this rectangular cylinder, an oscillatory phenomenon occurs in the wake, resulting in the well-known von Karman vortex street. This phenomenon arises from the main vortex rolling over the upper and lower faces of the cylinder. As these vortices are not synchronised, they influence the wake vortices sequentially. Due to the inverse rotation of the vortex shedding from the upper and lower surfaces, the wake rotation alternates between clockwise and counterclockwise. Consequently, the flow within the wake and along the cylinder's faces is in a constant state of change. This dynamic behavior prevents the simulation from reaching a stable and steady state.

However, despite the continuous oscillations and unsteady characteristics, the mean flow values slowly converge towards an equilibrium. At the start of the simulation, the boundary conditions need to propagate throughout the entire computational domain, exerting a significant influence on the flow statistics. Over time, this influence dissipates gradually until the instantaneous flow revolves around an equilibrium. This period between the start of the simulation and the equilibrium is referred to as the transient state.

This state is induced by two phenomena. In first, the propagation of the fluid particles through the whole domain is necessary. The changes in the mesh from coarser to finer, does not reset this propagation. Secondly, a rapid propagation of the characteristic lines of the flow, induced by any changes perform in the configuration set-up. The characteristic lines of the flow propagate through the domain at approximately the sound velocity, so they are rapidly dispersed.

To ensure the reliability of the results, it is crucial for the simulations to exit this state. It is worth noting that the time histories presented in figure 4.1 do not display the complete simulation history. The first and second simulations share the same starting point: the solution from previous simulations computed with coarser grids. As a result, a considerable portion of the transient state has already been simulated before the computation of the three simulations under investigation.

However, whenever there is a change is the mesh specifications, a change in the flow behavior occurs and need to be propagated, thus introducing a new transient state. To observe the exit of this state, the convergence of certain values are analysed. The key values of interest are the time-average lift and drag coefficients and the Strouhal number of each simulation.

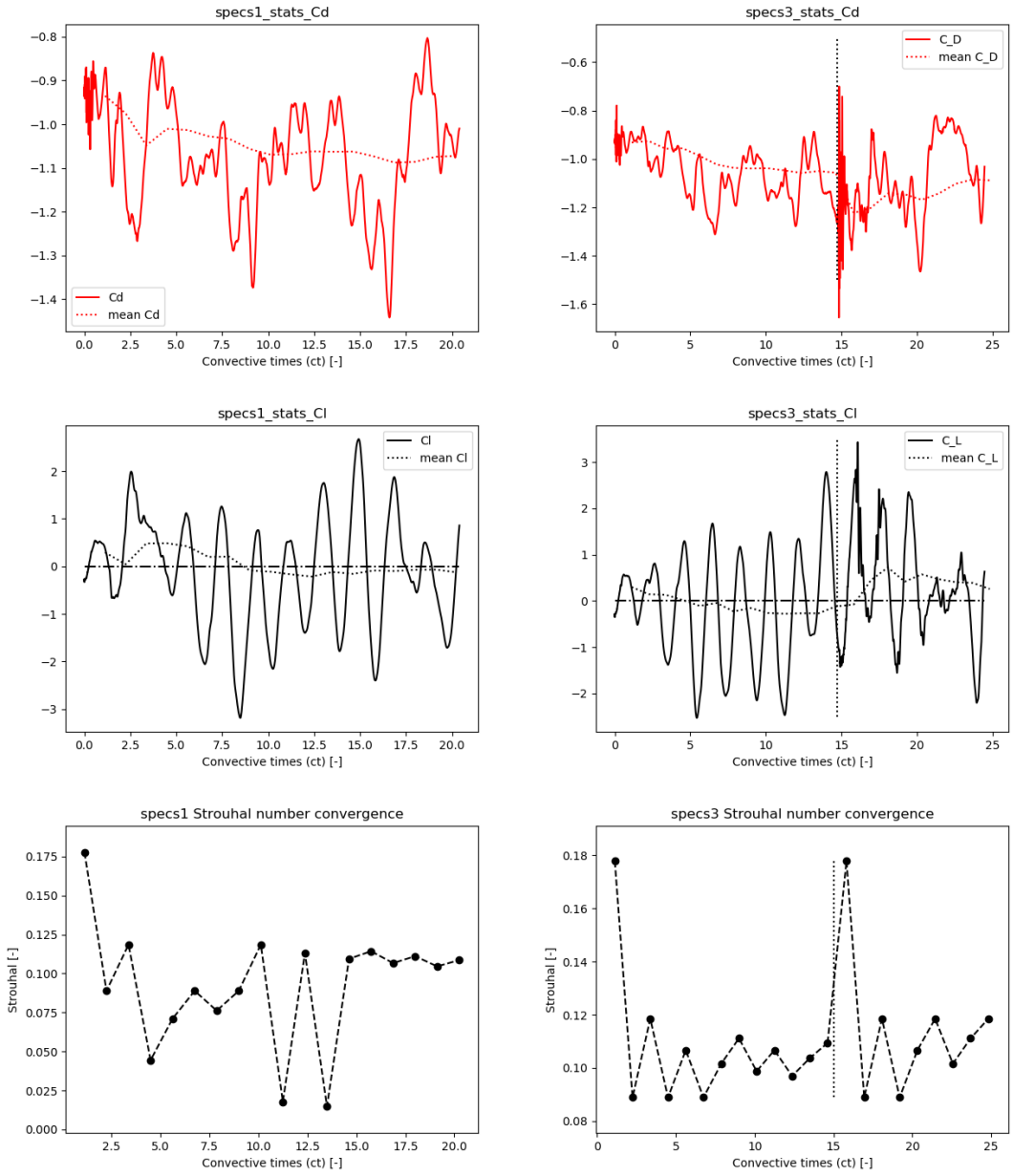

Figure 4.3: Time convergence of the lift (right) and drag (left) coefficients for the first (upper) and second plus third (lower) specifications

In figure 4.3, the time convergences of these values are plotted. For the lift and drag coefficients, the time histories were also displayed. This enables the observation of oscillation around the mean values. For the Strouhal number convergence, a frequency analysis is performed at several points in time. For each of these points

plotted, the cumulative period from all the preceding points is used for the frequency analysis. One additional convective time is add to the period accumulate between each points.

For the first specifications, convergence seems achieved after approximately ten convective times. Both the mean lift and the drag coefficient values have converged and oscillate around their respective time-averages. However, the Strouhal number has not yet reach convergence and appears to do so only after fifteen to eighteen convective times. It is important to note that since the values are computed based on the accumulation from the start, the convergence might be influenced by the initial values from the transient state.

In the case of the second simulation, the convergence behavior differs. The mean values of lift and drag coefficients converge faster, within six or seven convective times. The coefficients then oscillate around the mean values, displaying a more stable graph from the start of the simulation. However, the Strouhal number does not seem to converge at all during the accumulated fifteen convective times of simulation. The simulations features seems to have converged, but the occurrence of the Strouhal frequency remains puzzling.

For the third specifications, the lift convergence still descend towards zero, while the drag appears to have reach a plateau. The convergence is probably achieved, and the observation are a results of the initial transient state. The Strouhal number on the other hand also seems to not have reach convergence yet. Given the small amount of only ten convective times accumulated, such results could be expected.

The time statistics of the lift and drag coefficients and the Strouhal numbers are presented in the table below 4.3. The values between the statistics obtain from the entire period of accumulation are compared to those from a smaller period, discarding the initial transient state. The differences between the two sets of data are also computed, and they show little variations. The only parameters which is significantly impacted by the transient state appears to be the mean of the lift coefficient. The changes observed when the transient state is discarded are drastic in most of the simulations.

This shows two significant parameters on the statistical results. For the lift coefficient, the initial period and fluctuation due to the transient state has a large negative impact on the accumulated values. Another point less flagrant is that the Strouhal number only observed a dispersion for the third mesh when a period of only six convective times is used. However, no dispersion is observed in the second simulation Strouhal number although the accumulated period is only slightly higher.

An interesting point is also that the Strouhal remain the same although it was not converging in the graphs 4.3. This also shows the impact of the initial period on the statistical values. Following these observation, the minimal period of accumulation to compute a correct Strouhal number should be between six and height convective times, while excluding the transient state.

Case	Period [ct]	$\overline{C}_D$	std(C_D)	$C_{D,RMS}$	$\overline{C}_L$	std(C_L)	$C_{L,RMS}$	St_H
Specs 1	20	-1.072	0.127	1.080	-0.1219	1.185	1.192	0.108
	10	-1.077	0.136	1.085	-0.0630	1.214	1.216	0.108
Difference		0.4%	7%	0.5%	-48%	2.6%	2%	0%
Specs 2	15	-1.068	0.113	1.074	-0.1304	1.190	1.197	0.102
	8	-1.114	0.102	1.119	-0.0978	1.322	1.326	0.102
Difference		4.3%	9.7%	4.2%	-25%	11%	10.8%	0%
Specs 3	10	-1.088	0.163	1.100	0.258	1.129	1.158	0.102
	6	-1.053	0.173	1.067	0.0185	1.005	1.005	0.123
Difference		-3.2%	6%	-3%	-93%	-11%	-13%	20%

Table 4.3: Statistical results from the monitoring of the lift and drag coefficient for the three meshes. Comparison between the statistic obtain on the whole period and the statistic obtained from the converged period.

4.1.4 Mesh convergence

One of the objectives when running multiple meshes with different specifications is to compare them. In this section, the differences between the graphs and statistics computed earlier for the three meshes are compared. These observations are crucial to determine the impact of the mesh resolution and if the implied computational cost is worth it.

Firstly, a qualitative comparison of the time histories is performed. A striking difference is immediately pointed out. For the first two simulations, on the left graph and left part of the right graph of figure 4.1, the lift coefficient is surprisingly smooth. Small disturbance are indeed present at the start when the solver adapts the solution to the new mesh. However, these disturbance fade away almost immediately.

Conversely, for the third specifications simulation, after the dotted lines on the right graph of figure 4.1, the lift coefficient plot only slightly smooth down. In this case, high disruption are observed at the start. The commotions calm down when the simulation progress, but they never disappear unlike the other two cases. This

observation is a result that seems to fit more the physics, with the highly turbulent flow induced by the detached shear layer.

This difference remains relatively small, the primary oscillation of the flow does not vary much in the third specifications compared to the other two. An explanation for this difference is probably the resolution around the detached shear layer. As detailed previously, the refinement led to less dissipation of the vorticities in this region. These small vortical structures have a significant impact on the flow in their direct region but not on the global flow. With the lower resolution of the first and second specifications, most of the eddies developing are dissipated in the mesh around the shear layer. A lot of information is thus lost there, in the region right above and below the surfaces where the lift coefficient is monitored. This loss could explain the smoothness observed on the graphs.

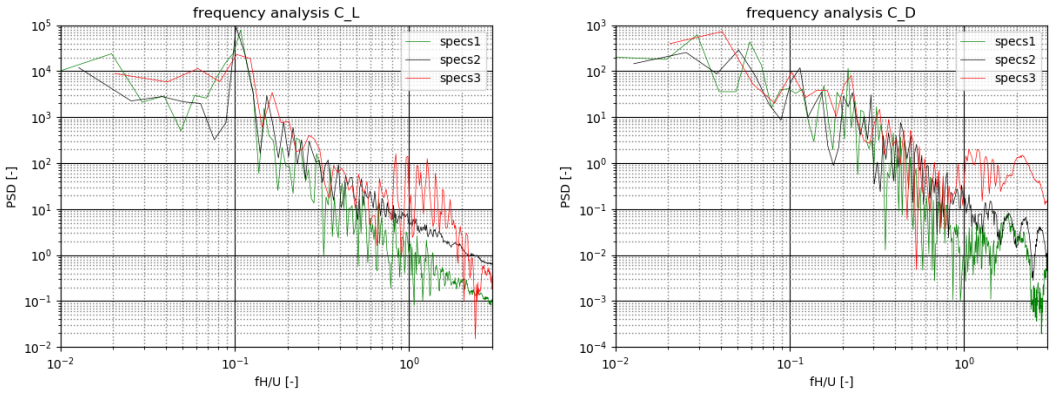

Figure 4.4: Frequency analysis comparison between the three specifications, from the lift coefficient (left) and from the drag coefficient (right).

In figure 4.4, the frequency analysis based on the lift and drag coefficients are compared between the three meshes. On this illustration, two differences of the PSD are obvious. The main Strouhal frequency PSD is lower in the third specifications compared to the first and second ones. This loss of amplitude could be caused by the smaller vortical structures captured by the third specification mesh. They disrupt slightly the main two-dimensional flow from which the Strouhal number is primarily computed.

Conversely, for Strouhal frequencies around unity, the third simulation PSD have values up to a hundred times higher. Again, the loss of the smaller vortical structures lead to a smoother flow. This smoothness implies that most of the flow features are regulate by the principal frequency. And this shows now on the bigger

frequency with a loss of amplitude while explaining the impact observed on the lift coefficient.

Similar observations are made on the frequency analysis pictured from the drag coefficients. The result are pretty similar when the frequency analysis is done, with mainly a big drop of amplitude on all the frequencies observed for the drag. However, the same observations as before for the main Strouhal frequency and the frequencies close to unity are observed.

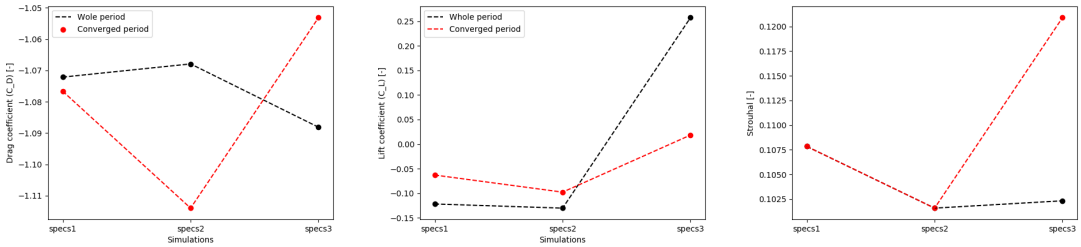

Figure 4.5: Mesh convergence of the simulations statistics : the drag coefficient (left), the lift coefficient (center) and the Strouhal number (right).

In the previous section, the time convergence of the simulations primary statistics was explored. An interesting part of simulating three mesh with upgrading resolutions is to observe the statistics convergences with the mesh resolution. The figure 4.5 illustrates the mesh convergence of the lift and drag coefficients, and the Strouhal number. Two sets of values were used, the first deduced from the whole period accumulated while the second on a reduced period excluding the transient state.

An observation is that the values does not show a flagrant convergence. The deviations observed between the first and second simulations are in opposite direction compared to the result of the third specifications. The second specifications appears to give worse results compared to the first one.

However, the deviations in results from the first to the second simulations are small. The main difference between these two meshes was the resolution of the near wall region. This could imply that the resolution selected in the first mesh specifications could already be enough as this sole modification does not upgrade the results precision. It is important to note that the second simulation accumulation was smaller than the first one. The results precision could be wronged due to this fact.

The third simulation also had a smaller accumulation period but still gave better results. However, the significant drop between both results of the third simulations is mainly caused by this smaller period of accumulation. If the results remains better thanks to the higher resolution of the mesh around the shear layer, the small period significantly impact the reliability of the statistics.

To conclude on the resolution of the mesh, two primary observation need to be recall. Firstly, the mesh resolution around the shear layer seems to improve drastically the results of the simulations. The sole resolution of the near wall region without touching the shear layer mesh does not yield any positive results. It only raises the computational cost of the simulation leading in fact to worse results. This puts here again an emphasis on the importance of the period of accumulation and its key role in the results accuracy.

4.1.5 Comparison with literature

After an analysis of the resolution of the meshes, a comparison of the time and frequency statistics with the results of the literature is performed. The several statistical values of interest computed previously are recalled in the table below 4.4. An ensemble average on the results obtain from the three simulations is also computed to compare it to the BARC ensemble average.

Case	Period [ct]	$\overline{C}_D$	std(C_D)	$C_{D,RMS}$	$\overline{C}_L$	std(C_L)	$C_{L,RMS}$	St_H
Specs 1	20	-1.072	0.127	1.080	-0.1219	1.185	1.192	0.108
Specs 2	15	-1.068	0.113	1.074	-0.1304	1.190	1.197	0.102
Specs 3	7	-1.088	0.163	1.100	0.258	1.129	1.158	0.102
Specs 1	10	-1.077	0.136	1.085	-0.0630	1.214	1.216	0.108
Specs 2	8	-1.114	0.102	1.119	-0.0978	1.322	1.326	0.102
Specs 3	6	-1.053	0.173	1.067	0.0185	1.005	1.005	0.123
Ensemble Average		-1.078	0.135	1.088	0.1149	1.175	1.182	0.108

Table 4.4: Mesh statistics from the three simulations and ensemble average.

The results retrieved from some studies of the literature presented in the second chapter are detailed in the table 4.5. The result obtained for each simulation and a recall of the Reynolds numbers used are presented along with an ensemble average of this set of data.

In a rapid observation, the three simulations seem in good concordance with the literature for the drag coefficient and Strouhal number. In the BARC study [8], similar results were observed for those two statistics in most of the studies. The

Author	Re_H	$t-avg(C_D)$	$t-avg(C_L)$	$t-std(C_L)$	St_H
Shimada and Ishihara [2002] [38]	2.2 $\times 10^4$	0.975	-	0.03 - 0.12	0.103 - 0.119
Arslan et al. [2011] [3]	2.64 $\times 10^4$	0.984 - 1.39	-	0.59 - 0.84	0.07 - 0.16
Mannini et al. [2011] [20]	10^5	0.968 - 1.071	0.0032 - 0.047	0.42 - 1.075	0.094 - 0.102
Mannini et al. [2010] [19]	2.64 $\times 10^4$	1.015 - 1.172	-	1.08 - 1.12	0.087 - 0.105
Mannini and Schewe [2011] [21]	2.64 $\times 10^4$	0.965 - 1.016	-0.087 - 0.085	0.173 - 0.553	0.087 - 0.119
Riberio [2011] [33]	2.64 $\times 10^4$	1.17	-	0.9	0.073
Grozecu et al. [2011a] [**?**]	2 $\times 10^4$	0.96	0.0022	0.35	0.122
Grozecu et al. [2011b] []	4 $\times 10^4$	0.97 - 0.98	-0.097 - 0.0043	0.52 - 0.65	0.107 - 0.11
Bruno et al. [2011] [6]	4 $\times 10^4$	0.96 - 1.03	-0.315 - -0.0024	0.2 - 0.73	0.112 - 0.122
Bruno et al. [2010] [7]	4 $\times 10^4$	1.03	-	0.73	0.112
Wei and Kareem [2011] [44]	10^5	1.165 - 1.305	-0.33 - 0.42	0.495 - 1.465	-
Dahl [2014] [10]	2 $\times 10^5$	1.1008	0.2760	-	0.1221
Ensemble Average		1.065	0.0005	0.634	0.107

Table 4.5: Time statistics and ensemble averages from the literature simulations.

results of the present study matching with those of the literature is thus a good point, which helps defending the reliability of the simulations.

For the lift coefficients, however, the values are not ideal. The ensemble average of the literature is close to zero while for the simulations it is still far from it. The results are not dramatic and the mean values of the lift coefficient were slowly converging towards zero as depicted in figure 4.3. This trend is also underlined in the table 4.3, with the drastic upgrade in the lift coefficient, especially for the third specification which almost reaches the threshold value. As already mentioned before, the value of zero is not reached yet probably due to the lack of statistical accumulation.

The source of this discrepancy could also lies elsewhere. This critical value of lift coefficient, implies a symmetrical mean flow on the upper and lower surfaces of the cylinder. Although the symmetry of the flow in this configuration studied is expected, many results in the literature did not obtain symmetrical flows. And this was not only observed in numerical simulation, but also in experimental ones, the reason are however mostly from different sources.

Another point of interest is the standard deviation of the lift coefficient. In all cases this deviation is significant. Surprisingly though, the three meshes seems to be influenced in the same way, as no major differences between them are observed. It is expected when looking at the time histories, but surprising for the third mesh, given the lower PSD of the Strouhal number frequency. When compared to most results of the literature, these numbers are significantly higher compare to the ensemble average. However, looking at the simulations in details, some of them present also

the same standard deviation. A significant difference between this master thesis simulations and the ones depicted in the literature is the Reynolds number. This could advance some sources of explanation, but no conclusive data are available to explain this phenomenon, and the dispersion in the BARC is already significant despite similar Reynolds numbers.

A general take from these analysis and comparison with the literature is that all three mesh specifications gives precise and concordant results. The third mesh is more precise and it shows in the results. However, the accumulation period for the third mesh remain small and this might have an unnoticed effect on the results. For the three meshes a longer period of accumulation could be of great interest. However, in regards with the computational capacities required for a convective time to be modeled, accumulating more would be a costly process.

4.2 Mean flow analysis

The monitoring of the instantaneous parameters of the flow was performed and analysed. Some interesting results were observed. A comparison with other results obtained from the mean of the flow variables could further improve the understanding of the previous observations.

From Argo DGFluid, some of the variables of the flow mean values are directly accumulated and computed by the solver. The mean values in time and in span of the vorticity and velocity in the entire domain are obtained. On the cylinder's faces, the time accumulation of the pressure or the shear stress are also computed.

With these data, the mean flow features can be mapped and compared. The mean point of reattachment, the size of the recirculation region and it's center are computed bellow. The pressure distribution on both the upper and lower faces of the cylinder are plotted and the results are compared with the literature.

4.2.1 Surfaces mapping

The mean flow over the upper and lower cylinder are obtained. From the literature, the characteristics of this mean flow are known. The shear layer detaches at the leading edges and reattaches before the trailing edges, resulting in a recirculation zone. Several points describing this recirculation region are interesting to capture: the coordinates of its center, its height, and the point of reattachment to the cylinder's faces.

With these data, the comparison within the simulations and with the literature is easier. In the studies from the literature, a lot of dispersion was observed, the mean flow conditions seems thus to be highly dependant on the set-up parameters. Adding this study to the values present in the literature might help discover some feature for the not well known Reynolds number of 2 $\times 10^5$.

Bubble center coordinates

The first values of interest are the coordinates of the center of the bubble. A method in three steps was performed to determined these coordinates from the mean velocity of the flow. Initially, to obtain a clear visual understanding of the mean flow feature, the streamlines are plotted above and bellow the cylinder as depicted in figure 4.6. An approximate location can be deduced from these pictures, which is at the center of these streamlines. The center seems therefore in all simulations to be above the second halves of the cylinder's faces.

From the pictures, the center of the coordinates could be obtained, by adding more precise streamlines in the center of the previous ones. Although it works at perfection, it is an arduous task to perform. An easiest way, is to recall that the velocity magnitude at the center of the mean recirculation zone is null. On the figure 4.7 the velocity contour are illustrated for velocity magnitudes bellow 0.5 [m/s].

Multiple zones of low velocity are depicted on the pictures, however, from the first step with the streamlines, it was determined that the center is in the second halve of the surface. The position of these contours are extracted and with a simple python code, the region of interest can be isolated. With these positions, the center of these regions is easily determined and correspond to the coordinates of the center of the recirculation zones.

This process was repeated for the three specifications and the results obtained for the coordinates of the mean bubble on the upper and lower surfaces are presented in the table 4.6. To ensure the reliability of the results computed, the velocity magnitude is plotted over the y dimension at abscissa of the center, x_c. On these plots depicted in figure 4.8, the velocity comes almost exactly at zero at y_c, meaning the results obtained were pretty close to the actual center of the recirculation region.

Specifications 1

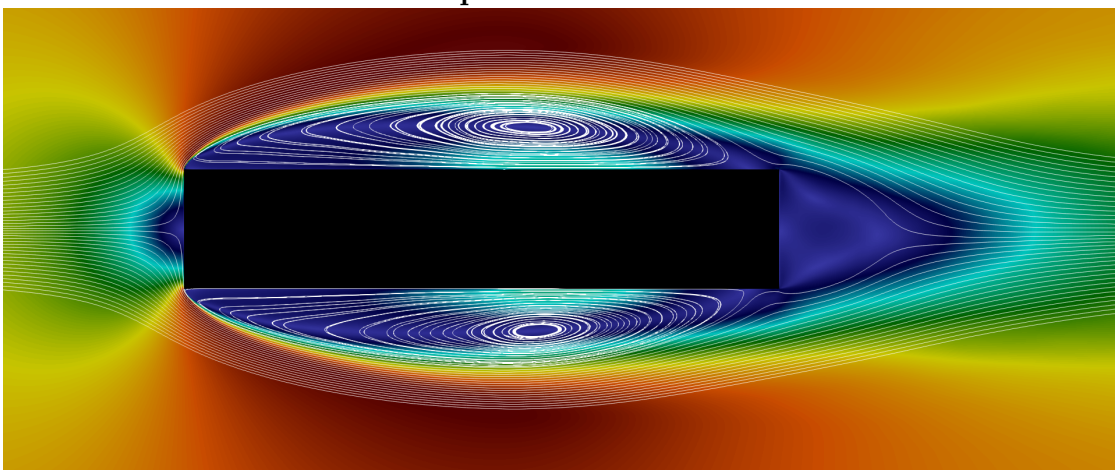

Specifications 2

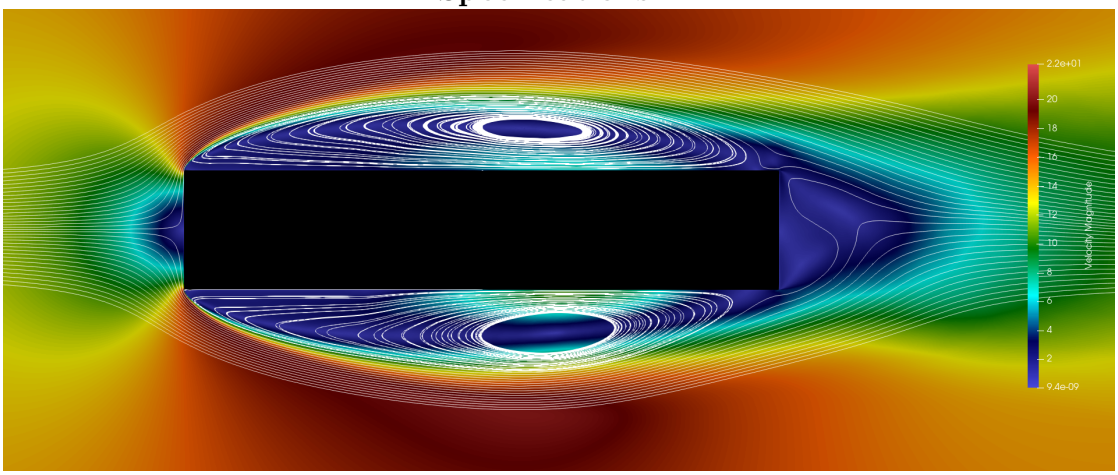

Specifications 3

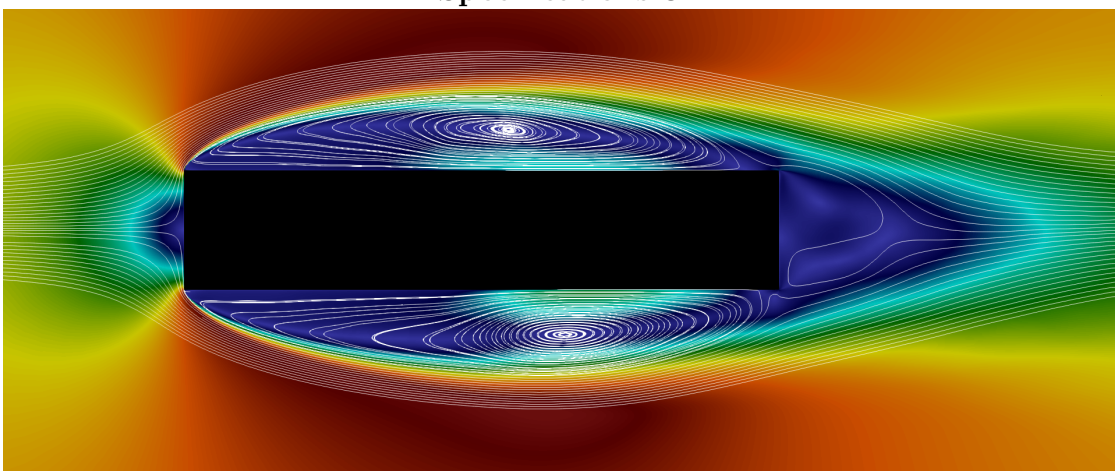

Figure 4.6: Mean streamlines for the three meshes specifications.

Specifications 1

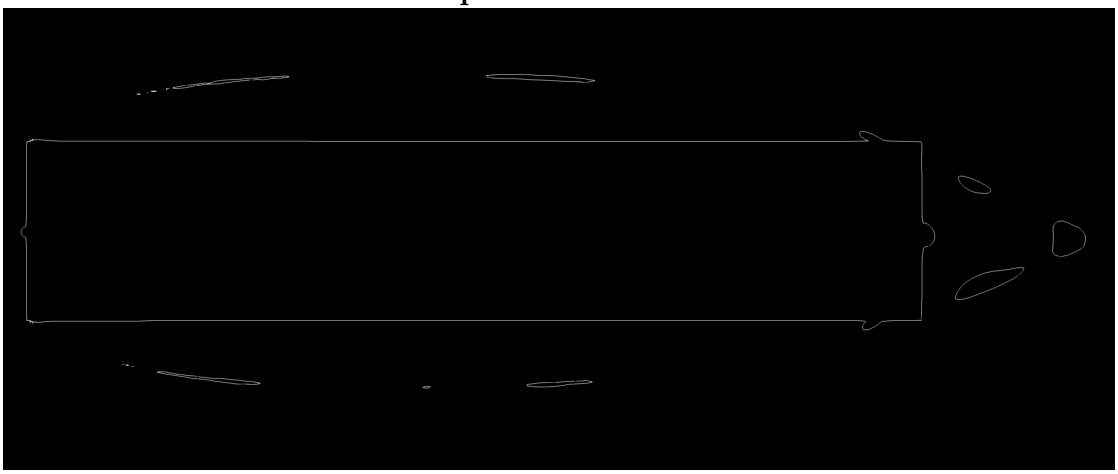

Specifications 2

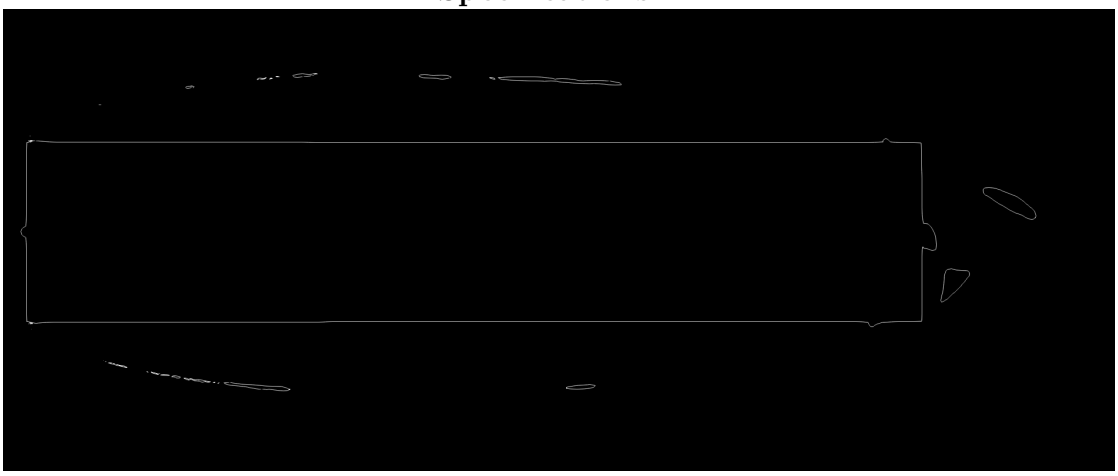

Specifications 3

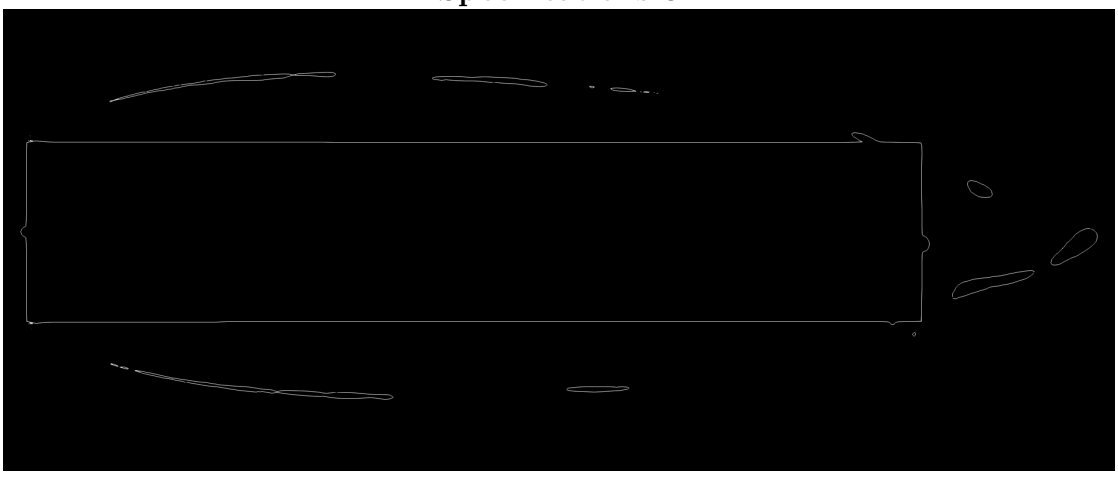

Figure 4.7: Velocity contours from velocity magnitudes bellow 0.5 [m/s] for the three specifications.

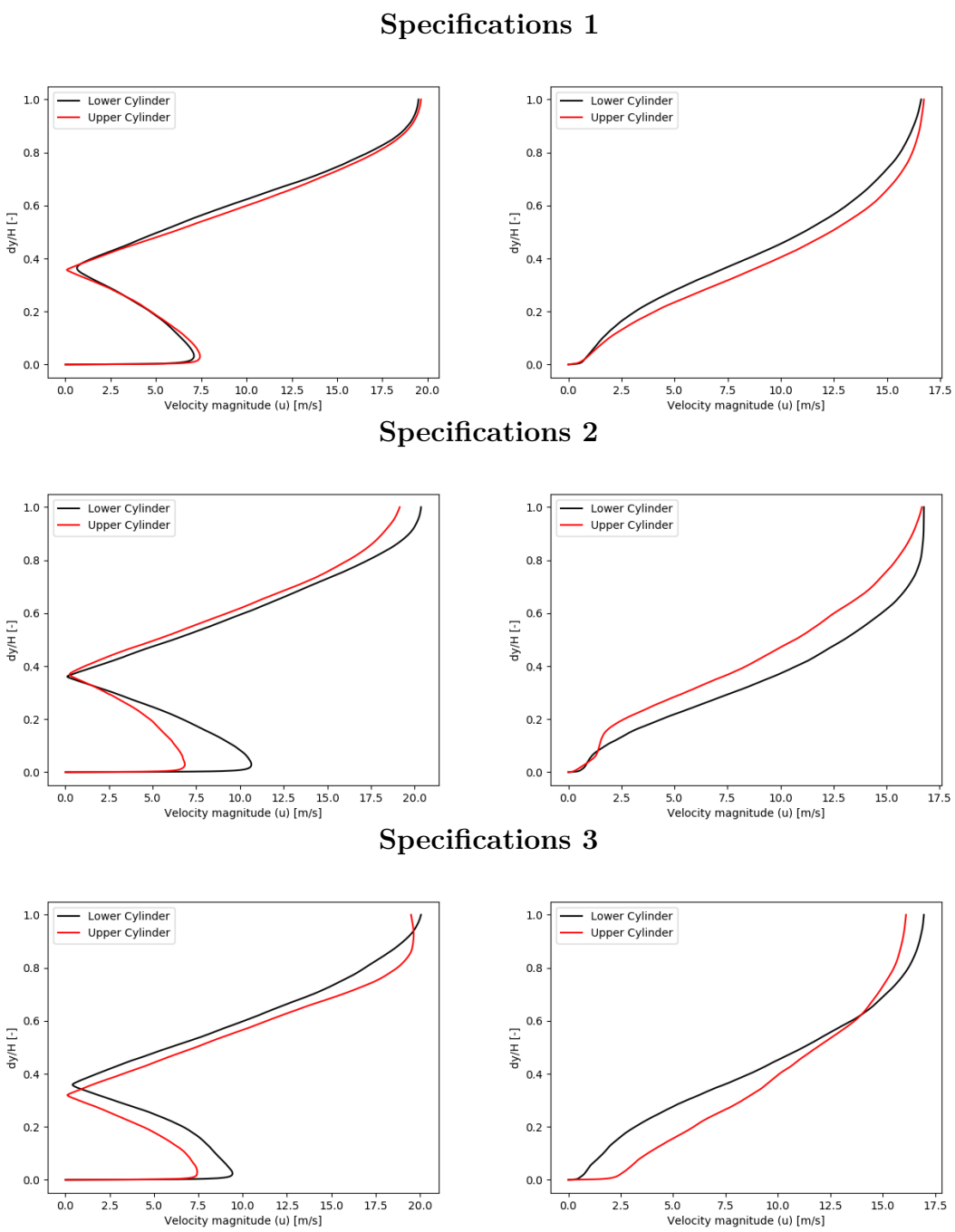

Figure 4.8: Plot of the velocity magnitude along the y-direction at the center of the recirculation region abscissa x_c (left) and at the point of reattachment x_R (right).

Height

To compute the height of the recirculation zone, the streamlines following the mean flow detached shear layer on both faces are plotted. These streamlines are obtained when it passes the closest to the front edges of the cylinder. They are illustrated for all three simulations in the figure 4.10, along the vorticity contours computed earlier.

The height of the recirculation region is computed by extracting the position of the plotted streamlines. For the upper cylinder, the maximal position in y, while the minimum for the lower cylinder. The values for the upper and lower surfaces recirculation zone height (h_b/H) are also presented in the table 4.6.

Length, reattachment point

To compute the point of reattachment of the shear layer, a first qualitative observation can be performed. Looking at the figure 4.10, where the shear layer streamlines and the vorticity contours are illustrated, two points can be made. Near the end of the cylinder's face, the streamline comes almost touching the surface, and is parallel to it. In this region, the mean flow is reattached since this implies that the shear layer is parallel to the cylinder and close to it.

An other observation is some small region near the surface of the cylinder where the velocity magnitude is null. They are depicted by little ears near the end of the cylinder's surfaces in figure 4.10. The point of reattachment is also defined with a zero velocity magnitude above the surface of the cylinder.

However, figuring the exact point using these pictures is not really accurate. The best way to obtain the length of the recirculation zone is to plot the time-average shear stress distribution along the cylinder's faces. For the three specifications, the shear stresses distribution are plotted in figure 4.9 for both the upper and lower surfaces. The location of the reattachment point is the abscissa where the mean shear stress changes in sign.

In the region of the main vortex, the flow at the surface goes in the opposite direction compare to the freestream. For this section, the mean friction coefficient is negative, ($\overline{C_f} < 0$). Then further down, the reattached flow goes in the same direction as the freestream velocity and the shear stress coefficient is positive ($\overline{C_f} > 0$). The point of reattachment can thus be computed from the shear stress coefficient. The values for the three simulation are presented in the table 4.6.

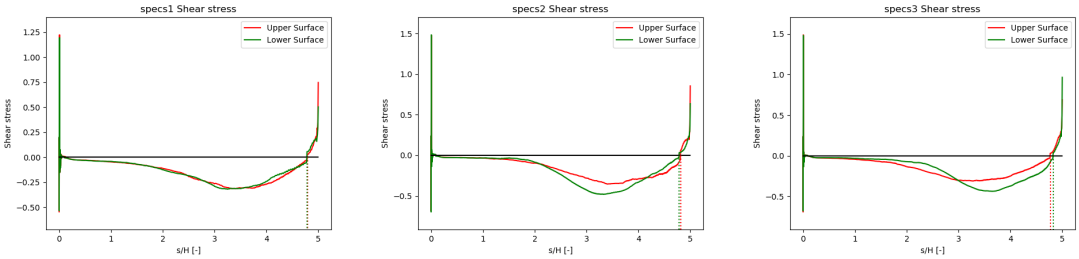

Figure 4.9: Shear stress distributions over the surfaces for the three simulations.

The velocity magnitude at the point of reattachment for each simulation are also plotted in the figure 4.8. The points of reattachment are definitely well found when looking at these graphs. The velocities are not always the same, but the curves go straight to the freestream velocity. And they indeed look like a velocity profile found for turbulent flow attached to a no-slip wall.

Comparison

All the data computed here above for the three meshes are assembled in the table below 4.6. The values are made dimensionless using the height of the cylinder (H), to facilitate the comparison with other studies.

Simulation	Face	x_R/H	h_b/H	x_c/H	y_c/H
Specs 1	Upper	4.790	0.664	2.872	0.353
	Lower	4.784	0.671	2.707	0.355
	Mean	4.787	0.667	2.783	0.354
Specs 2	Upper	4.813	0.682	2.990	0.367
	Lower	4.786	0.716	3.034	0.318
	Mean	4.800	0.699	3.012	0.343
Specs 3	Upper	4.526	0.619	2.569	0.318
	Lower	4.769	0.705	3.059	0.360
	Mean	4.648	0.662	2.809	0.339
Ensemble average		4.745	0.676	2.868	0.345

Table 4.6: Recirculation bubble data for the three meshes, and for the upper and lower cylinder's faces.

The differences between the three meshes are pretty small. The point of reattachment of the flow is in all six cases close to the trailing edge. The height or the center's ordinate of the bubble have also similar values in all simulations. The only variable that deviates across the simulations is the abscissa of the bubble.

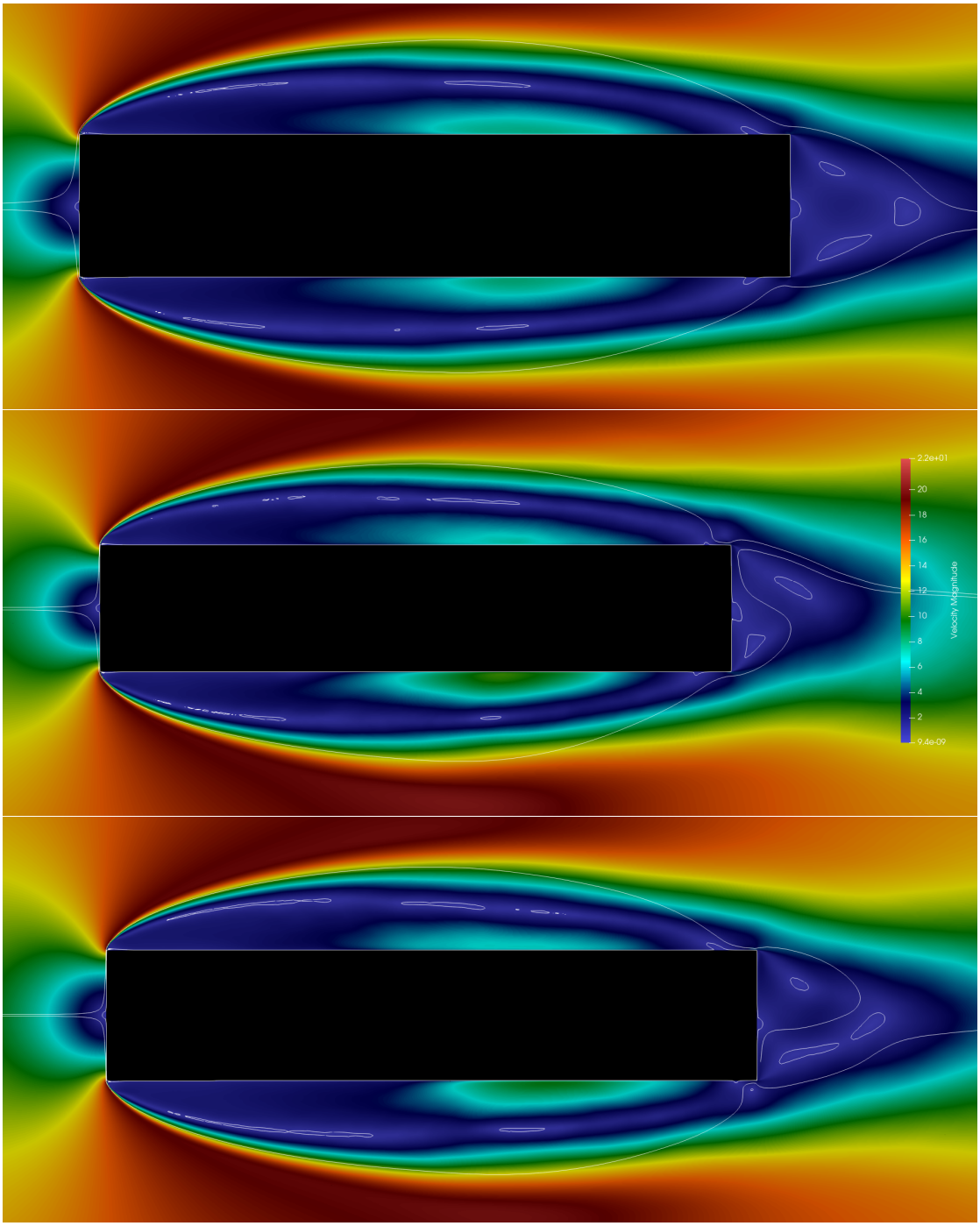

Figure 4.10: Mean flow around the cylinder, with shear layer streamlines and velocity contours of velocity magnitudes below 0.5.

And all the other results are pretty similar to one another. The only difference remains in the symmetry, for the first specification the variability between the upper and lower surface is close to zero. Even more when compare to the other two simulations, which see bigger dispersion. The only value that varies slightly is the abscissa of the center of the recirculation zone (x_c). But even for this value, the variation observed for the third simulation is higher by several folds.

In the table below 4.7, the statistics obtained in the literature are presented. The Reynolds number of each of these studies is also recalled for the sake of clarification. The values presented in some studies were computed with the origin at the center of the cylinder upper surface. To compare the results of the present study with those of the literature, the result were adapt to the system used in this thesis.

Study	Re_H	x_R	x_c	y_c
Arslan et al. [2011] [3]	2.64 $\times 10^4$	1.84 - 4.79	1.25 - 3.25	0.28 - 0.32
Mannini et al. [2010] [20]	2.64 $\times 10^4$	4.22 - 4.56	1.06 - 2.45	0.27 - 0.38
Mannini et al. [2011] [21]	10^5	4.75	1.5 - 3	-
Grozescu et al. [2011] [13]	2 $\times 10^4$	4.14 - 4.6	2.41 - 3.47	0.26 - 0.305
Grozescu et al. [2011] [12]	4 $\times 10^4$	4.15	2.33	0.32
Bruno et al [2010] [7]	4 $\times 10^4$	4.68	2.54	0.3
Ensemble Average		4.75	2.27	0.304

Table 4.7: Statistics of reattachment and center of recirculation bubble from literature results.

On average, the results computed in this study have some similitude to the literature results. The reattachment point in most of the simulations where situated close to the trailing edges. The same goes for the center of the recirculation bubbles. The ordinate is pretty close while the abscissa of this study is placed further down the cylinder but not too far off. Generally, despite the huge variety in the results and the Reynolds difference between the several studies, this study is pretty spot on, with the ensemble average. The point of reattachment are pretty much exactly the same. Again, the primary dispersion arise for the abscissa of the center of the recirculation zone. However, this point is also vastly dispersed in the results of the literature.

4.2.2 Pressure distribution

For the three simulations, the mean pressure on the surface of the cylinder are mapped. To analyse this data set and compare it to previous results, the first task is to make it dimensionless. The coefficient of pressure is computed in the same

way as the forces coefficients earlier, but only using the flow characteristics. The reference used here are the freestream velocity (U_∞) and the pressure (p_{ref}) and density of the flow (ρ):

$$C_p = \frac{p - p_{ref}}{\frac{1}{2}\rho U_\infty^2} \tag{4.11}$$

The time-averaged pressure coefficients are plotted in the figure 4.11, for the upper and lower faces of each simulation. The plots show the distribution of pressure along the x direction for each span point, as well as the spanwise average in black.

The graphs illustrate the deviations of the pressure distributions for different point in the span. In the case of a totally converged flow, these distribution should all follow the same curve, the mean curve. In some case, this phenomenon is almost observed, especially for the upper cylinder face from the first simulation. And in all cases the distributions are all closely following the mean distribution. This shows that the pressure over each surfaces are somewhat converged with the cumulative periods.

If the difference on the same surfaces are swallow, the mean of the three simulation distributions are plotted in the figure 4.12. In this plot, the averages from the upper and lower surfaces for each simulations are illustrated. In the first half of the cylinder, up to s/H = 2, the three meshes pressure distributions are close to each others. The main difference is observe right after with the second specifications deviating from the other two. In general, the distributions of the pressure coefficients for the three simulations have similar shapes.

These coefficients distribution are compared with those obtained in the literature. Various results were obtain for the pressure distribution in the x direction. An overall good agreement for all numerical simulation on the first halve distribution was obtain. For this part, the simulations performed in this thesis all reaches similar values.

However, further down, the mean shape of the distribution obtain from previous results is vastly different. The pressure coefficient immediately goes up and reaches the value of -0.2 near the trailing edge. This value is also obtained here, but after a slight dive around the center of the cylinder's face, followed by a sharper raise. Although some of the simulation obtained the same shape, most of them did not.

A last interesting point to note is the lack of amelioration with the meshes resolution. No precise conclusion can be drawn out of this graphs on the impact of the resolution on the pressure coefficient distribution.

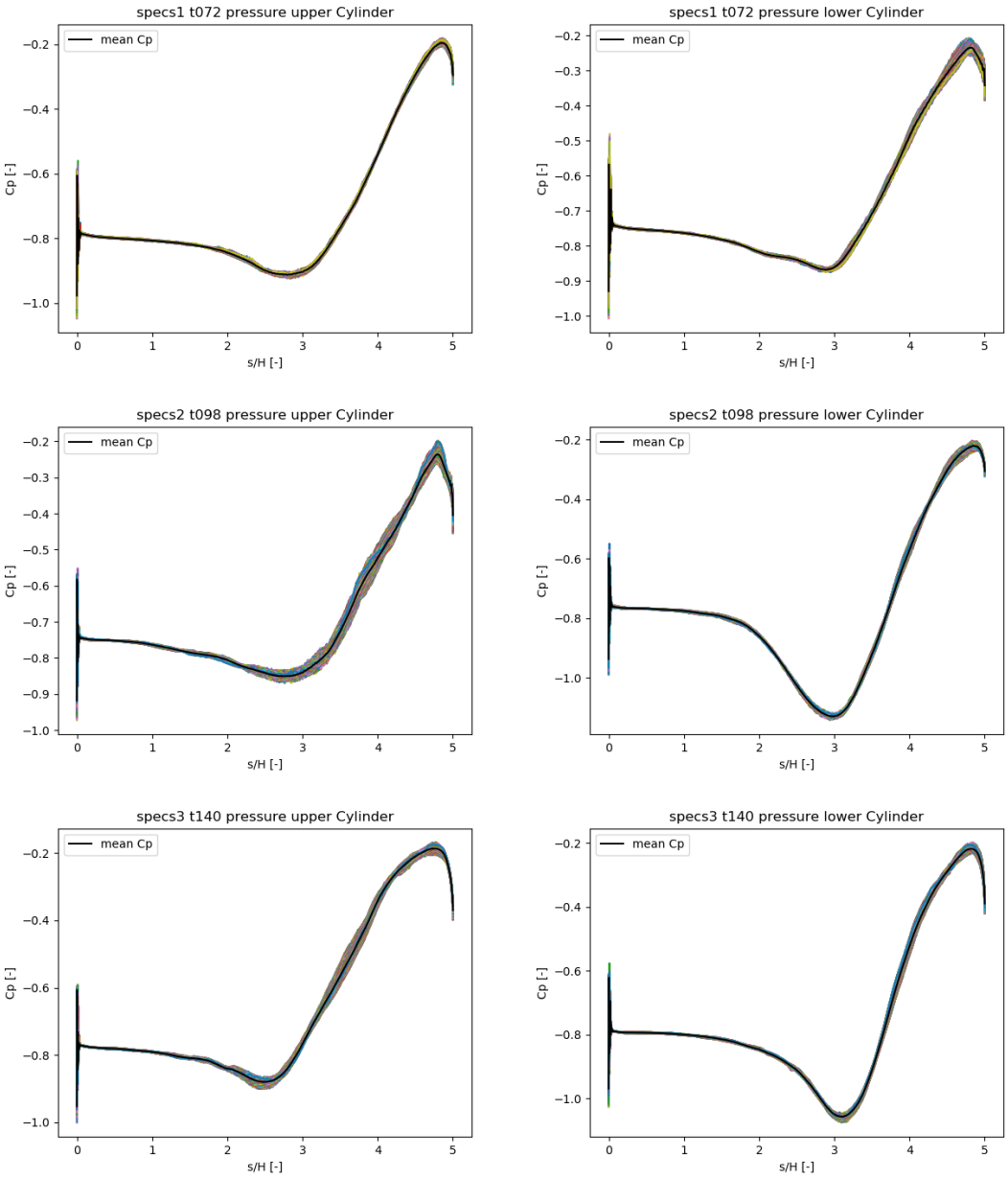

Figure 4.11: Distribution along the x direction of the pressure coefficient for the upper (left) and lower (right) surface, for the first (top), second (middle) and third (bottom) specifications.

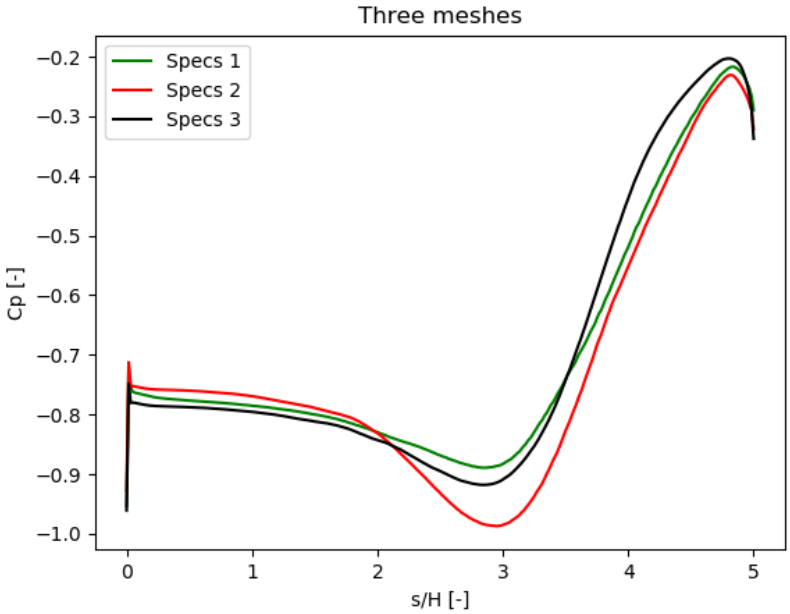

Figure 4.12: Mean coefficient of pressure distribution for the three meshes. The coefficients are averaged in time, span and over the upper and lower surfaces.

4.2.3 Mean flow convergence

A first study of the time convergence was performed based on the monitors, a similar study can be conducted to assess for the convergence of the mean flow. The convergence was already observed from the pressure coefficient distribution, by analysing the dispersion from the results at different span points in figure 4.11. None are fully converged, however, the upper cylinder distribution from the first simulation seems more converged in term of pressure distribution compared to the others.

Another trend to observe is the of the mean streamlines around the rectangular cylinder. For each simulation, this convergence is depicted across multiple pictures of the mean flow at different times. They are shown in Annex A (A.1,A.2,A.3). For each of the simulations, the convergence of the mean flow toward an equilibrium is observed. The trends between the pictures are still noticeable, which would imply that the mean flow has yet to reach a converged state.

4.3 Spanwise correlation

When the domain was defined, the span length was set to one height of the cylinder. This choice was made to alleviate the computational costs already significant of the simulations. The focus was put on the grid spacing of the mesh in the spanwise dimension as it was a key value determined by Bruno et al. in 2012 [6] and Mariotti et al. in 2017 [23].

The three meshes conducted in this master thesis used two distinct mesh discretization for the span. A coarser on for the first specifications and a more refined for the other two which values are presented in the table 3.1.

The small spanwise length will lead to greater correlation than in other studies, the objective of this section is to observe if the fine grid spacing applied will help alleviate this. To observe this factor, several sets of probes were placed in the simulation domain. The placement of the probes are pictured in figure 4.13, with three distinct groups of probes. Surface probes, in red capture the pressure correlations at the surfaces of the cylinder. The boundary layer probes in green capture the velocity correlations in the detached boundary layer, near the leading edge. In the wake, the probes in blue gather the pressure and velocity correlations.

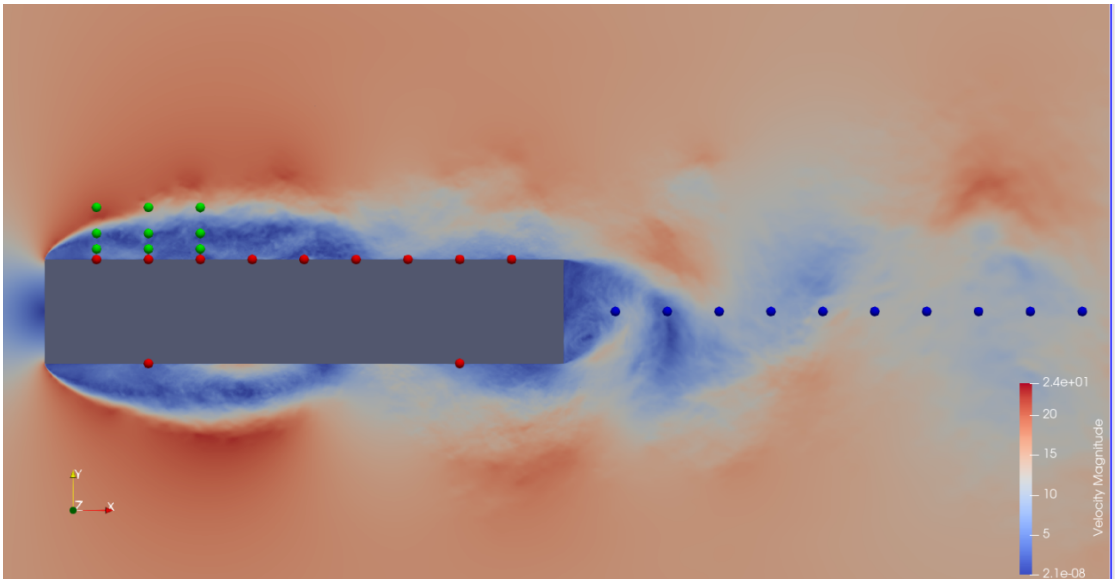

Figure 4.13: Probes configuration

The results obtain for the spanwise correlation are depicted in the Annex B (B.2,

B.1, B.3). The pressure correlation at the surface of the cylinder for the third specification are depicted bellow 4.14. The correlations of pressure from the BARC are depicted in the figure bellow 4.15.

The pressure correlation reveals to be really correlated. In comparison with the BARC benchmark, only the probe 4 at the cylinder surface reveals somewhat low correlations. All the others, from all simulations are ultra correlated in pressure. In the wake of the cylinder it is even worse. These result are surprising since the BARC showed better correlations at the same spanwise length for a coarser grid spacing in the spanwise dimension.

A reassuring point comes from the velocity correlations, both in x and z direction gives way better results. However, no amelioration is observed when the mesh is further refined in the simulation two and three compared to the correlations of the first specifications. Here again a surprising results when compared to the study of Bruno et al. [6] and Mariotti et al. [23] who observed less correlation on more refined grids.

4.4 Symmetry analysis

The rectangular cylinder and the freestream conditions are symmetric with no incidence angle. A symmetry would therefore be expected for the mean flow characteristics, such as the recirculation bubble and statistics, with the lift coefficient. However, in the literature, few of the studies reached perfect symmetry in even one of these characteristics. The ensemble averages on the other hand, does reach such convergence value as shown for the lift coefficient in the table 4.5. In this thesis, the symmetry of the flow from the three simulations was studied from various perspectives.

It is important to note that the instantaneous flow is not symmetric at all, the complex flow and interactions prevent it. However, the mean flow and time-averaged statistics, should converge towards a clear symmetry.

From the force analysis, a time-averaged lift coefficient of zero would represent a perfectly symmetric flow. The third simulation mean lift coefficient approachs this value, when the initial transient state is ruled out. Although close to zero, the lift coefficient of this simulation does not really speak for symmetry. The period of accumulation is thin so this value might be the call of luck. However, the three simulations convergence towards this value of zero lift coefficient, the accumulation is simply to swallow to conclude anything.

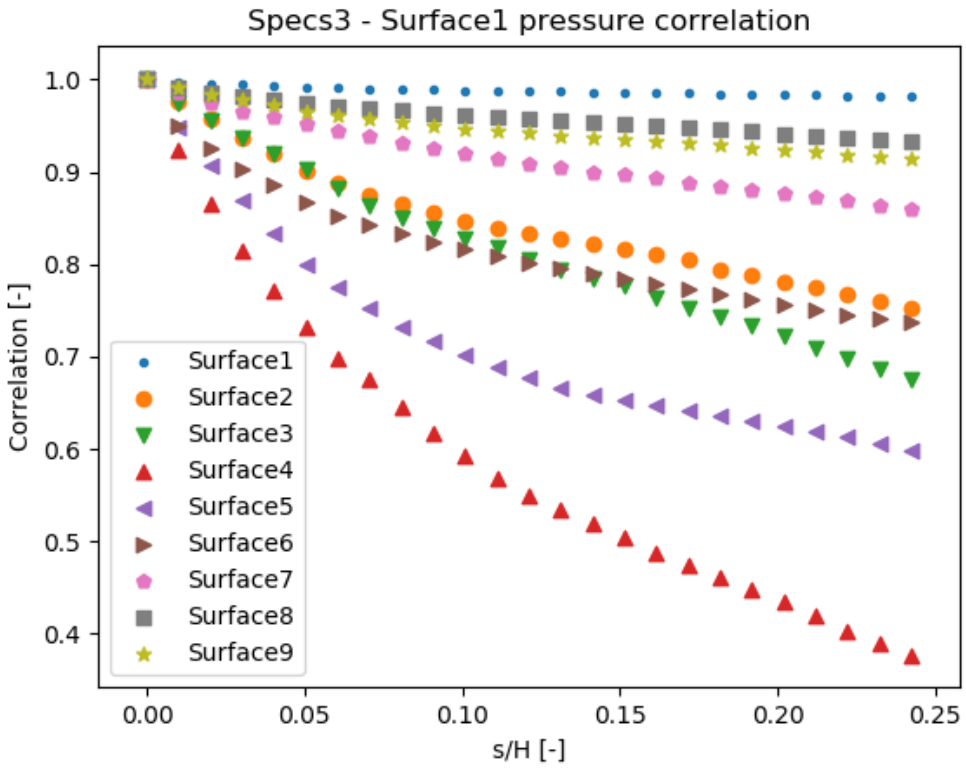

Figure 4.14: Pressure correlation at the cylinder surface for the third specifications

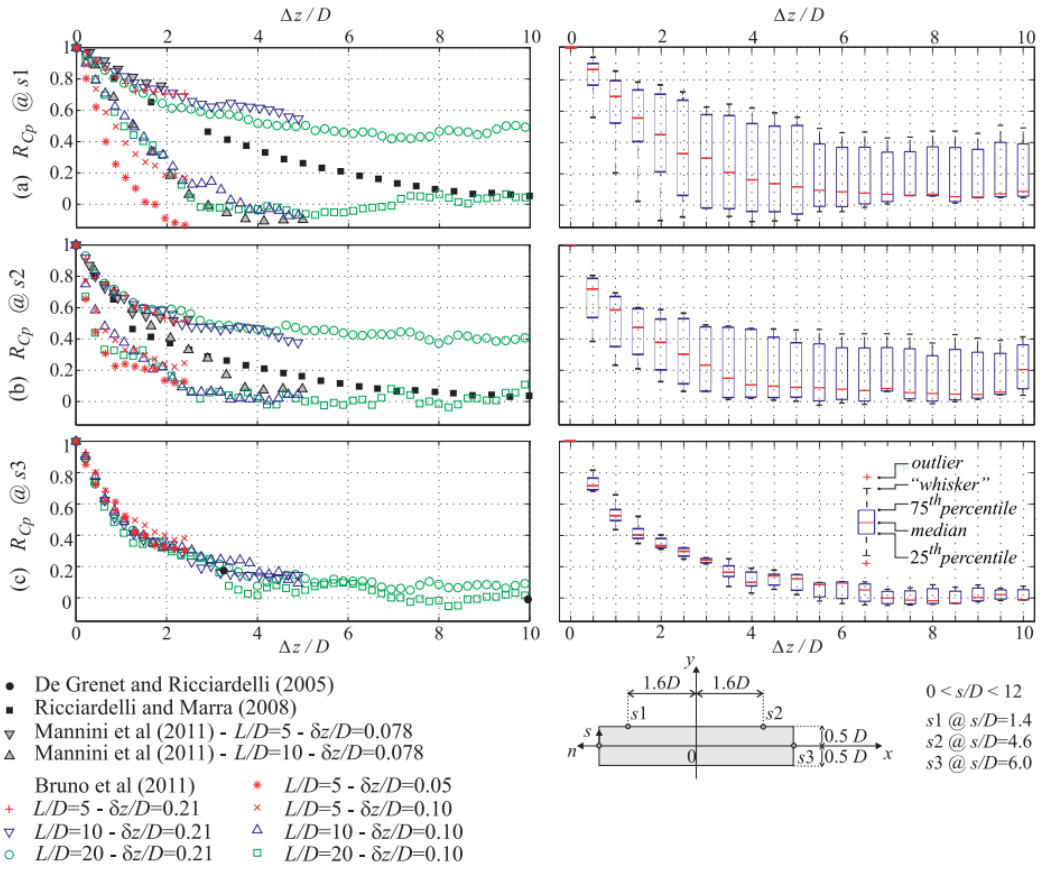

Figure 4.15: Correlation of pressure form the BARC at different points. From Bruno et al. [8].

If the lift coefficient can not help much, the mean flow features certainly do. The symmetry of the mean flow can be observe from the streamlines drawn from the mean velocity field, depicted in figure 4.6. The observation of those graphs and of the data extracted from them, clearly shows an asymmetry of the flow. However, the convergence of the mean flows does seems to flow towards a symmetry as it can be observed in the figure of Annex A. The dispersion in the symmetry for the third specification is still quite large but this still probably due to the lack of cummulated statistics.

Chapter 5

Conclusion

In this master thesis, numerical simulations were performed on the flow around a rectangular cylinder with aspect ratio of 5. The results obtained from these simulations were thoroughly analysed and compared with the literature. A mesh convergence study was also performed to asses the impact of the resolution of the mesh.

The results obtain from the three simulations were in good agreement with the literature. However, the results obtained and their dispersion when different period are observed showed the importance of the period of accumulation. The mesh convergence study revealed the significant impact of the shear layer resolution compared to the near wall resolution.

The analysis of the mean flow features did not diverge from previous results obtained in the literature. The reattachment of the shear layer tends to the end of the surface of the cylinder as depicted in many studies. The characteristics of the flow showed many similarities with the literature and the impact of the mesh resolution was deemed irrelevant.

The mean pressure distribution however diverged slightly from other results in the region under the center of the recirculation zone. Similar results were obtained for all three meshes specifications, showing an intriguing feature that was only found in one or two results of the literature. For the rest of the distribution, the features were mostly similar to all other simulations.

The spanwise correlation was studied and the result were not ideal. The amelioration of the grid spacing in the span direction showed no major effects on the correlations. The pressure data are strongly correlated on the surface of the cylinder and even more in the wake. The only reassuring results are the velocity correlations that

showed way better results.

A tendency toward a symmetrical flow is also observed in all simulations. This comes in line with the expected mean lift coefficient of zero. Here again, the period of accumulation is the driving factor leading to better and more precise results.

The mesh refinement proved to be an important for the capture of the detached shear-layer. In the less refined meshes, the shear layer is dissipated and its influence is not modelled by the solver. This dissipation did not impact the flow feature who are mainly two-dimensional. But the standard deviation of the lift coefficient was greatly impacted. Without the refinement, this data greatly diverges from the results obtained in previous studies, with a far greater deviation.

Like in all simulations, a dilemma is observed between the cost and the precision of the simulation. But in this case, a double dilemma is observed. The resolution needs to be enough to capture the turbulent detached shear layer with precision. And like in all simulations the flow features needs to converge for the researchers to collect accurate data. But in this case, the convergence is never achieved due to the unsteadiness, and the precision of the solution is proportional to the size of the period of accumulation. So for a good accuracy, a highly refined mesh is needed but also a low computational cost mesh to gather enough data.

Chapter 6

Improvement

The flow around rectangular cylinders remains an interesting subject with many points to uncovers. The lack of simulations performed at high Reynolds numbers of 2×10^5 and the large dispersion in other results makes the validation of the simulation difficult. More results should appear in the next few years thanks to the benchmark launched by the CSTB. Statistical analysis of more data sets of exclusively flows at this precise Reynolds number would be a great contribution.

In this study, the results from the pressure correlations are intriguing and would require further in depth investigation. The span is indeed smaller than the recommendations, and if the computational resources are present a larger span would be a huge upgrade.

The thesis simulations were strongly limited by the resources available. The high turbulence flow analysed and the induced complex features need a high mesh resolution. Furthermore, the accumulation of lots of statistics would be an obligation for further study to ensure the reliability of the results. Bigger installations would therefore be required for a future investigation and continuity of this thesis work.

Appendix A

Mean flow convergence

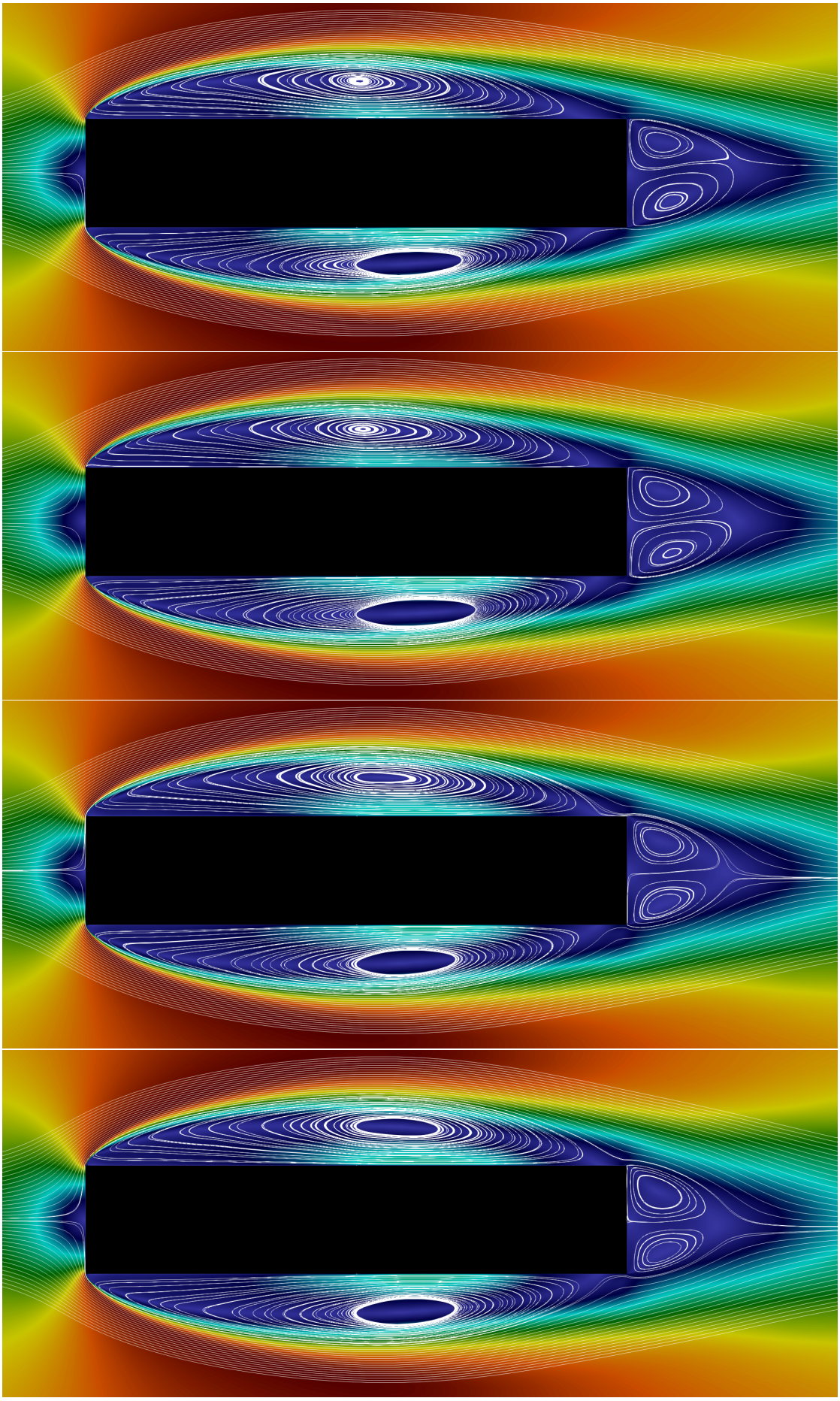

Figure A.1: Mean flow of the first specification at distinct times increasing from top to bottom.

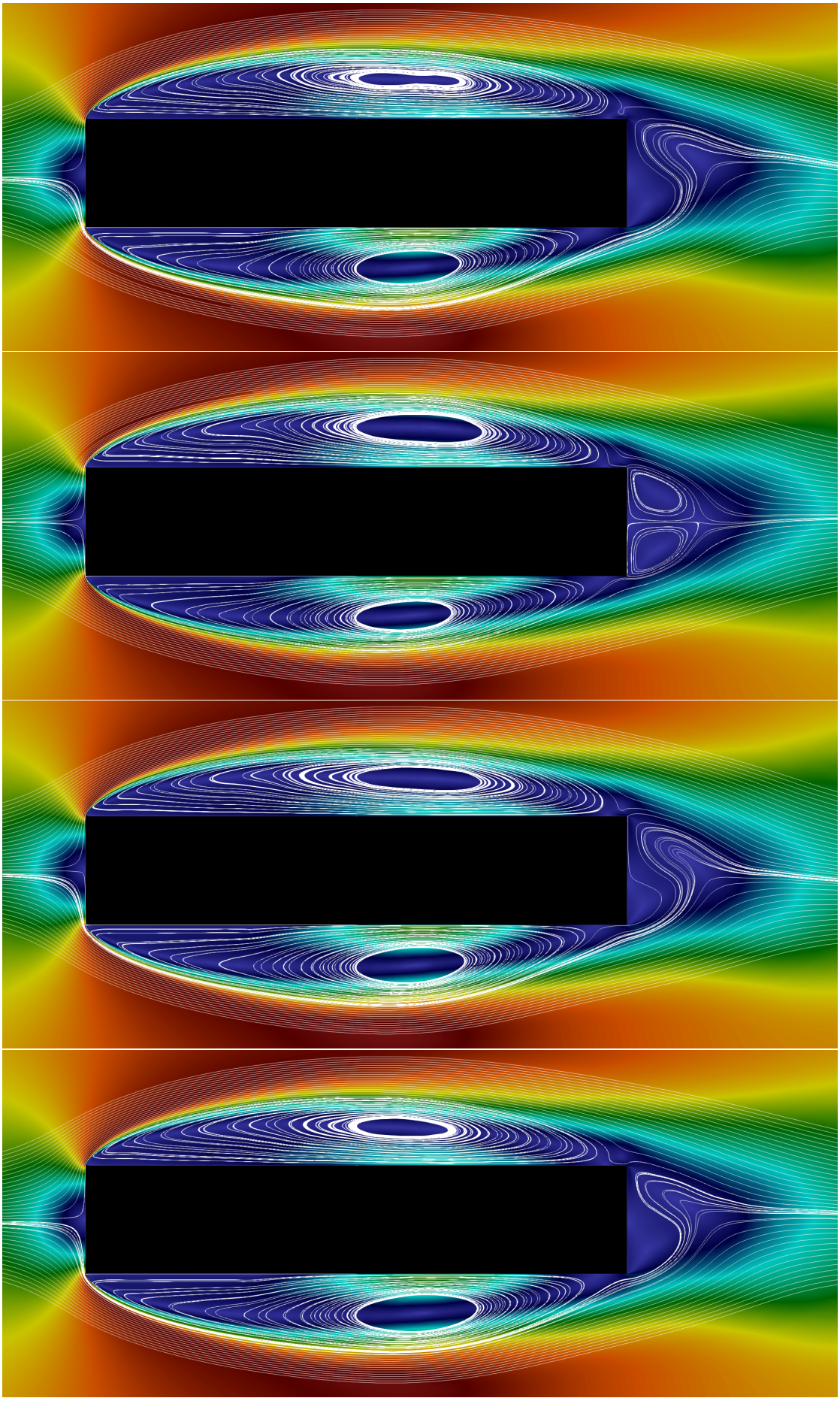

Figure A.2: Mean flow of the second specification at distinct times increasing from top to bottom.

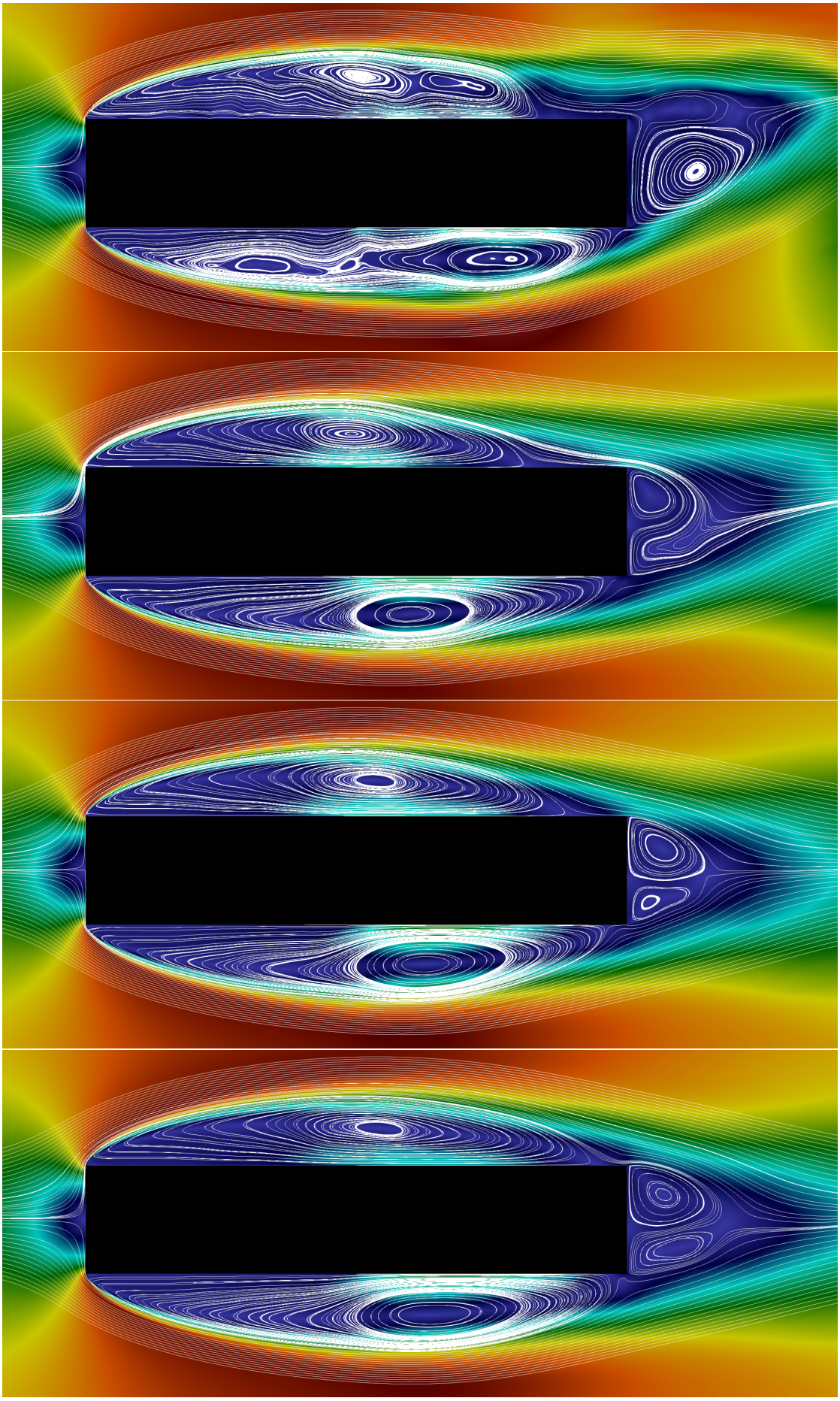

Figure A.3: Mean flow of the third specification at distinct times increasing from top to bottom.

Appendix B

Spanwise correlations

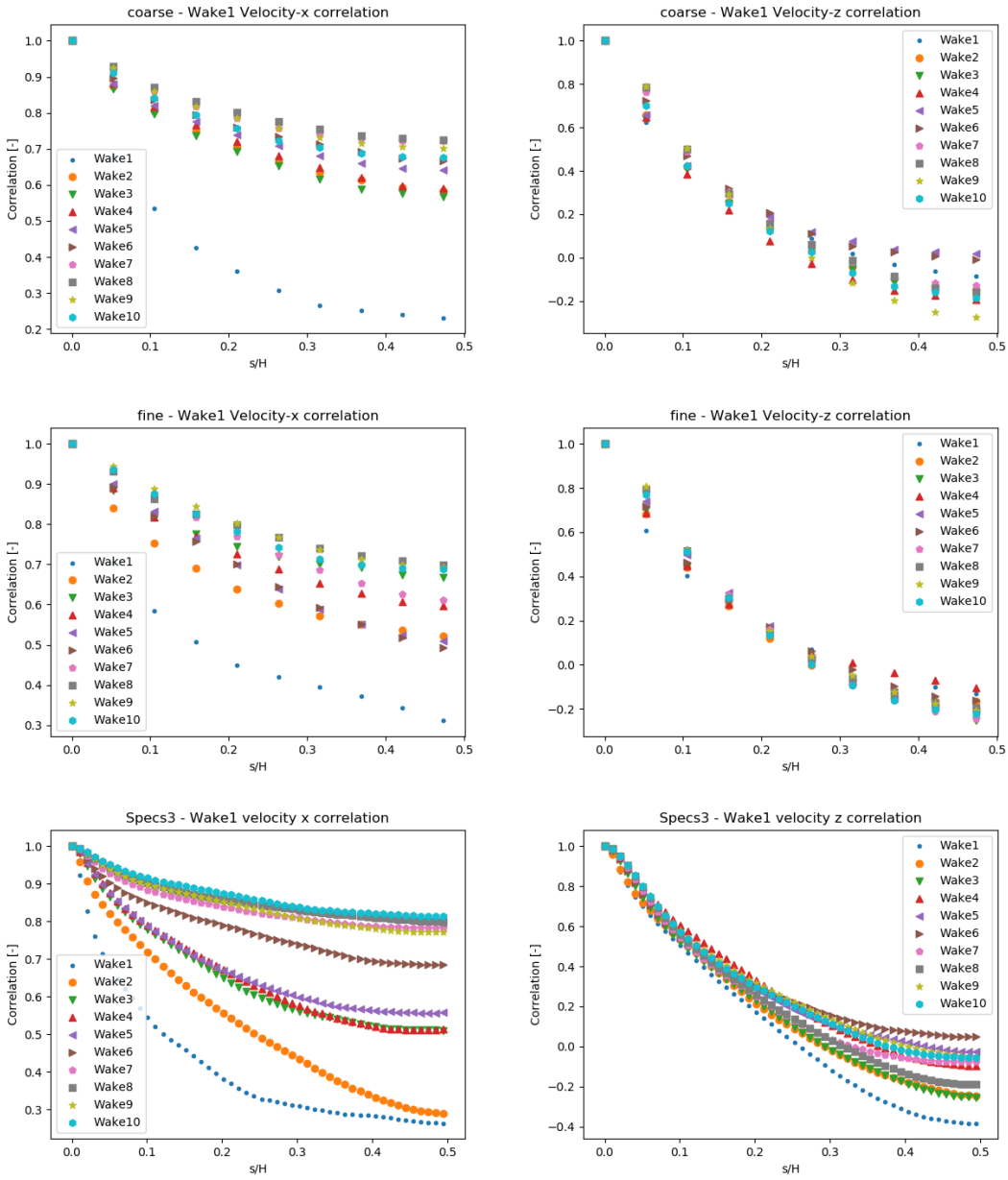

Figure B.1: Velocity correlations in the wake, the x component (left) and the z component (right).

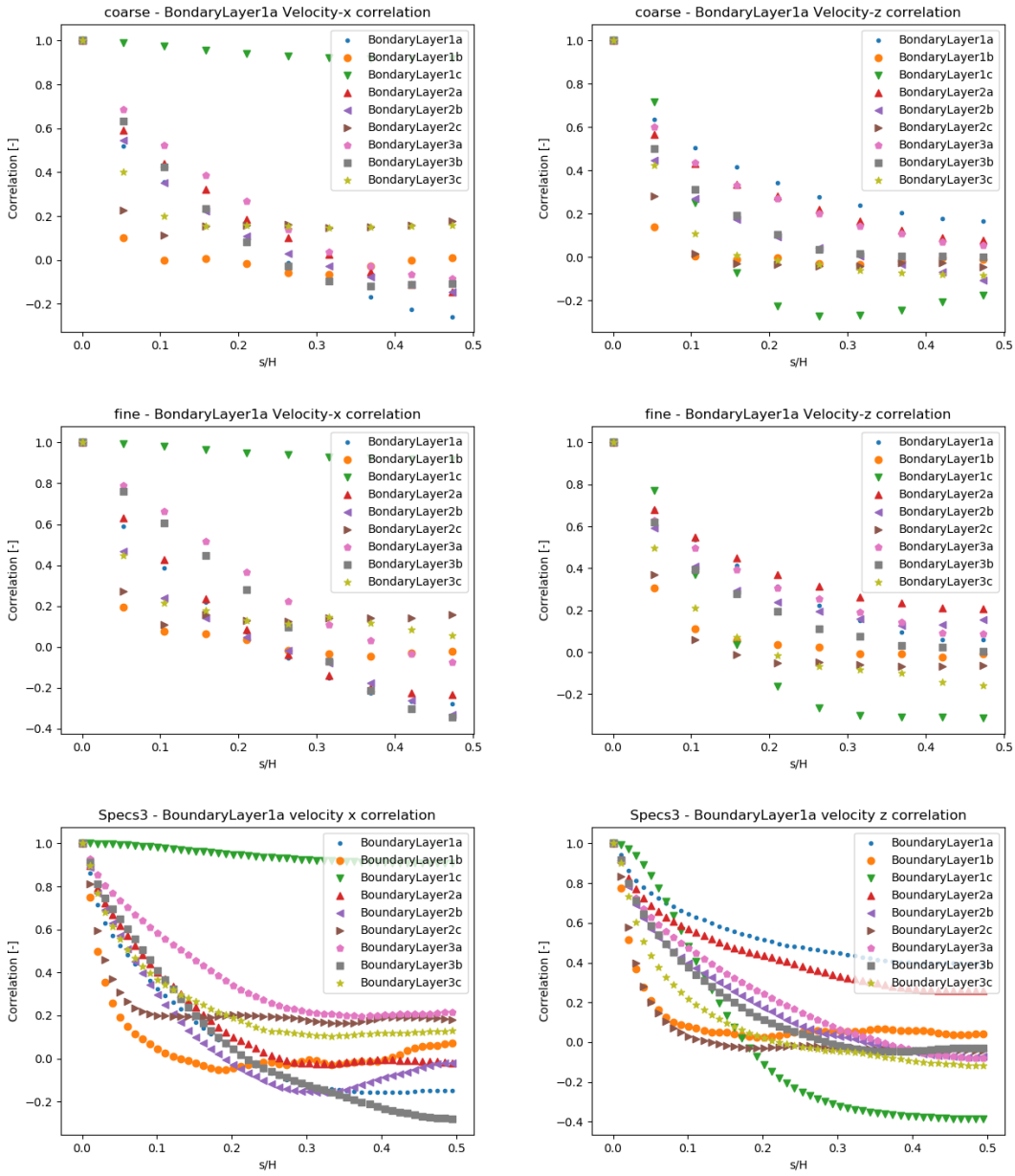

Figure B.2: Velocity correlations in the boundary layer, the x component (left) and the z component (right).

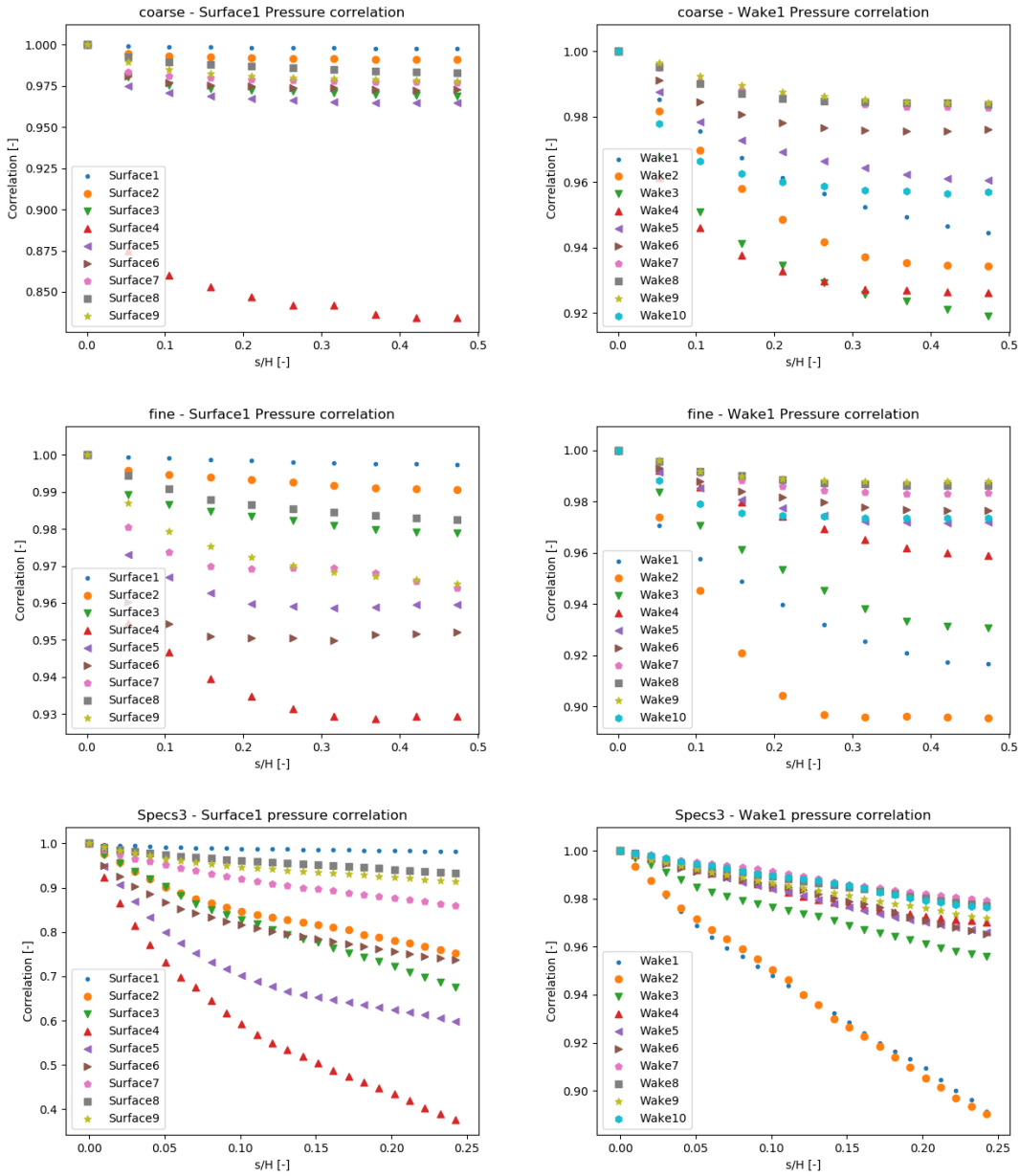

Figure B.3: Pressure correlations at the cylinder upper surface (left) and in the wake (right)

Bibliography

[1] Sarallah Abbasi. Numerical simulation of aspect ratio effect of the rectangular cylinder on the aerodynamic noise. *Journal of Computational & Applied Research in Mechanical Engineering (JCARME)*, 12(2):263–273, 2023.

[2] James Ahrens, Berk Geveci, and Charles Law. *ParaView: An End-User Tool for Large Data Visualization*. Visualization Handbook. Elsevier, 2005.

[3] Tufan Arslan, Bjornar Pettersen, and Helge I Andersson. Calculation of the flow around two interacting ships. In *Proceedings of the thirteenth International Conference on Wind Engineering, Amsterdam, The Netherlands*. CIMNE, 2011.

[4] Peter W Bearman. On vortex shedding from a circular cylinder in the critical reynolds number regime. *Journal of Fluid Mechanics*, 37(3):577–585, 1969.

[5] AJ Bronkhorst, CPW Geurts, and CA Van Bentum. Unsteady pressure measurements on a 5:1 rectangular cylinder. In *Proceedings of the 13th International Conference on Wind Engineering, Amsterdam, The Netherlands*, volume 1015, 2011.

[6] Luca Bruno, Nicolas Coste, and Davide Fransos. Simulated flow around a rectangular 5: 1 cylinder: Spanwise discretisation effects and emerging flow features. *Journal of Wind Engineering and Industrial Aerodynamics*, 104:203–215, 2012.

[7] Luca Bruno, Davide Fransos, Nicolas Coste, and Arianna Bosco. 3d flow around a rectangular cylinder: a computational study. *Journal of Wind Engineering and Industrial Aerodynamics*, 98(6-7):263–276, 2010.

[8] Luca Bruno, Maria Vittoria Salvetti, and Francesco Ricciardelli. Benchmark on the aerodynamics of a rectangular 5:1 cylinder : an overview after the first four years of activity. *Journal of Wind Engineering and Industrial Aerodynamics*, 126:87–106, 2014.

[9] Andrea Cimarelli, Adriano Leonforte, and Diego Angeli. Direct numerical simulation of the flow around a rectangular cylinder at a moderately high reynolds number. *Journal of Wind Engineering and Industrial Aerodynamics*, 174:39–49, 2018.

[10] Sindre Misund Dahl. Unsteady rans simulation of flow around rectangular cylinders with different aspect ratios at high reynolds number. Master's thesis, Institutt for marin teknikk, 2014.

[11] Geuzaine, Christophe and Remacle, Jean-Francois. Gmsh.

[12] AN Grozescu, L Bruno, D Fransos, MARIA VITTORIA Salvetti, et al. Large-eddy simulations of a benchmark on the aerodynamics of a rectangular 5: 1 cylinder. In *Atti del XX Congresso della Società Italiana di Meccanica Teorica e Applicata*, 2011.

[13] Annabella N Grozescu, Maria Vittoria Salvetti, Simone Camarri, and Guido Buresti. Variational multiscale large-eddy simulations of the barc flow configuration. In *Proceedings of the Thirteenth International Conference on Wind Engineering, Amsterdam, The Netherlands*, 2011.

[14] FL Haan Jr and A Kareem. Anatomy of turbulence effects on the aerodynamics of an oscillating prism. *Journal of engineering mechanics*, 135(9):987–999, 2009.

[15] K. HOURIGAN, M.C. THOMPSON, and B.T. TAN. Self-sustained oscillations in flows around long blunt plates. *Journal of Fluids and Structures*, 15(3):387–398, 2001.

[16] Thai-Hoa Le, Masaru Matsumoto, and Hiromichi Shirato. Spanwise coherent structure of wind turbulence and induced pressure on rectangular cylinders. *Wind and Structures An International Journal*, 12, 09 2009.

[17] C. Mannini, A. Mariotti, L. Siconolfi, and M. V. Salvetti. Benchmark on the aerodynamics of a 5:1 rectangular cylinder: Further experimental and les results. In Maria Vittoria Salvetti, Vincenzo Armenio, Jochen Fröhlich, Bernard J. Geurts, and Hans Kuerten, editors, *Direct and Large-Eddy Simulation XI*, pages 427–432, Cham, 2019. Springer International Publishing.

[18] Claudio Mannini, Antonino Maria Marra, Luca Pigolotti, and Gianni Bartoli. The effects of free-stream turbulence and angle of attack on the aerodynamics of a cylinder with rectangular 5:1 cross section. *Journal of Wind Engineering and Industrial Aerodynamics*, 161:42–58, 2017.

[19] Claudio Mannini, G Schewe, Ante Soda, and K Weinman. Three-dimensional numerical simulation of flow around a 1: 5 rectangular cylinder. *Three-Dimensional Numerical Simulation of Flow Around a 1*, pages 1000–1004, 2009.

[20] Claudio Mannini, Ante Šoda, and Günter Schewe. Unsteady rans modelling of flow past a rectangular cylinder: Investigation of reynolds number effects. *Computers & fluids*, 39(9):1609–1624, 2010.

[21] Claudio Mannini, Ante Šoda, and Günter Schewe. Numerical investigation on the three-dimensional unsteady flow past a 5: 1 rectangular cylinder. *Journal of Wind Engineering and Industrial Aerodynamics*, 99(4):469–482, 2011.

[22] A Mariotti, MV Salvetti, P Shoeibi Omrani, and JAS Witteveen. Stochastic analysis of the impact of freestream conditions on the aerodynamics of a rectangular 5: 1 cylinder. *Computers & Fluids*, 136:170–192, 2016.

[23] A. Mariotti, L. Siconolfi, and M.V. Salvetti. Stochastic sensitivity analysis of large-eddy simulation predictions of the flow around a 5:1 rectangular cylinder. *European Journal of Mechanics - B/Fluids*, 62:149–165, 2017.

[24] Masaru Matsumoto, Hiromichi Shirato, Kenji Araki, Takashi Haramura, and Tomoaki Hashimoto. Spanwise coherence characteristics of surface pressure field on 2-d bluff bodies. *Journal of Wind Engineering and Industrial Aerodynamics*, 91:155–163, 01 2003.

[25] Hiroshi Nakaguchi. An experimental study on aerodynamics drag of rectangular cylinders. *Journal of the Japan Society for Aeronautical and Space Sciences*, 16(168):1–5, 1968.

[26] Y. Nakamura, Y. Ohya, S. Ozono, and R. Nakayama. Experimental and numerical analysis of vortex shedding from elongated rectangular cylinders at low reynolds numbers 200-103. *Journal of Wind Engineering and Industrial Aerodynamics*, 65(1):301–308, 1996.

[27] Y. Nakamura and T. Yoshimura. Flutter and vortex excitation of rectangular prisms in pure torsion in smooth and turbulent flows. *Journal of Sound and Vibration*, 84(3):305–317, 1982.

[28] Yasuharu Nakamura and Masamichi Nakashima. Vortex excitation of prisms with elongated rectangular, h and [vdash] cross-sections. *Journal of Fluid Mechanics*, 163:149–169, 1986.

[29] Yasuharu Nakamura, Yuji Ohya, and Hideki Tsuruta. Experiments on vortex shedding from flat plates with square leading and trailing edges. *Journal of Fluid Mechanics*, 222:437–447, 1991.

[30] Yuji Ohya, Yasuharu Nakamura, Shigehira Ozono, Hideki Tsuruta, and Ryuzo Nakayama. A numerical study of vortex shedding from flat plates with square leading and trailing edges. *Journal of Fluid Mechanics*, 236:445–460, 1992.

[31] Atsushi Okajima. Strouhal numbers of rectangular cylinders. *Journal of Fluid Mechanics*, 123:379–398, 1982.

[32] R. Parker and M.C. Welsh. Effects of sound on flow separation from blunt flat plates. *International Journal of Heat and Fluid Flow*, 4(2):113–127, 1983.

[33] André FP Ribeiro. Unsteady rans modelling of flow past a rectangular 5: 1 cylinder: investigation of edge sharpness effects. In *Proceedings of the 13th International Conference on Wind Engineering, Amsterdam, The Netherlands*, 2011.

[34] M. Ricci, L. Patruno, S. de Miranda, and F. Ubertini. Flow field around a 5:1 rectangular cylinder using les: Influence of inflow turbulence conditions, spanwise domain size and their interaction. *Computers & Fluids*, 149:181–193, 2017.

[35] Francesco Ricciardelli. Effects of the vibration regime on the spanwise correlation of the aerodynamic forces on a 5:1 rectangular cylinder. *Journal of Wind Engineering and Industrial Aerodynamics - J WIND ENG IND AERODYN*, 98:215–225, 04 2010.

[36] Francesco Ricciardelli and Antonino Marra. Sectional aerodynamic forces and their longitudinal correlation on a vibrating 5:1 rectangular cylinder. 07 2008.

[37] B Rocchio, A Mariotti, and MV Salvetti. Flow around a 5: 1 rectangular cylinder: Effects of upstream-edge rounding. *Journal of Wind Engineering and Industrial Aerodynamics*, 204:104237, 2020.

[38] Kenji Shimada and Takeshi Ishihara. Application of a modified k–ε model to the prediction of aerodynamic characteristics of rectangular cross-section cylinders. *Journal of fluids and structures*, 16(4):465–485, 2002.

[39] Ahmad Sohankar. Large eddy simulation of flow past rectangular-section cylinders: Side ratio effects. *Journal of wind engineering and industrial aerodynamics*, 96(5):640–655, 2008.

[40] A.N. Stokes and M.C. Welsh. Flow-resonant sound interaction in a duct containing a plate, ii: Square leading edge. *Journal of Sound and Vibration*, 104(1):55–73, 1986.

[41] T Tamura, Y Itoh, and K Kuwahara. Computational separated-reattaching flows around a rectangular cylinder. *Journal of Wind Engineering and Industrial Aerodynamics*, 50:9–18, 1993.

[42] TETSURO Tamura, Y Itoh, A Wada, and K Kuwahara. Numerical study of pressure fluctuations on a rectangular cylinder in aerodynamic oscillation. *Journal of wind engineering and industrial aerodynamics*, 54:239–250, 1995.

[43] Boon Thong Tan, Mark Christopher Thompson, and Kerry Hourigan. Flow past rectangular cylinders: receptivity to transverse forcing. *Journal of Fluid Mechanics*, 515:33–62, 2004.

[44] Zhigang Wei and Ahsan Kareem. A benchmark study of flow around a rectangular cylinder with aspect ratio 1: 5 at reynolds number 1. e5. In *Proceedings of the Thirteenth International Conference on Wind Engineering, Amsterdam, The Netherlands*, 2011.

[45] Dahai Yu, Kyle Butler, Ahsan Kareem, James Glimm, and Jiangang Sun. Simulation of the influence of aspect ratio on the aerodynamics of rectangular prisms. *Journal of Engineering Mechanics*, 139(4):429–438, 2013.

[46] Dahai Yu and Ahsan Kareem. Parametric study of flow around rectangular prisms using les. *Journal of Wind Engineering and Industrial Aerodynamics*, 77:653–662, 1998.

UNIVERSITÉ CATHOLIQUE DE LOUVAIN
École polytechnique de Louvain
Rue Archimède, 1 bte L6.11.01, 1348 Louvain-la-Neuve, Belgique | **www.uclouvain.be/epl**